AD_____

Award Number: **W81XWH-11-2-0016**

TITLE: **Physiologic Waveform Analysis for Early Detection of Hemorrhage during Transport and Higher Echelon Medical Care of Combat Casualties**

PRINCIPAL INVESTIGATOR: **Ramakrishna Mukkamala, Ph.D.**

CONTRACTING ORGANIZATION: **Michigan State University, East Lansing, MI 48824**

REPORT DATE: March **2014**

TYPE OF REPORT: **Final**

PREPARED FOR: U.S. Army Medical Research and Materiel Command
         Fort Detrick, Maryland 21702-5012

DISTRIBUTION STATEMENT:

   X Approved for public release; distribution unlimited

REPORT DOCUMENTATION PAGE

Form Approved
OMB No. 0704-0188

Public reporting burden for this collection of information is estimated to average 1 hour per response, including the time for reviewing instructions, searching existing data sources, gathering and maintaining the data needed, and completing and reviewing this collection of information. Send comments regarding this burden estimate or any other aspect of this collection of information, including suggestions for reducing this burden to Department of Defense, Washington Headquarters Services, Directorate for Information Operations and Reports (0704-0188), 1215 Jefferson Davis Highway, Suite 1204, Arlington, VA 22202-4302. Respondents should be aware that notwithstanding any other provision of law, no person shall be subject to any penalty for failing to comply with a collection of information if it does not display a currently valid OMB control number. **PLEASE DO NOT RETURN YOUR FORM TO THE ABOVE ADDRESS.**

1. REPORT DATE (DD-MM-YYYY) March 2014	2. REPORT TYPE Final	3. DATES COVERED (From - To) 15 October 2010 – 14 October 2013

4. TITLE AND SUBTITLE Physiologic Waveform Analysis for Early Detection of Hemorrhage during Transport and Higher Echelon Medical Care of Combat Casualties	5a. CONTRACT NUMBER
	5b. GRANT NUMBER W81XWH-11-2-0016
	5c. PROGRAM ELEMENT NUMBER

6. AUTHOR(S) Ramakrishna Mukkamala email: rama@egr.msu.edu	5d. PROJECT NUMBER
	5e. TASK NUMBER
	5f. WORK UNIT NUMBER

7. PERFORMING ORGANIZATION NAME(S) AND ADDRESS(ES) Michigan State University East Lansing, MI 48824-1046	8. PERFORMING ORGANIZATION REPORT NUMBER

9. SPONSORING / MONITORING AGENCY NAME(S) AND ADDRESS(ES) U. S. Army Medical Research and Materiel Command Fort Detrick, Maryland 21702-5012	10. SPONSOR/MONITOR'S ACRONYM(S)
	11. SPONSOR/MONITOR'S REPORT NUMBER(S)

12. DISTRIBUTION / AVAILABILITY STATEMENT

Approved for public release; distribution unlimited

13. SUPPLEMENTARY NOTES

14. ABSTRACT
Early detection of hemorrhage is crucial for managing combat casualties. However, mean arterial blood pressure (ABP) and other vital signs are late indicators of a bleed. By contrast, cardiac output (CO), stroke volume (SV), ventricular end-diastolic volume (EDV), and autonomic nervous system (ANS) activity can provide timely warning of blood loss. However, existing methods for their measurement are invasive and/or require an operator. On the other hand, a peripheral ABP waveform can be measured non-invasively and automatically with commercial devices that are amenable to most combat casualties during evacuation and medical care thereafter. We have conceived techniques to track CO, SV, EDV, and ANS activity by mathematical analysis of a peripheral ABP waveform and simpler non-invasive waveforms. Our objective was to prove the efficacy of these techniques during hypovolemia. We investigated the techniques based on existing data from conscious humans exposed to lower body negative pressure (LBNP) – a model of early bleeding. Our most significant results were that the techniques can estimate relative changes in CO and SV accurately and better than previous techniques during progressive LBNP and recovery. We also transitioned the techniques from academia to a ventured backed start-up company. The techniques could ultimately be used to help manage combat casualties during transport and higher echelon care.

15. SUBJECT TERMS
cardiovascular physiology, combat casualty care, hemorrhage, signal processing

16. SECURITY CLASSIFICATION OF:			17. LIMITATION OF ABSTRACT	18. NUMBER OF PAGES	19a. NAME OF RESPONSIBLE PERSON USAMRMC
a. REPORT U	b. ABSTRACT U	c. THIS PAGE U	UU	87	19b. TELEPHONE NUMBER (include area code)

Standard Form 298 (Rev. 8-98)
Prescribed by ANSI Std. Z39.18

Table of Contents

1. Introduction

Hemorrhage is a leading cause of combat death. So, early detection of blood loss – when intervention may be most effective – is crucial for managing casualties of war. However, due to compensatory physiologic mechanisms, mean arterial blood pressure (ABP) and other vital signs often change late and precipitously during progressive bleeding. By contrast, cardiac output (CO), stroke volume (SV), ventricular end-diastolic volume (EDV), and autonomic nervous system (ANS) activity can provide timely warning of blood loss as well as guide fluid resuscitation. However, existing methods for their measurement are invasive and/or require a point-of-care operator and are therefore not suitable for austere environments. On the other hand, a peripheral ABP waveform can be measured non-invasively and automatically with commercial devices that are amenable to most combat casualties during evacuation and medical care thereafter. We have conceived techniques to track CO, SV, EDV, and ANS activity by mathematical analysis of a peripheral ABP waveform and simpler non-invasive waveforms. The objective of this project was to prove the efficacy of these physiologic waveform analysis techniques during hypovolemic conditions. To achieve this objective, we investigated the techniques based on existing data from the US Army Institute of Surgical Research (USAISR) comprising requisite measurements from many healthy, conscious humans exposed to lower body negative pressure (LBNP) – an established model of early bleeding. Successful completion of this efficient data analysis project may ultimately translate to effective hemorrhage monitoring during transport and higher echelon care of combat casualties.

2. Keywords

Cardiovascular physiology, combat casualty care, hemorrhage, signal processing

3. Overall Project Summary

In this main section of the final report, we use the same format as our previous reports. Table 1 shows a Gantt chart summarizing the approved statement of work and our progress. Thereafter, we describe our accomplishments with respect to each task.

Task	Y1Q1	Y1Q2	Y1Q3	Y1Q4	Y2Q1	Y2Q2	Y2Q3	Y2Q4	Y3Q1	Y3Q2	Y3Q3	Y3Q4	Status
1a													Completed
1b													Completed
1c													Completed
1d													Completed
2a													Completed
2b													Completed
2c													Completed
3a													Completed
3b													Completed
3c													Completed
4a													Completed
4b													Ongoing
4c													Ongoing

Table 1: Gantt chart summarizing statement of work and progress.

At the start of the project, we performed initial work necessary for conducting the tasks in the statement of work. In particular, we carefully reviewed all of the human LBNP data provided by the USAISR. This effort included the creation of a spreadsheet of the physiologic measurements available for each subject and determination of which subject data were suitable for analysis. We found that data from 125 subjects could be studied in the context of this project. We randomly selected one-fifth of the subjects and used their data as the optimization or training set.

FY10 Task 1. Optimize new physiologic waveform analysis techniques with respect to a portion of the human LBNP data: Subtask 1a. Maximize accuracy of the techniques. (Months 1-6)

This task is completed.

First, as described in [7] (see Appendix), we applied our new long time interval analysis (LTIA) technique to estimate relative changes in CO and SV from the non-invasive peripheral ABP waveforms. We explored various refinements to the technique in an attempt to maximize its accuracy with respect to the training dataset. Integrating the technique with non-invasive pulse transit time (PTT) was most effective. The integrated technique specifically involved first estimating PTT from the available non-invasive thoracic electrical bioimpedance and peripheral ABP waveforms as described in [13] (see Appendix) and then correcting the LTIA technique for arterial compliance changes using the PTT in accordance with the Bramwell-Hill equation as described in [8] (see Appendix). Figure 1 shows that the optimized LTIA technique agreed fairly well with the available reference CO measurement on average. Further, this technique correctly predicted significant reductions in CO during LBNP and an appreciable increase in CO upon recovery in 90% of the subjects.
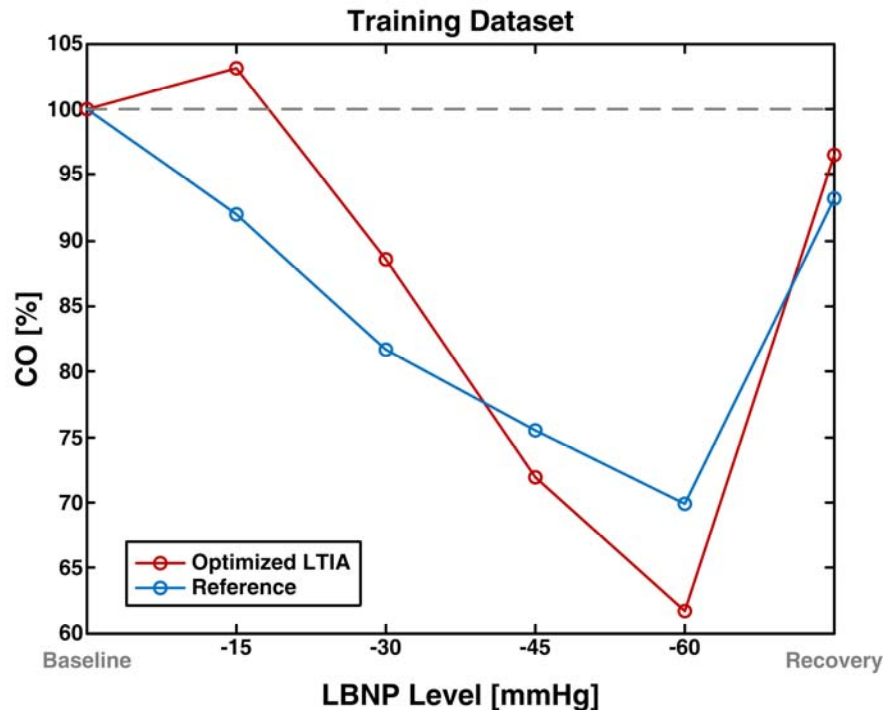

Figure 1: New long time interval analysis (LTIA) technique for estimating relative changes in cardiac output (CO) (and stroke volume (SV)) from non-invasive physiologic waveforms optimized with respect to the training set of the human lower body negative pressure (LBNP) data.

Second, we applied our new short time interval analysis (STIA) technique to estimate relative changes in CO and SV from the peripheral ABP waveforms. This technique involved first estimating the central ABP waveform from the peripheral ABP waveform as described in [12] (see Appendix) and then estimating SV from the central ABP waveform as described in [11] (see Appendix). We likewise explored various refinements to the technique to maximize its accuracy with respect to the training dataset. The PTT correction for arterial compliance changes described above was again most effective. Figure 2 shows that the optimized STIA technique agreed about as well with the reference CO measurement as the optimized LTIA technique on average. The STIA technique also correctly predicted significant reductions in CO during LBNP and an appreciable increase in CO upon recovery in 95% of the subjects. Hence, it performed similarly to the LTIA technique in the training dataset. However, the STIA technique needs only a few beats of the waveform to arrive at an estimate, whereas the LTIA technique requires 30-60 sec intervals of the waveform. Thus, the STIA technique has the advantage of being able to detect very rapid hemodynamic changes.
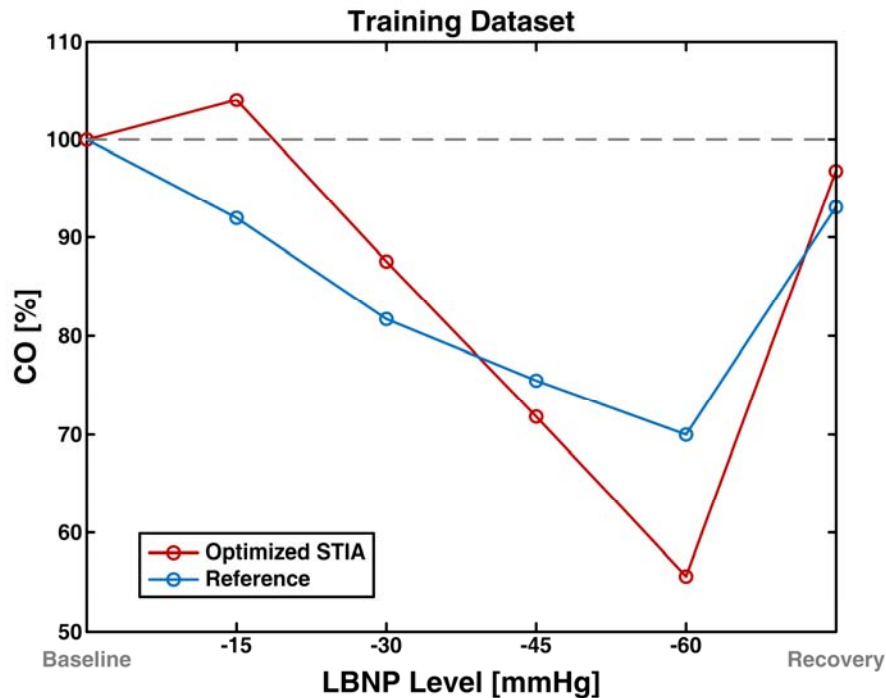

Figure 2: New short time interval analysis (STIA) technique for estimating relative changes in CO (and SV) from non-invasive physiologic waveforms optimized with respect to the training set of the human LBNP data.

Finally, as described in [1] (see Appendix), we applied our new closed-loop identification (CLI) technique to estimate specific cardiac sympathetic and parasympathetic nervous system (SNS and PNS) indices from the non-invasive peripheral ABP, ECG, and respiratory waveforms. We similarly explored various refinements to the technique to maximize its accuracy with respect to the training dataset. We found that sequential identification of impulse responses represented with triangular basis functions was most effective. Figure 3 shows that the optimized CLI technique directionally agreed with the available reference muscle sympathetic nerve activity measurement on average. The average correlation coefficient between the technique and the reference measurement was 0.93.
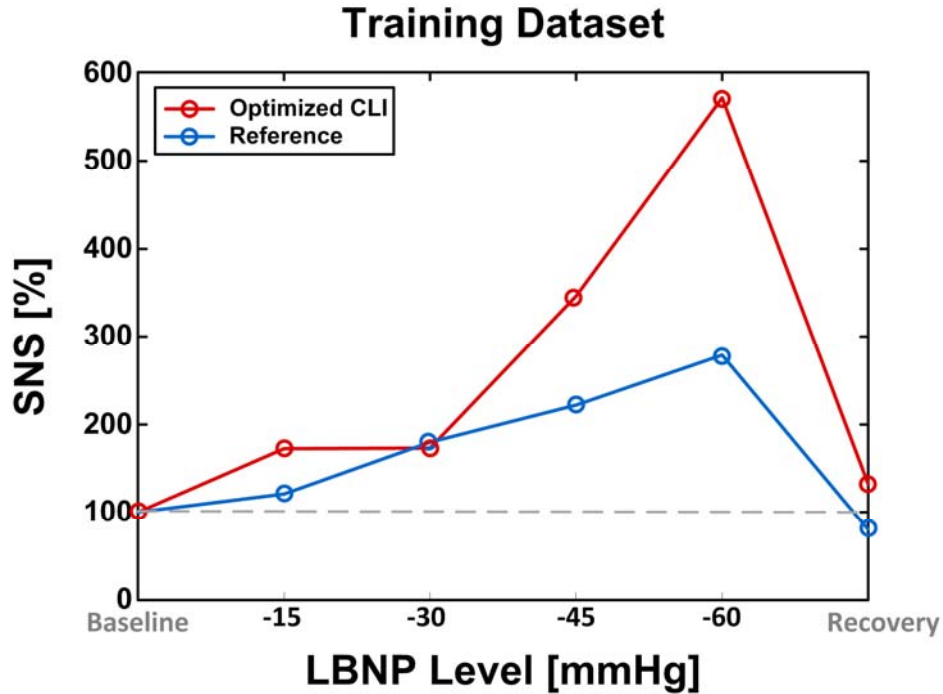
Figure 3: New closed-loop identification (CLI) technique for estimating a specific sympathetic nervous system (SNS) index (and a specific parasympathetic nervous system (PNS) index) from non-invasive physiologic waveforms optimized with respect to the training set of the human LBNP data.

FY10 Task 1. Optimize new physiologic waveform analysis techniques with respect to a portion of the human LBNP data: Subtask 1b. Maximize computational speed of the techniques. (Months 7-8)

This task is completed.

We first coded the three new techniques and a fourth new technique described below in MATLAB using straightforward algorithms on a standard PC. This code executed the LTIA and CLI techniques significantly faster than real-time. On the other hand, the code executed the STIA and fourth techniques, which are similar in complexity, about 15 times slower than real-time. However, the speed of the code, when compiled, increased to near real-time. We also coded an algorithm to further increase the speed of the two techniques via a fast local search (rather than an exhaustive search) that exploits the information from the previous interval for analysis to yield a good initial seed for the current analysis interval. This code increased the speed by a factor of about five. Since the techniques would ultimately be implemented on a fast digital signal processor in the field, computational speed is no longer a concern.

FY10 Task 1. Optimize new physiologic waveform analysis techniques with respect to a portion of the human LBNP data: Subtask 1c. Maximize ability of the techniques to discriminate between LBNP levels and recovery. (Months 9-10)

This task is completed.

We explored various combinations of the variables estimated by the four new techniques to maximize their ability to discriminate between the LBNP levels and recovery with respect to the

7

training dataset. The fourth technique involved estimating the central ABP waveform from the peripheral ABP waveform as described above, estimating relative change in EDV from the central ABP waveform as described in [10] (see Appendix), and correcting for arterial compliance changes using PTT as described above. Neither of the ANS indices was very useful here. However, the relative SV change estimates of the LTIA and STIA techniques and the relative EDV change estimate were all effective, with the former estimated variable offering a bit better discriminatory ability. Combining these variables did not help. The relative CO change estimates of the techniques also showed fairly good discriminatory ability. Table 2 shows good discrimination power of the relative SV change estimate of the LTIA technique in terms of generally high receiver operating characteristic area under the curve (ROC AUC) values. (ROC AUC values range from 0 and 1 and indicate the probability of correct detection/discrimination.)

Level	Recovery	-60 mmHg	-45 mmHg	-30 mmHg
-15 mmHg	0.56	1	0.95	0.81
-30 mmHg	0.78	0.95	0.84	-
-45 mmHg	0.93	0.83	-	-
-60 mmHg	0.99	-	-	-

Table 2: New technique for discriminating between the LBNP levels and recovery from non-invasive physiologic waveforms optimized with respect to the training set of the human LBNP data. Values are receiver operating characteristic area under the curves (ROC AUCs) comparing the relative SV change estimates of the LTIA technique between the indicated levels.

FY10 Task 1. Optimize new physiologic waveform analysis techniques with respect to a portion of the human LBNP data: Subtask 1d. Maximize ability of the techniques to predict intolerance to further increases in LBNP level. (Months 11-12)

This task is completed.

We explored various combinations of the variables estimated by the four new techniques to maximize their ability to predict intolerance to further increases in LBNP level with respect to the training dataset. We first defined intolerant subjects as those who could not complete the LBNP level of -70 mmHg. Just over half the subjects met this criterion. We then used the estimated variables at a LBNP level of -60 mmHg to predict which of the subjects would become intolerant to further LBNP increases. The relative SV change estimate of the STIA technique by itself was most predictive, with a ROC AUC value of 0.78.

FY11 Task 2. Comprehensively evaluate techniques with respect to the remaining portion of the human LBNP data: Subtask 2a. Assess accuracy of the optimized techniques. (Month 17)

This task is completed.

First, we applied the optimized LTIA and STIA techniques to estimate relative changes in CO and SV from the non-invasive physiologic waveforms in the testing dataset. Figure 4 shows that both of these techniques agreed pretty well with the reference CO measurement on average. Further, the LTIA and STIA techniques correctly predicted significant reductions in CO during LBNP and an appreciable increase in CO upon recovery in 96% and 97% of the subjects, respectively. Hence, both techniques afforded accurate monitoring of relative CO change.
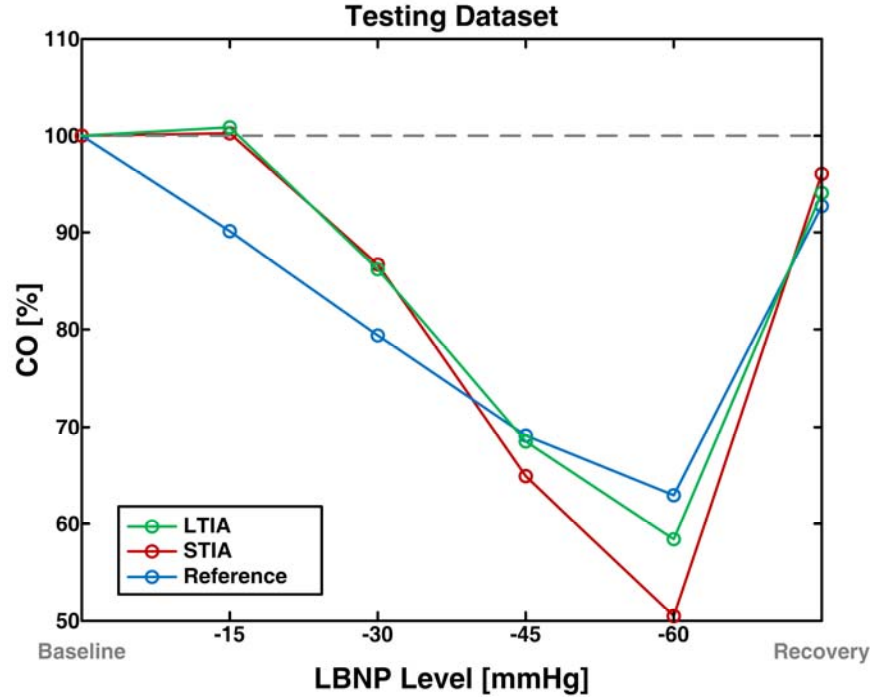
8

Figure 4: New LTIA and STIA techniques for estimating relative changes in CO (and SV) from non-invasive physiologic waveforms in the testing set of the human LBNP data.

Then, we applied the optimized CLI technique to estimate specific SNS and PNS indices from the physiologic waveforms in the testing dataset. Figure 5 shows that this technique agreed to some extent with the reference muscle sympathetic nerve activity measurement on average. The average correlation coefficient between the technique and the reference measurement was 0.75. Hence, this technique provided reasonably accurate monitoring of a specific SNS index.
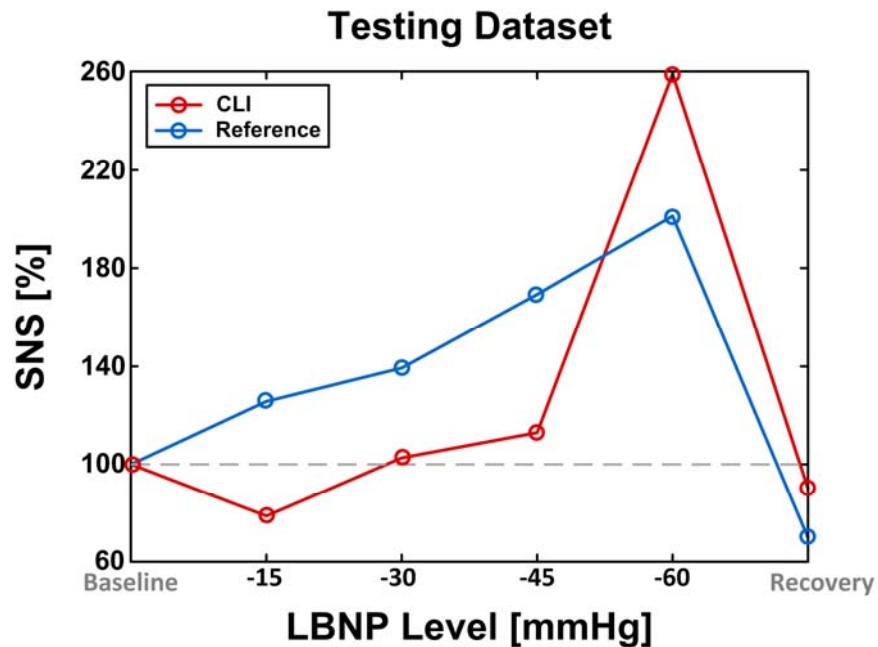

Figure 5: New CLI technique for estimating a specific SNS index (and a specific PNS index) from non-invasive physiologic waveforms in the testing set of the human LBNP data.

FY11 Task 2. Comprehensively evaluate techniques with respect to the remaining portion of the human LBNP data: Subtask 2b. Assess optimized hypovolemia discrimination ability of the techniques. (Month 18)

This task is completed.

We applied the optimized technique to discriminate between the LBNP levels and recovery in the testing dataset. Table 3 shows good discrimination power again in terms of generally high ROC AUC values. Hence, the technique offers sensitive detection of central blood loss.

Level	Recovery	-60 mmHg	-45 mmHg	-30 mmHg
-15 mmHg	0.46	1	0.98	0.84
-30 mmHg	0.81	0.97	0.89	-
-45 mmHg	0.98	0.82	-	-
-60 mmHg	1	-	-	-

Table 3: New technique for discriminating between the LBNP levels and recovery from non-invasive physiologic waveforms in the testing set of the human LBNP data. Values are analogous to Table 2.

FY11 Task 2. Comprehensively evaluate techniques with respect to the remaining portion of the human LBNP data: Subtask 2c. Assess optimized hypovolemia prediction ability of the techniques. (Month 19)

This task is completed.

We applied the optimized technique to predict intolerance to further increases in LBNP level in the testing dataset. The technique achieved a relatively high ROC AUC of 0.73.

FY11 Task 3. Compare techniques to previous physiologic waveform analysis techniques and vital signs: Subtask 3a. Analogously optimize previous physiologic waveform analysis techniques and vital signs. (Months 13-16)

This task is completed.

First, we explored previous techniques for estimating relative changes in CO and SV from the peripheral ABP waveforms in the training dataset. These techniques included the rudimentary mean ABP technique, the classic pulse pressure times heart rate (HR) technique, and the Windkessel technique (i.e., exponential fitting to the diastolic intervals of the waveform). Various versions of the previous techniques were unable to show meaningful reductions in CO during LBNP. One exception was the Modelflow technique (i.e., estimation of the parameters of a three-parameter Windkessel using *in vitro* arterial compliance data and an iteration). However, Figure 6 shows that this technique did not agree that well with the reference CO measurement on average. Further, the technique correctly predicted significant reductions in CO during LBNP and an appreciable increase in CO upon recovery in only 48% of the subjects.

Second, we explored previous techniques for estimating SNS activity from the physiologic waveforms in the training dataset including the popular heart rate (HR) power spectral analysis technique. We found that the ratio of the low frequency to high frequency HR power (LF/HF power) performed best. Figure 7 shows that this technique agreed well with the reference

muscle sympathetic nerve activity measurement on average. The average correlation coefficient between the technique and the reference measurement was 0.96.
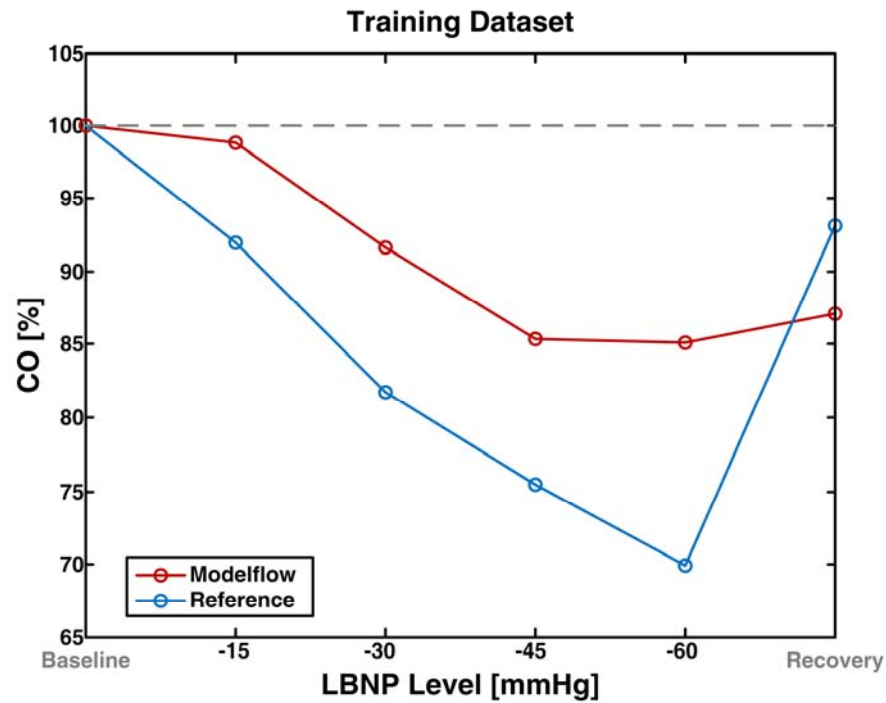

Figure 6: The best previous technique for estimating relative changes in CO (and SV) from non-invasive peripheral ABP waveforms in the training set of the human LBNP data.
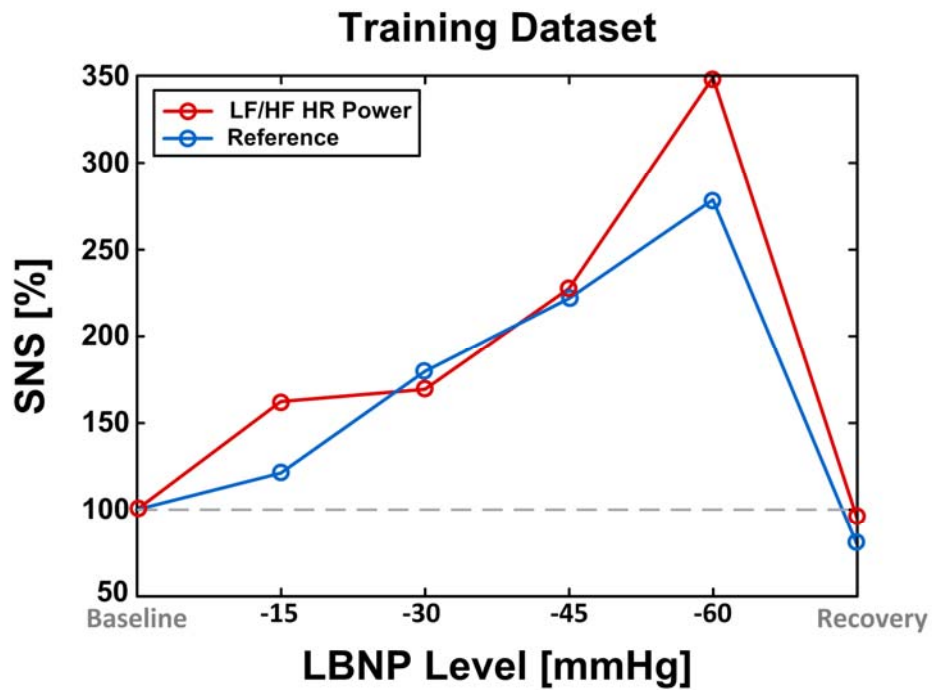

Figure 7: The best previous technique for estimating SNS activity from ECG waveforms in the training set of the human LBNP data.

11

Third, we explored various combinations of the variables estimated by the two previous techniques to maximize their ability to discriminate between the LBNP levels and recovery with respect to the training dataset. We found that the relative SV change estimate of the Modelflow technique by itself was most effective. But, the relative CO change estimate of this technique yielded appreciably reduced discriminatory ability. Table 4 shows good discrimination power of the relative SV change estimate again in terms of ROC AUC values.

Level	Recovery	-60 mmHg	-45 mmHg	-30 mmHg
-15 mmHg	0.46	1	1	0.89
-30 mmHg	0.79	0.98	0.91	-
-45 mmHg	0.95	0.85	-	-
-60 mmHg	0.98	-	-	-

Table 4: The best previous technique for discriminating between the LBNP levels and recovery from non-invasive physiologic waveforms in the training set of the human LBNP data. Values are ROC AUCs comparing the relative SV change estimates of the Modelflow technique between the indicated levels.

Finally, we explored various combinations of the variables estimated by the two previous techniques to maximize their ability to predict intolerance to further increases in LBNP level with respect to the training dataset. We used the definition of intolerance and performed the prediction as described above. We found that the relative SV change estimate of the Modelflow technique was again most effective, with a ROC AUC value of 0.62.

FY11 Task 3. Compare techniques to previous physiologic waveform analysis techniques and vital signs: Subtask 3b. Analogously assess the optimized techniques. (Months 20-21 (first half))

This task is completed.

First, we applied the Modelflow technique to estimate relative changes in CO and SV from the peripheral ABP waveforms in the testing dataset. Figure 8 shows that this technique did not agree that well with the reference CO measurement on average. Further, the technique correctly predicted significant reductions in CO during LBNP and an appreciable increase in CO upon recovery in only 51% of the subjects. Hence, the technique was not accurate.

Second, we applied the HR power spectral analysis technique to estimate SNS activity from the physiologic waveforms in the testing dataset. Figure 9 shows that this technique directionally agreed with the reference muscle sympathetic nerve activity measurement on average. The average correlation coefficient between the technique and the reference measurement was 0.85. Hence, this technique provided relatively accurate monitoring of SNS activity.

Third, we applied the best previous technique to discriminate between the LBNP levels and recovery in the testing dataset. Table 5 shows good discrimination power again in terms of high ROC AUC values. Hence, this technique offers sensitive detection of central blood loss.

Finally, we applied the best previous technique to predict intolerance to further increases in LBNP level in the testing dataset. The technique achieved a ROC AUC value of only 0.54. Hence, its predictive capacity was similar to a coin flip.
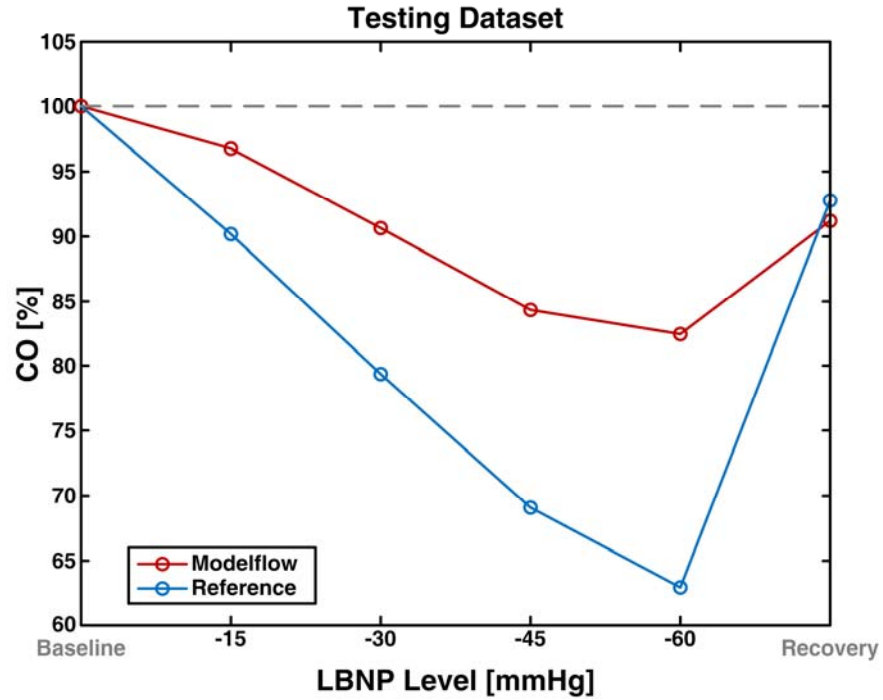
Figure 8: Previous technique for estimating relative changes in CO (and SV) from non-invasive peripheral ABP waveforms in the testing set of the human LBNP data.
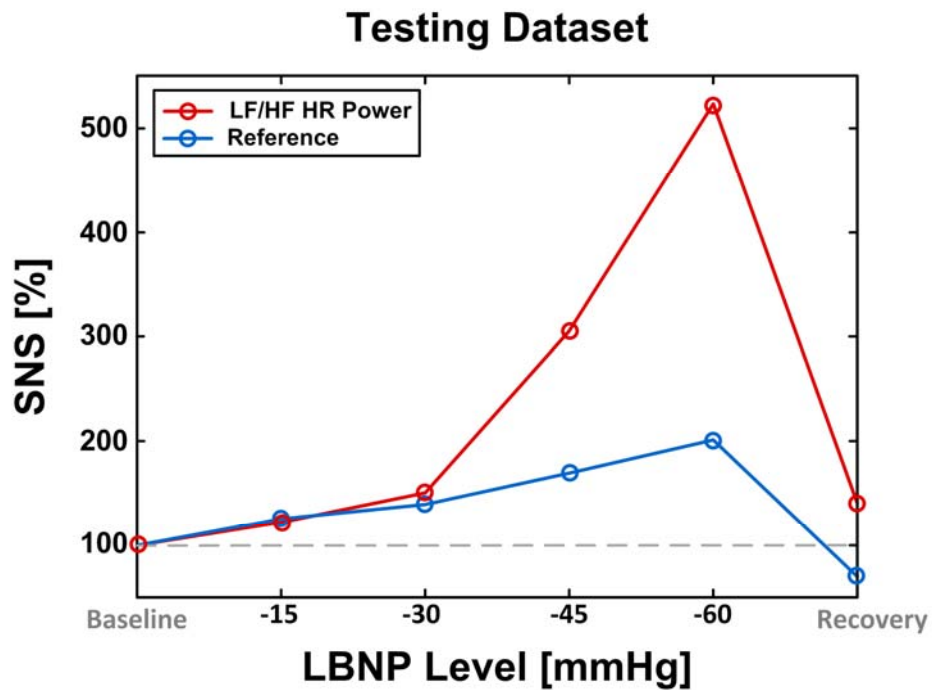

Figure 9: Previous technique for estimating SNS activity from ECG waveforms in the testing set of the human LBNP data.

.

Level	Recovery	-60 mmHg	-45 mmHg	-30 mmHg
-15 mmHg	0.64	1	1	0.91
-30 mmHg	0.92	0.99	0.92	-
-45 mmHg	1	0.84	-	-
-60 mmHg	1	-	-	-

Table 5: Previous technique for discriminating between the LBNP levels and recovery from non-invasive physiologic waveforms in the testing set of the human LBNP data. Values are analogous to Table 4.

FY11 Task 3. Compare techniques to previous physiologic waveform analysis techniques and vital signs: Subtask 3c. Statistically compare the performance of the new and previous techniques. (Months 21 (second half)-22)

This task is completed.

We statistically compared the accuracy and ability to discriminate between the LBNP levels and recovery of the new and previous techniques in the testing dataset as well as their ability to predict intolerance to further increases in LBNP level. Using a Wilcoxon sign-rank test, we found that the new LTIA and STIA techniques were more accurate in monitoring CO than the previous Modelflow technique ($p < 0.000001$). Using the R statistic, we found that the previous LF/HF power technique was more accurate in monitoring the SNS than the new CLI technique ($p < 0.0001$). Using the Hanley-McNeil paired data test with Bonferroni correction (i.e., $p = 0.005$ was regarded as significant), we found that the previous Modelflow technique was better than the new LTIA technique in discriminating between the LBNP level and recovery in two out of ten cases (-15 mmHg vs. -30 mmHg ($p < 0.005$) and -30 mmHg vs. recovery ($p < 0.0001$)). Finally, again using the Hanley-McNeil paired data test, we found that the new STIA technique was better in than the previous Modelflow technique in predicting intolerance to further increases in LBNP level ($p < 0.005$).

To summarize, the new techniques afforded much better accuracy in monitoring CO and in hypovolemia prediction. The previous techniques offered somewhat better ability in hypovolemia discrimination. The previous techniques also provided more accurate SNS monitoring. However, while the previous LF/HF power technique is sensitive to SNS activity, it is known to be nonspecific. For example, it is strongly dependent on the PNS, which declines with progressive LBNP. So, it is unclear whether this technique would ultimately prove more accurate than the new CLI technique in practice.

FY11-12 Task 4. Disseminate results and plan technology transition: Subtask 4a. Disseminate preliminary results through presentations and manuscripts. (Months 7-22)

This task is completed.

In the first year of the project, we presented our initial results at the (1) annual Experimental Biology Conference in Washington, D.C.; (2) Biotechnology HPC Institute of TATRC (Dr. Jacques Reifman's group) in Frederick, MD; (3) weekly MSU Department of Electrical and Computer Engineering Brownbag Seminar; and (4) annual IEEE Engineering in Medicine and Biology Society Conference in Boston, MA. We also published two journal papers, two peer-reviewed conference papers, and one abstract.

In the second year of the project, we presented our latest results at the (1) TATRC Biomonitoring Technologies Product Line Review in Frederick, MD; (2) annual IEEE Engineering in Medicine and Biology Society Conference in San Diego, CA; and (3) USAISR (Dr. Victor Convertino's laboratory) in Fort Sam Houston, TX. We also published one journal paper (in press), three peer-reviewed conference papers, and one abstract. In addition, we filed two provisional patents.

All details are provided in Sections 6 and 7 below.

FY11-12 Task 4. Disseminate results and plan technology transition: Subtask 4b. Disseminate final results through presentations and manuscripts. (Months 23-24)

This task is ongoing.

In the third year of the project, we presented our final results at the (1) Department of Cardiovascular Medicine of Kyushu University in Fukuoka, Japan and (2) annual IEEE Engineering in Medicine and Biology Society Conference in Osaka, Japan. (Within a few weeks after the completion of this project, we also presented the results at the (1) National Biomedical Engineering Conference of Mexico in Aguascallientes and (2) Xerox Research Center in Webster, NY.) In addition, we published one journal paper (in press) and two peer reviewed conference papers and converted the provisional patents to full utility patents. Again, all details are provided in Sections 6 and 7 below.

We still have two journal papers on the final results of this project to publish. The first paper will be about CO monitoring via our LTIA technique, while the second paper will be dedicated to CO and EDV monitoring via our STIA techniques. We have made considerable progress on the first paper. Since we are in the business of publishing papers, we will complete this task unfunded.

FY11-12 Task 4. Disseminate results and plan technology transition: Subtask 4c. Pursue transition of the techniques towards military field deployment. (Months 1-24)

This task is ongoing.

Our major efforts for this task can be divided into four categories.

First, we developed a technique for monitoring the PNS that is more amenable to military field deployment. The problem with the widely used HF HR power as a PNS index is that it can also change with respiration, and the breathing pattern of soldiers surely changes during combat. Our idea was to (a) measure respiratory activity using only a single lead ECG waveform and (b) correct the HF HR power (measured with the same ECG waveform) for respiration using model-based system identification. In this way, respiratory changes are corrected for without requiring any additional sensors. Figure 10 shows initial results demonstrating that respiratory activity can be well tracked from a single lead ECG waveform. Figure 11 shows initial results demonstrating that the respiratory corrected index can provide better tracking of PNS decreases induced by LBNP than the HF HR power. In particular, note that the respiratory corrected index provides an earlier indicator of LBNP and does not predict an increase in PNS activity when the tidal volume increases. However, this technique does require further study.
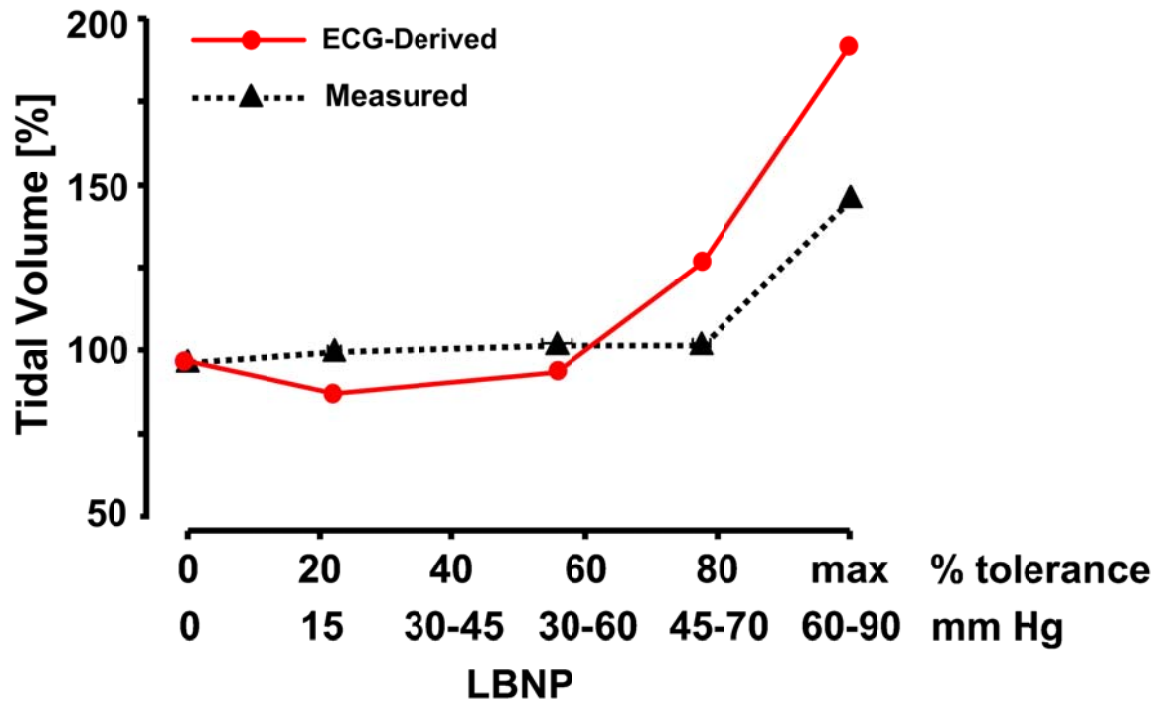
Figure 10: Technique for estimating respiratory activity from a single ECG waveform in a subset of the human LBNP data.
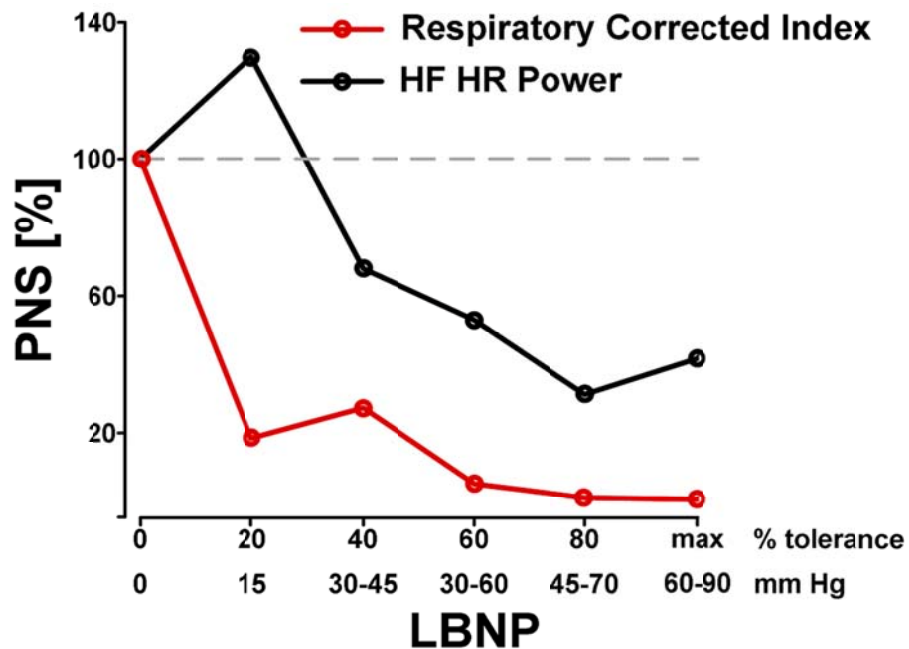

Figure 11: New technique for estimating a respiratory corrected PNS index from a single ECG waveform in the same subset of the human LBNP data along with the conventional HF HR power index of the PNS.

Second, we conceived several techniques for improved ABP monitoring with and without a cuff. In particular, we developed techniques to (1) enhance the accuracy of ABP measurements from the standard automated oscillometric cuff by physical modeling; (2) measure ABP continuously with a finger-cuff but without invoking the expensive arterial unloading principle; and (3) calibrate PTT estimates to ABP without requiring an experimental intervention to perturb ABP and thereby subsequently achieve cuff-less ABP monitoring. The physiologic waveform analysis techniques could potentially be applied to the measurements obtained from some of these techniques so as to be more amendable to military field deployment.

Third, we formed a start-up company based on the new hemodynamic monitoring techniques called Retia Medical (East Lansing, MI). In particular, we successfully recruited a CEO with excellent pedigree, obtained an exclusive license from MSU to use the techniques, and raised Series A venture financing from the Pritzker family. The company is funded to commercialize a minimally invasive CO monitoring device for the hospital market. However, with additional funding, the company will pursue other markets including military field deployment via partnership with an existing vendor of non-invasive ABP sensors.

Fourth, we submitted a number of proposals to further advance the physiologic waveform analysis techniques towards military field deployment. In particular, we submitted (1) three NIH R21 proposals to develop techniques for improved PTT estimation, which is needed for our hemodynamic monitoring techniques; (2) a NIH R21 proposal to extend our techniques to waveforms that are easier to measure than ABP (e.g., pulse oximeter waveforms); (3) a NIH SBIR Phase I proposal with Retia Medical to develop automated waveform artifact handling techniques, which is needed to be able to deploy the techniques in the field; and (4) a NIH U01 proposal to develop simpler ways to measure ABP. The SBIR application was awarded, and other proposals are pending.

Since our main career objective is to actually impact patient care, we will continue to work on this task, particularly through proposal submissions, without funding.

4. Key Research Accomplishments

The key research accomplishments were:

- Accurate estimation of relative changes in CO and SV during human progressive LBNP and recovery via new non-invasive physiologic waveform analysis techniques.

- Reasonably accurate estimation of a specific SNS index during human progressive LBNP and recovery via new non-invasive physiologic waveform analysis techniques.

- Sensitive discrimination between the LBNP levels and recovery via new non-invasive physiologic waveform analysis techniques.

- Superior accuracy in estimating relative changes in CO and SV during progressive LBNP and recovery and superior prediction of intolerance to further increases in LBNP level over previous physiologic waveform analysis techniques.

5. Conclusion

In summary, we optimized and assessed new and previous physiologic waveform analysis techniques for early, automated, and non-invasive detection of hemorrhage with respect to existing human LBNP data. Our most significant technical result was that the new techniques can estimate relative changes in CO and SV much more accurately than previous techniques during progressive hypovolemia and recovery. Our most significant non-technical accomplishment was transitioning the techniques to a venture-backed start-up company. We also disseminated the results widely and pursued a number of directions for technology transition and will continue these tasks unfunded. The new techniques may be employed in conjunction with commercial non-invasive sensors to help reduce combat mortality through timely identification of hemorrhage as well as reliable assessment of the adequacy of fluid resuscitation during transport and higher echelon medical care.

6. Publications, Abstracts, and Presentations

Publications

Peer-Reviewed Journal Papers

Year 1: [13] & [14]

Year 2: [5]

Year 3: [3]

Peer-Reviewed Conference Papers

Year 1: [8] & [16]

Year 2: [2] & [6] & [15]

Year 3: [4] & [9]

Abstracts

Year 1:

Zhang G, Moslehpour M, Mukkamala R. Continuous and less invasive cardiac output monitoring by long time interval analysis of a peripheral arterial blood pressure waveform with pulse transit time correction. Experimental Biology Conference, 2011.

Year 2:

Mukkamala R, Zhang G, Ryan KL, Rickards CA, Convertino VA. Comparison of pulse contour analysis methods in healthy humans exposed to lower body negative pressure. IEEE Engineering in Medicine and Biology Society Conference, 2012.

Presentations

Year 1:

"Continuous and less invasive cardiac output monitoring by long time interval analysis of a peripheral arterial blood pressure waveform with pulse transit time correction", Experimental Biology Conference, Washington DC, April, 2011.

"Hemodynamic monitoring by physiology-based signal processing", DoD Biotechnology HPC Software Applications Institute, Frederick, MD, April, 2011.

"Hemodynamic monitoring by physiology-based signal processing", MSU Department of Electrical and Computer Engineering Brown Bag Faculty Seminar, East Lansing, MI, May, 2011.

"Cardiac output monitoring by long time interval analysis of a radial arterial blood pressure waveform with correction for arterial compliance changes using pulse transit time", IEEE Engineering in Medicine and Biology Society Conference, Boston, MA, August, 2011.*

"Pulse arrival time is not an adequate surrogate for pulse transit time in terms of tracking diastolic blood pressure", IEEE Engineering in Medicine and Biology Society Conference, Boston, MA, August, 2011.*

Year 2:

"Physiologic waveform analysis for early detection of hemorrhage during transport and higher echelon medical care of combat casualties", Telemedicine & Advanced Technology Research Center (Biomonitoring Technologies for Casualties), Fort Diedrick, MD, June, 2012.

"Comparison of pulse contour analysis methods in healthy humans exposed to lower body negative pressure", IEEE Engineering in Medicine and Biology Society Conference, San Diego, CA, August, 2012.

"Model-based error analysis of the oscillometric fixed-ratio blood pressure measurement method", IEEE Engineering in Medicine and Biology Society Conference, San Diego, CA, August, 2012.*

"Perturbationless calibration of pulse transit time to blood pressure", IEEE Engineering in Medicine and Biology Society Conference, San Diego, CA, August, 2012.*

"Physiologic waveform analysis for combat casualty care", USAISR, Fort Sam Houstoon, TX, October, 2012.

Year 3:

"Hemodynamic monitoring by physiology-based signal processing", Department of Cardiovascular Medicine, Kyushu University, Fukuoka, Japan, December 2012.

"An initial step towards improving the accuracy of the oscillometric blood pressure measurement", IEEE Engineering in Medicine and Biology Society Conference, Osaka, Japan, July, 2013.*

"A comparative analysis of reduced arterial models for hemodynamic monitoring", IEEE Engineering in Medicine and Biology Society Conference, Osaka, Japan, July, 2013.*

7. Inventions, Patents and Licenses

Gao M, Mukkamala R. Methods and apparatus for determining pulse transit time as a function of blood pressure. MSU Tech ID 13012 ; US 11/047,516. Pending (utility application filed in August, 2013).

Hahn JO, Liu J, Mukkamala R. Methods and apparatus for determining cuff blood pressure. MSU Tech ID 13021 ; US 14/012,124. Pending (utility application filed in August, 2013).

8. Reportable Outcomes

The reportable outcomes were a set of algorithms for calculating CO, SV, EDV, and SNS and PNS indices from a non-invasive peripheral ABP waveform and other simpler waveforms.

9. Other Achievements

Other achievements under this project include:

- Ph.D. degree in Electrical and Computer Engineering earned by Guanqun Zhang in 2012

- Full-time employment at Sotera Wireless, San Diego, CA, earned by Guanqun Zhang in 2012

- NIH SBIR Phase I Award (1 R43 HL116037-01, 8/15/12-2/28/13).

10. References

[1]   Chen X, Mukkamala R. Selective quantification of the cardiac sympathetic and parasympathetic nervous systems by multisignal analysis of cardiorespiratory variability. American Journal of Physiology, 294(1):H362-H371, 2008.

[2]   Gao M, Mukkamala R. Perturbationless calibration of pulse transit time to blood pressure. Proceedings of the 34th Annual Conference of the IEEE Engineering in Medicine and Biology Society, 1:232-235, 2012.

[3]   Gao M, Zhang G, Olivier NB, Mukkamala R. Improved pulse wave velocity estimation using an arterial tube-load model. IEEE Transactions on Biomedical Engineering, 2013 Nov 20. [Epub ahead of print].

[4]   Liu J, Hahn JO, Mukkamala R. An initial step towards improving the accuracy of the oscillometric blood pressure measurement. Proceedings of the 35th Annual Conference of the IEEE Engineering in Medicine and Biology Society, 1:4082-4085, 2013.

[5]   Liu J, Hahn JO, Mukkamala R. Error mechanisms of the oscillometric fixed-ratio blood pressure measurement method. Annals of Biomedical Engineering,41(3):587-597, 2013.

[6]   Liu J, Hahn JO, Mukkamala R. Model-based error analysis of the oscillometric fixed-ratio blood pressure measurement method. Proceedings of the 34th Annual Conference of the IEEE Engineering in Medicine and Biology Society, 1:633-636, 2012.

[7]   Lu Z, Mukkamala R. Continuous cardiac output monitoring in humans by invasive and non-invasive peripheral blood pressure waveform analysis. Journal of Applied Physiology, 101(2):598-608, 2006.

[8]   Moshlehpour M, Zhang G, Mukkamala R. Cardiac output monitoring by long time interval analysis of a radial arterial blood pressure waveform with correction for arterial compliance changes using pulse transit time. Proceedings of the 33rd Annual Conference of the IEEE Engineering in Medicine and Biology Society, 1:5496-5498, 2011.

[9]   Mukkamala R, Gao M. A comparative analysis of reduced arterial models for hemodynamic monitoring. Proceedings of the 35th Annual Conference of the IEEE Engineering in Medicine and Biology Society, 1:225-228, 2013.

[10]   Swamy G, Kuiper J, Gudur MSR, Olivier NB, Mukkamala R. Continuous left ventricular ejection fraction monitoring by aortic pressure waveform analysis. Annals of Biomedical Engineering, 37(6):1055-1068, 2009.

[11]   Swamy G, Mukkamala R. Estimation of the aortic pressure waveform and beat-to-beat cardiac output from multiple peripheral artery pressure waveforms. IEEE Transactions on Biomedical Engineering, 55(5):1521-1529, 2008.

[12]   Swamy G, Xu D, Olivier NB, Mukkamala R. Adaptive transfer function for deriving the aortic pressure waveform from a peripheral artery pressure waveform. American Journal of Physiology, 297(5):H1956-H1963, 2009.

[13]   Xu D, Ryan KL, Rickards CA, Zhang G, Convertino VA, Mukkamala R. Improved pulse transit time estimation by system identification analysis of proximal and distal arterial waveforms. American Journal of Physiology, 301(4):H1389-H1395, 2011.

[14]   Zhang G, Gao M, Xu D, Olivier NB, Mukkamala R. Pulse arrival time is not an adequate surrogate for pulse transit time as a marker of blood pressure. Journal of Applied Physiology, 111(6):1681-1686, 2011.

[15]   Zhang G, Ryan KL, Rickards CA, Convertino VA, Mukkamala R. Early detection of hemorrhage via central pulse pressure derived from a non-invasive peripheral arterial blood pressure waveform. Proceedings of the 34th Annual Conference of the IEEE Engineering in Medicine and Biology Society, 1:3116-3118, 2012.

[16]   Zhang G, Xu D, Olivier NB, Mukkamala R. Pulse arrival time is not an adequate surrogate for pulse transit time in terms of tracking diastolic blood pressure. Proceedings of the 33rd Annual Conference of the IEEE Engineering in Medicine and Biology Society, 1:6462-6464, 2011.

You might find this additional information useful...

This article cites 39 articles, 17 of which you can access free at:
http://ajpheart.physiology.org/cgi/content/full/294/1/H362#BIBL

Updated information and services including high-resolution figures, can be found at:
http://ajpheart.physiology.org/cgi/content/full/294/1/H362

Additional material and information about *AJP - Heart and Circulatory Physiology* can be found at:
http://www.the-aps.org/publications/ajpheart

This information is current as of May 23, 2008 .

Selective quantification of the cardiac sympathetic and parasympathetic nervous systems by multisignal analysis of cardiorespiratory variability

Xiaoxiao Chen and Ramakrishna Mukkamala

Department of Electrical and Computer Engineering, Michigan State University, East Lansing, Michigan

Chen X, Mukkamala R. Selective quantification of the cardiac sympathetic and parasympathetic nervous systems by multisignal analysis of cardiorespiratory variability. *Am J Physiol Heart Circ Physiol* 294: H362–H371, 2008. First published November 9, 2007; doi:10.1152/ajpheart.01061.2007.—Heart rate (HR) power spectral indexes are limited as measures of the cardiac autonomic nervous systems (CANS) in that they neither offer an effective marker of the β-sympathetic nervous system (SNS) due to its overlap with the parasympathetic nervous system (PNS) in the low-frequency (LF) band nor afford specific measures of the CANS due to input contributions to HR [e.g., arterial blood pressure (ABP) and instantaneous lung volume (ILV)]. We derived new PNS and SNS indexes by multisignal analysis of cardiorespiratory variability. The basic idea was to identify the autonomically mediated transfer functions relating fluctuations in ILV to HR (ILV→HR) and fluctuations in ABP to HR (ABP→HR) so as to eliminate the input contributions to HR and then separate each estimated transfer function in the time domain into PNS and SNS indexes using physiological knowledge. We evaluated these indexes with respect to selective pharmacological autonomic nervous blockade in 14 humans. Our results showed that the PNS index derived from the ABP→HR transfer function was correctly decreased after vagal and double (vagal + β-sympathetic) blockade ($P < 0.01$) and did not change after β-sympathetic blockade, whereas the SNS index derived from the same transfer function was correctly reduced after β-sympathetic blockade in the standing posture and double blockade ($P < 0.05$) and remained the same after vagal blockade. However, this SNS index did not significantly decrease after β-sympathetic blockade in the supine posture. Overall, these predictions were better than those provided by the traditional high-frequency (HF) power, LF-to-HF ratio, and normalized LF power of HR variability.

heart rate variability; modeling; power spectral analysis; system identification; transfer function

OVER TWO DECADES AGO, Cohen and co-workers demonstrated that power spectral analysis of resting heart rate (HR) variability could provide more specific measures of the cardiac autonomic nervous systems (CANS) than a basic single time statistical analysis (e.g., mean and SD) (1, 2, 26). Using selective pharmacological autonomic nervous blockade, these investigators demonstrated that low-frequency (LF; 0.04–0.15 Hz) fluctuations in HR are jointly mediated by the parasympathetic nervous system (PNS) and β-sympathetic nervous system (SNS), whereas high-frequency (HF; 0.15–0.4 Hz) fluctuations are solely mediated by the PNS. It therefore directly followed that the HF power of HR variability could serve as a simple quantitative index of the PNS. Shortly thereafter, Malliani et al. (18) proposed the ratio of the LF power to HF power of HR variability [LF-to-HF ratio (LF/HF ratio)] as an index of sympathovagal balance as well as normalized LF and HF powers as indexes of the CANS independent of the total power or variance. Since then, these easily obtainable indexes have been extensively studied under a wide variety of pathophysiologic conditions (31), having most notably been shown to be associated with mortality in various patient classes [e.g., postmyocardial infarction (10), cardiac arrest (13), and critically ill (36)] as well as to be altered by various disease processes [e.g., diabetic autonomic neuropathy (14, 23), congestive heart failure (11, 29), and hypertension (15, 16)]. Today, the HF power of HR variability is generally accepted as a useful index of the PNS, whereas the LF/HF ratio and normalized LF power are sometimes considered to be indexes of sympathovagal balance or the SNS (31).

Despite their widespread use and established association with disease, HR power spectral indexes are quite controversial in terms of being actual measures of the CANS (18, 24). Part of this controversy simply stems from the common misconception that these indexes should be indicative of basal or mean autonomic outflow when they are, in fact, intended to reflect the fluctuations in autonomic outflow about the mean value. The remaining part of the controversy surrounding HR power spectral indexes is based on their intrinsic limitations as measures of such fluctuations. One of the major limitations is that HR power spectral indexes, including the LF/HF ratio and normalized LF power, generally cannot provide an effective marker of the SNS (i.e., fluctuations in SNS outflow), because the LF power is mediated by both CANS, as shown in the initial study by Cohen and co-workers and verified in a subsequent study (25). Another major limitation, alluded to above, is that none of the HR power spectral indexes is truly specific to the CANS, since HR is just an output of these systems. For example, it is well known that the ultimate source of the HF power of HR variability is respiration. Thus, changes in the HF power could also reflect changes in the respiratory input. Similarly, changes in the LF power of HR variability could also reflect changes in arterial blood pressure (ABP) fluctuations, which may cause HR fluctuations through the baroreflex (1). So, for example, the HF power may not provide a useful means to monitor the PNS during exercise (18), whereas the LF/HF ratio may not be an effective indicator of sympathovagal balance when local vasomotor activity alters the variability of the ABP input (1, 40).

As a result, investigators have recently sought improved indexes of the CANS by employing more sophisticated analyses of beat-to-beat cardiovascular variability. Vetter et al. proposed to selectively quantify the PNS and SNS using a

---

blind source separation analysis of HR and ABP variability (33) as well as HR and QT interval variability (34). Chon and co-workers then introduced a principal dynamic mode analysis of HR variability to separately characterize the two CANS (40, 41). The common idea underlying each of these analyses is to distinguish the SNS from the PNS by invoking some sort of independence or orthogonality assumption, which is generally untenable. Despite this assumption, the results of these analyses were quite promising and sparked our own interest in pursuing improved indexes of the PNS and SNS.

In this article, we derive indexes of the PNS and SNS based on a multisignal analysis of the beat-to-beat variability in potentially noninvasively measured HR, ABP, and instantaneous lung volume (ILV). The basic idea of the analysis, which was briefly proposed by us with co-workers in Ref. 38 (see the DISCUSSION), was to identify the transfer functions relating the fluctuations in ILV and ABP to HR so as to effectively eliminate the input contributions to HR and then separate the estimated transfer functions in the time domain into PNS and SNS indexes using physiological insight rather than any independence or orthogonality assumption. We then showed that these new indexes are better than traditional HR power spectral indexes in terms of predicting the known effects of selective pharmacological autonomic nervous blockade on the two CANS in 14 healthy human subjects.

Our multisignal analysis of cardiorespiratory variability aims to derive specific indexes of the PNS and SNS from the dynamic coupling relating fluctuations in ILV to HR (ILV→HR), which represents the autonomically mediated respiratory sinus arrhythmia phenomena (21), and the dynamic coupling relating the fluctuations in ABP to HR (ABP→HR), which characterizes the autonomically mediated HR baroreflex (21). [Note that ILV→HR coupling is actually noncausal, perhaps due to coupling between the respiratory and HR control centers in the brain (21, 30, 32).] The analysis specifically invokes two key linearity assumptions that are justified by previous physiological findings. The first assumption is that ILV→HR and ABP→HR couplings may be well approximated with linear and time-invariant transfer functions for small, resting fluctuations. This assumption is supported by the work of Chon et al., who showed that 70–75% of the variance of resting HR variability could be explained by linear couplings, whereas only an additional 10–15% of the variance could be attributed to second-order nonlinear couplings (12). The second assumption is that the ILV→HR and ABP→HR transfer functions may each be modeled in its time domain impulse response form as the superposition of early and fast PNS component and a delayed and sluggish SNS component, as initially observed by Triedman et al. (32). This assumption is buttressed by known physiology and the comparison shown in Fig. 1 of the impulse responses relating pure vagal and sympathetic stimulation to HR fluctuations that were experimentally determined by Berger et al. (8) in dogs with typical ILV→HR and ABP→HR impulse responses that were identified by analysis of cardiorespiratory fluctuations from humans at rest (21). [Note that the data of Berger et al. actually revealed
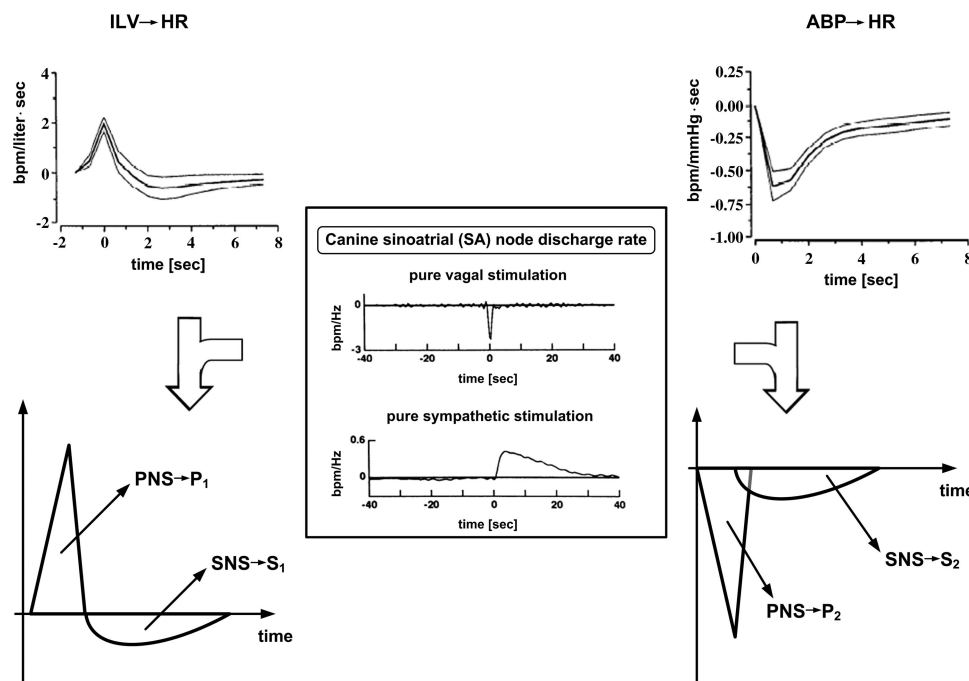

Fig. 1. Models of transfer functions relating fluctuations in instantaneous lung volume to heart rate (ILV→HR) and fluctuations in arterial blood pressure to HR (ABP→HR) upon which the multisignal analysis of cardiorespiratory variability is based. The models (*bottom left* and *bottom right*) specifically represent each transfer function in its time domain impulse response form as the superposition of an early and fast parasympathetic nervous system (PNS) component and a delayed and sluggish β-sympathetic nervous system (SNS) component. These models originated by comparing the impulse responses relating pure vagal and sympathetic stimulation to HR fluctuations that were experimentally determined in dogs (*middle*; reproduced from Ref. 8) with typical ILV→HR and ABP→HR impulse responses that were previously estimated by analysis of cardiorespiratory fluctuations from humans (*top left* and *top right*; reproduced from Ref. 19). [The experimentally determined vagal impulse response shows no time delay, whereas the experimentally determined sympathetic impulse response shows a delay of ∼2 s (8).] The pairs of scalar indexes, P_1 and S_1 as well as P_2 and S_2, represent the two norms of the PNS and SNS components of ILV→HR and ABP→HR impulse responses, respectively. bpm, Beats per minute.

that the sympathetic impulse response is delayed by ~2 s with respect to the vagal impulse response (8).] It should be further noted that the comparison shown in Fig. 1 effectively represents an extrapolation of the efferent autonomic nervous limbs in dogs to the afferent, central, and efferent autonomic nervous limbs in humans. The results shown in Fig. 1 therefore suggest that the frequency dependency of the ILV→HR and ABP→HR impulse responses can be largely attributed to efferent autonomic nervous limbs and that the CANS of dogs can well represent the CANS of humans. Based on these two linearity assumptions, the multisignal analysis of cardiorespiratory variability is employed in three steps.

In the first step, ILV→HR and ABP→HR impulse responses are estimated by applying parametric system identification to resting beat-to-beat fluctuations in HR, ABP, and ILV according to the block diagram shown in Fig. 2. In this way, the known correlation between ILV and ABP inputs is accounted for by simultaneously considering the contributions of both inputs to HR (i.e., dual-input identification), and the feedback baroreflex effects of fluctuations in ABP on HR may be disentangled from the feedforward mechanical effects of fluctuations in HR on ABP through the imposition of causality (i.e., open-loop identification of closed-loop systems) (35). The block diagram also includes a perturbing noise source (N_{HR}), which is also estimated and represents the residual HR variability not accounted for by the two inputs. This step is mathematically achieved with the following double-exogenous model with autoregressive (AR) input (27) originally proposed by Baselli et al. (4, 5):

$$HR[n] = \sum_{i=m}^{M} g[i]ILV[n-i] + \sum_{i=1}^{N} h[i]ABP[n-i] + N_{HR}[n]$$
$$(1)$$

$$N_{HR}[n] = \sum_{i=1}^{P} a[i]N_{HR}[n-i] + W_{HR}[n],$$

where n is discrete time. The sets of unknown finite impulse response (FIR) parameters {$g[i]$, $h[i]$}, respectively, define ILV→HR and ABP→HR impulse responses, whereas the unmeasured residual white noise error (W_{HR}) and the set of unknown AR parameters {$a[i]$} specify N_{HR}. The terms m, M, and N represent the maximum expected durations of the FIRs,
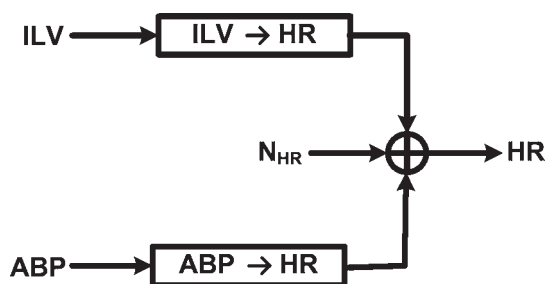

Fig. 2. Block diagram illustrating the estimation of the ILV→HR and ABP→HR impulse responses by application of parametric system identification to resting beat-to-beat fluctuations in HR, ABP, and ILV. N_{HR}, which represents the residual variability in HR not accounted for by the two inputs, is also estimated in the process.

whereas P limits the number of AR parameters. Note that the causality of the ABP→HR impulse response is enforced here by virtue of setting the $h[i]$ parameters to 0 for negative values of i, whereas the noncausality of the ILV→HR impulse response is accounted for by setting m to a negative value. The parameter sets are estimated from ~6-min intervals of zero-mean fluctuations in HR, ABP, and ILV sampled at 1.5 Hz based on least-squares minimization of W_{HR} using a weighted-principal component regression method (37) (see the APPENDIX). Prior to the application of this method, HR and ABP are normalized by their mean values and ILV is normalized by its SD, as described in Ref. 38. Thus, the identified impulse responses will have units of s^{-1} and represent the relationship between relative fluctuations in the input about its mean value and relative fluctuations in the output about its mean value.

In the second step, the estimated ILV→HR and ABP→HR impulse responses are each separated into PNS and SNS components as generally shown in Fig. 1. More specifically, the typical ILV→HR impulse response here indicates that, in response to an impulse increase in ILV at *time 0*, HR would first increase due to early (noncausal) and fast parasympathetic withdrawal and then decrease due to delayed and sluggish β-sympathetic withdrawal. Thus, the PNS and SNS components are of opposite direction in amplitude and delayed in time with respect to each other. As a result, the PNS component of the ILV→HR impulse response is precisely determined as the initial portion of the impulse response extending up to the first 0 crossing (as this marker specifies the amplitude direction change) following the time of the peak amplitude that occurs within the first 5 s (as the PNS is fast), whereas the SNS component is specified as the remaining latter portion of the impulse response (as the SNS is slow and delayed). The typical ABP→HR impulse response shown in Fig. 1 indicates that, in response to an impulse increase in ABP at *time 0*, HR would decrease first due to early (causal) and fast parasympathetic activation and then due to delayed and sluggish β-sympathetic withdrawal. Thus, the PNS and SNS components here are also delayed in time with respect to each other but are of the same direction in amplitude. As a result, the separation procedure is not as straightforward for the ABP→HR impulse response. In particular, the initial downstroke of this impulse response is regarded as the first part of the PNS component. The time interval of the initial downstroke is precisely defined up to the minimum amplitude that occurs within the first 5 s (as the PNS is fast). The remaining part of the PNS component (i.e., the return of this stable component to 0), which may be obscured by the subsequent SNS component, is assumed to be symmetric to the visible first part, as suggested by the data of Berger et al. shown in Fig. 1. The SNS component is then established by subtracting the total PNS component from the entire ABP→HR impulse response (as the SNS is slow and delayed). Note that the separation procedure for the ILV→HR impulse response assumes that the PNS and SNS components do not overlap in time, whereas this separation procedure makes no such assumption.

In the third step, scalar indexes of the PNS and SNS are determined from the corresponding components of the ILV→HR and ABP→HR impulse responses. Specifically, the two norms (i.e., square root of the energy) of the PNS and SNS components are calculated to arrive at a pair of PNS and SNS indexes denoted as P_1 and S_1 as determined

from the ILV→HR impulse response and P_2 and S_2 as determined from the ABP→HR impulse response. Note that these indexes will be dimensionless due to the aforesaid signal normalization.

MATERIALS AND METHODS

Experimental data. We evaluated P_1 and P_2 indexes of the PNS and S_1 and S_2 indexes of the SNS with respect to a previously collected human cardiorespiratory dataset. The materials and methods utilized in the collection of this dataset are described in detail elsewhere (30). The experimental protocol was approved by the MIT Committee on the Use of Humans as Experimental subjects, and written informed consent was obtained from the subjects.

Briefly, 14 healthy male subjects (age: 19–38 yr) participated. Surface ECG, ABP (radial artery catheter), and ILV (chest-abdomen inductance plethysmography) were continuously recorded at a sampling rate of 360 Hz. Throughout the recordings, the subjects initiated each respiratory cycle on cue to a sequence of audible tones spaced at random intervals of 1–15 s with a mean of 5 s (7). The purpose of this random-interval breathing protocol was to produce a broadband ILV signal so as to enhance the reliability of subsequent system identification analyses, especially pertaining to the estimation of couplings involving ILV as the input. Approximately 13-min intervals of the random-interval breathing cardiorespiratory measurements were recorded for each of six experimental conditions. First, control measurements were recorded from the subjects in supine and standing postures. Then, seven of the subjects received atropine at 0.03 mg/kg iv (vagal blockade), and measurements were recorded from the subjects in the two postures. Finally, these subjects received propranolol at 0.2 mg/kg iv (β-sympathetic blockade) to achieve total cardiac autonomic nervous blockade (double blockade), and measurements were again recorded from the subjects in both postures. The remaining seven subjects were studied similarly but received the drugs in reverse order. A 5-min period for hemodynamic equilibration was allowed between each experimental condition.

Data analysis As described in Refs. 6 and 30, ABP and ILV were digitally filtered and decimated to 1.5 Hz, and synchronized 1.5 Hz HR tachograms were constructed from surface ECGs. PNS and SNS indexes were then derived as described above from two nonoverlapping intervals of each ~13-min record in the cardiorespiratory dataset. The resulting pairs of each index from each data record were then averaged. For comparison, the HF power, LF/HF ratio, and normalized LF power [LF/(LF+HF)] of HR tachograms were analogously computed for each data record using AR power spectral analysis (31) with postfiltering (6). [HF and LF bands were defined here to range from 0.04 to 0.15 Hz and from 0.15 to 0.40 Hz, respectively (31).] For each of the seven investigated indexes, outliers defined to be >2 SDs from the mean value were removed, wherein means and SDs were robustly estimated with the Gaussian-based method of Armoundas et al. (3). Finally, paired t-tests were performed to determine if the indexes were significantly altered from the control condition to each drug condition.

RESULTS

Figures 3 and 4 show group average results (mean ± SE) for the estimated ILV→HR and ABP→HR impulse responses along with the corresponding P_1 and P_2 indexes of the PNS and S_1 and S_2 indexes of the SNS before (control) and after vagal, β-sympathetic, and double blockade in the standing posture. Generally speaking, it can be seen visually that the early and fast PNS components of the two impulse responses were blunted much more following vagal and double blockade than β-sympathetic blockade, whereas the delayed and slower SNS components were more strongly attenuated after β-sympathetic and double blockade than vagal blockade.

Figure 5 summarizes group average results (mean ± SE) for the two PNS indexes of P_1 and P_2 derived from the estimated ILV→HR and ABP→HR impulse responses and the conventional HF power of HR variability. As expected, the HF power
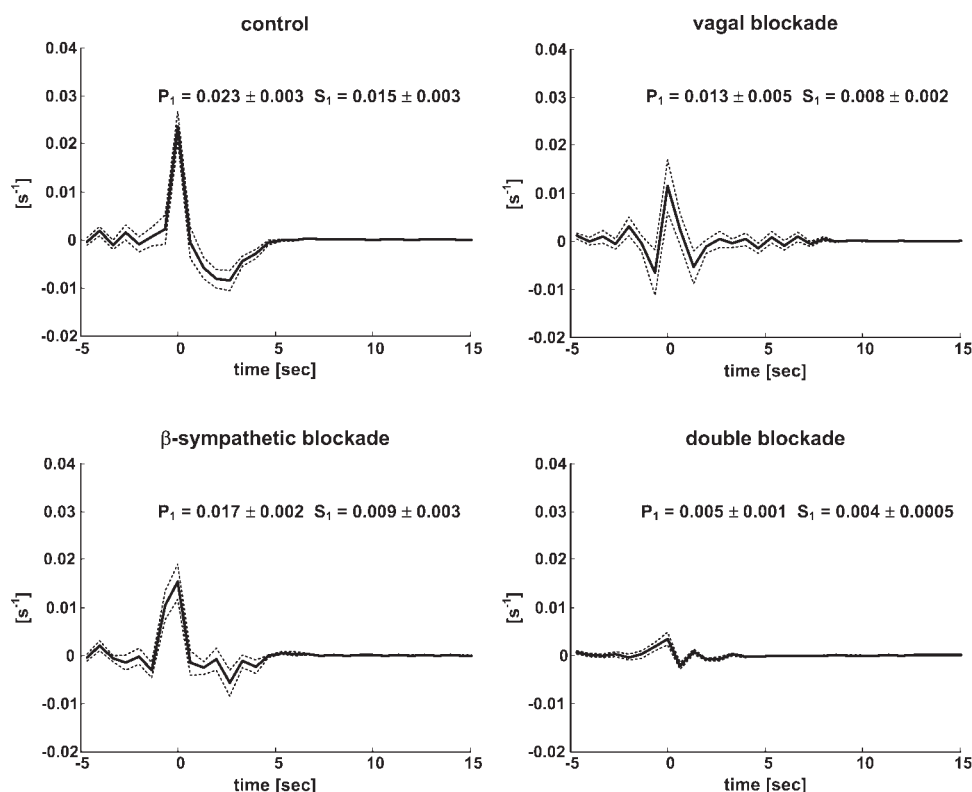
Fig. 3. Group average results (mean ± SE) for the estimated ILV→HR impulse responses and the corresponding P_1 and S_1 indexes from 14 human subjects before (control) and after vagal, β-sympathetic, and double (vagal + β-sympathetic) blockade in the standing posture.
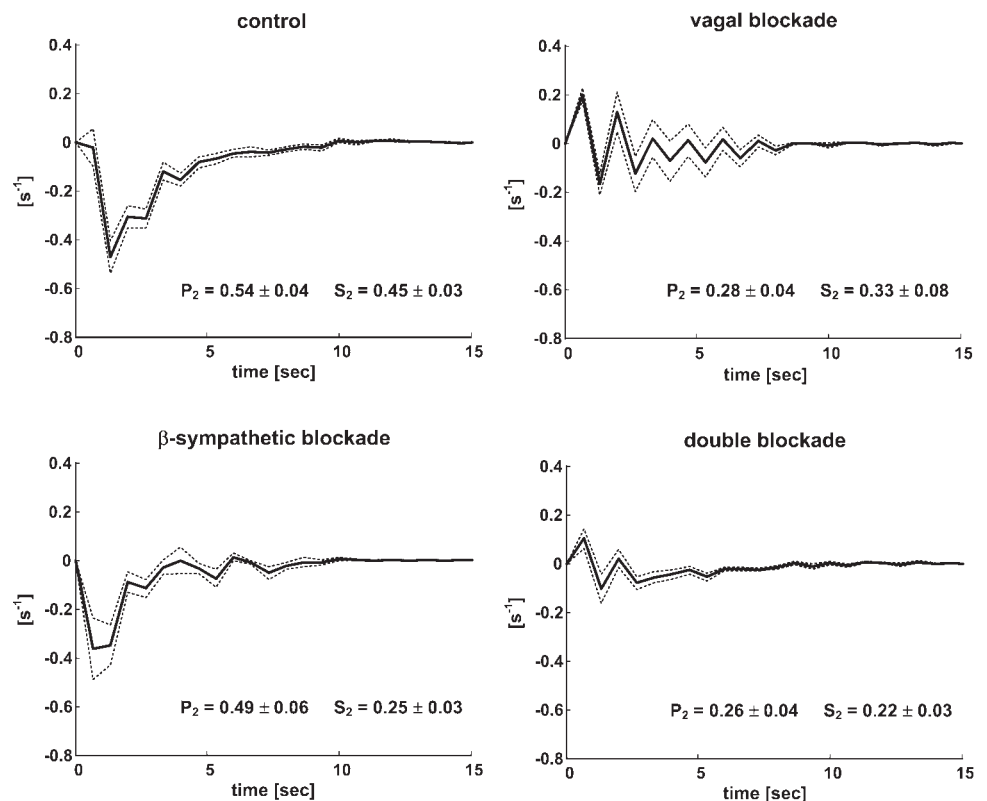
Fig. 4. Group average results (mean $\pm$ SE) for the estimated ABP$\rightarrow$HR impulse responses and the corresponding P_2 and S_2 indexes from 14 human subjects before (control) and after vagal, β-sympathetic, and double (vagal + β-sympathetic) blockade in the standing posture.

generally performed well in predicting the known effects of the pharmacological autonomic nervous blockade agents on the PNS. In particular, this index was virtually abolished following vagal and double blockade with $P < 0.05$. Furthermore, the index did not change after β-sympathetic blockade in the supine posture. However, counter to expectation, the PNS index did decrease following β-sympathetic blockade in the standing posture with $P < 0.05$. Overall, the P_1 index was better in predicting the known drug effects on the PNS. That is, this index reduced considerably after vagal and double blockade with $P < 0.10$ and did not change following β-sympathetic blockade in either posture. The P_2 index provided even better predictive capacity in that it decreased after vagal and double blockade with $P < 0.01$ while remaining unchanged after β-sympathetic blockade. However, the extent of the reductions was not as marked as the other indexes.

Figure 6 summarizes group average results (mean $\pm$ SE) for the two SNS indexes of S_1 and S_2 derived from the two estimated impulse responses and the conventional LF/HF ratio and normalized LF power of HR variability. As expected, the LF/HF ratio did not perform as well in predicting the known effects of the autonomic nervous blockade drugs on the SNS as the HF power did in predicting the drug effects on the PNS. Whereas the LF/HF ratio did decrease following β-sympathetic blockade with $P < 0.05$ and did not change after vagal blockade, it did not diminish after double blockade. In fact, this index actually increased following double blockade in the standing posture with $P < 0.10$. The LF/HF ratio appeared to be a somewhat better index of sympathovagal balance, as it doubled following vagal blockade, albeit not to any level of statistical significance. Overall, the normalized LF power did not provide an improved ability to predict the drug effects on

the SNS. This index did decrease after double blockade with $P < 0.10$ and after β-sympathetic blockade in the standing posture with $P < 0.001$ but did not diminish after β-sympathetic blockade in the supine posture. Furthermore, the extent of the reductions was always very small. In addition, in contrast to expectation, the index increased after vagal blockade in the supine posture but not the standing posture with $P < 0.05$. The S_1 index likewise did not offer enhanced predictive capacity. This index did substantially decrease after double blockade with $P < 0.005$ but did not change after β-sympathetic blockade in both postures. Moreover, the SNS index actually decreased after vagal blockade in the supine posture with $P < 0.10$. On the other hand, the S_2 index afforded overall improved ability in predicting the drug effects on the SNS. In particular, this index did not change after vagal blockade and decreased after double blockade in both postures and β-sympathetic blockade in the standing posture with $P < 0.05$. Its only blemish was that the decrease after β-sympathetic blockade in the supine posture was not statistically significant.

DISCUSSION

Conventional HR power spectral indexes are indisputably of significant physiological and prognostic value but suffer from limitations as measures of the CANS. Most notably, these indexes neither offer an effective marker of the SNS due to its joint mediation with the PNS in the LF band nor afford specific measures of the CANS due to the input contributions to HR (e.g., ILV and ABP). In this study, we aimed to overcome these limitations by deriving indexes of the PNS and SNS via multisignal analysis of cardiorespiratory variability. More specifically, first, we applied parametric system identification to
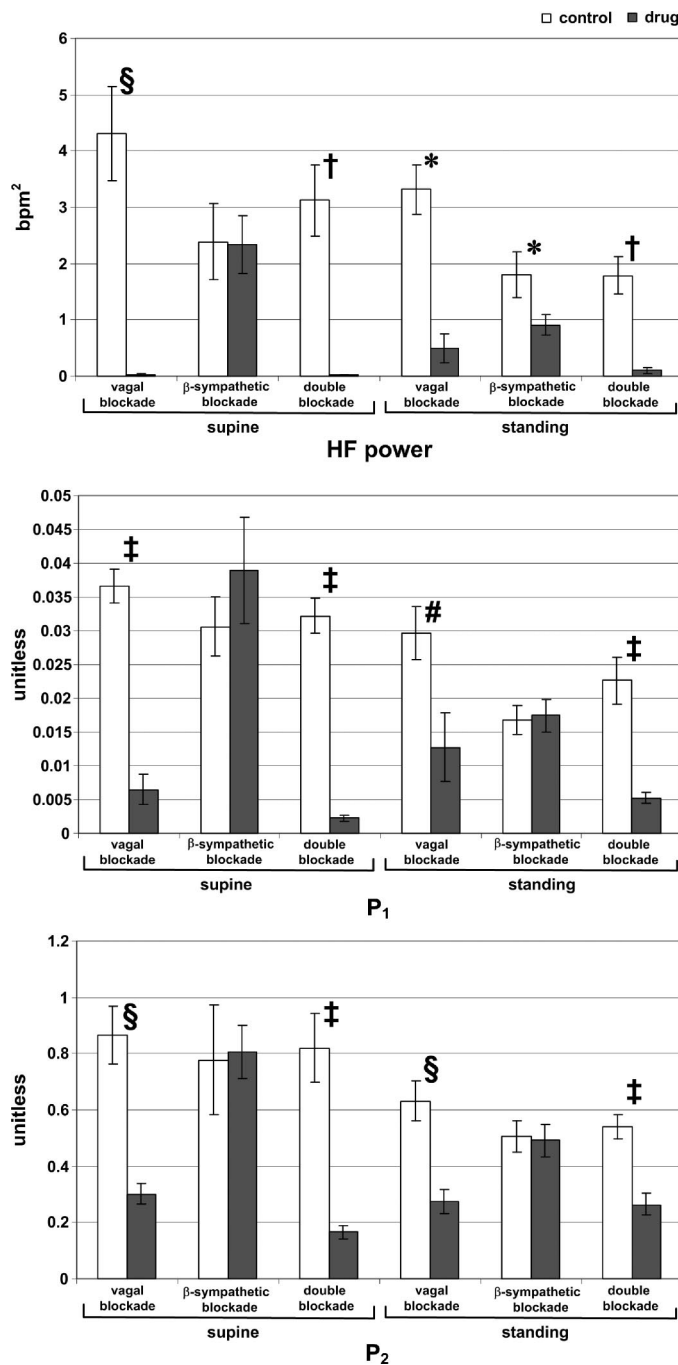
Fig. 5. Group average results (mean ± SE) for the conventional high-frequency (HF) power of HR variability and the P_1 and P_2 indexes of the PNS derived by multisignal analysis of cardiorespiratory variability from 14 human subjects before (control) and after vagal, β-sympathetic, and double (vagal + β-sympathetic) blockade in the supine and standing postures. #$P <$ 0.10; *$P <$ 0.05; §$P <$ 0.01; †$P <$ 0.005; ‡$P <$ 0.001.

resting beat-to-beat fluctuations in HR, ABP, and ILV so as to estimate the autonomically mediated ILV→HR and ABP→HR transfer functions (see Fig. 2). Then, we separated each estimated transfer function in the time domain into an early and fast PNS component and delayed and sluggish SNS component (see Fig. 1). Finally, we computed scalar indexes of the PNS and SNS from the respective time domain or impulse response components. In this way, the overlap of the SNS and

PNS in the frequency domain may be circumvented, and the input contributions to HR may be eliminated. Analogous to the HR power spectral indexes, the derived indexes represent the responses of the CANS to unity changes in their inputs about the mean value and therefore do not reflect basal autonomic tone. Whereas there have been many studies of ILV→HR and ABP→HR couplings (see, e.g., Ref. 39), this study goes one step further by attempting to separately quantify the two CANS from the couplings. We note that this basic idea was initially introduced by us with co-workers in the APPENDIX of Ref. 38. In that study, we specifically proposed the method described herein to separate the ILV→HR impulse response into PNS and SNS indexes (P_1 and S_1). In this study, we introduced a method to decompose the less straightforward ABP→HR impulse response into PNS and SNS indexes (P_2 and S_2). In addition, and significantly, we evaluated, for the very first time, both pairs of indexes, specifically in the context of selective pharmacological autonomic nervous blockade in 14 human subjects. Our results showed that, at the expense of requiring additional measurements, the newly derived indexes, particularly P_2 and S_2, were better than the HF power, LF/HF ratio, and normalized LF power of HR variability in correctly predicting the known drug effects on the PNS and SNS (see Figs. 5 and 6).

In theory, the HF power of HR variability, which is mediated solely by the PNS, should be a useful vagal index, unless there is a significant change in respiratory effort. The experimental results of the present study confirm this theory. In particular, HF power was able to correctly predict the effects of vagal and double blockade in the supine and standing postures and β-sympathetic blockade in the supine posture wherein no significant change in the HF power of ILV fluctuations occurred. However, this PNS index actually decreased after β-sympathetic blockade in the standing posture, likely due to the significant reduction ($P <$ 0.05) in the HF power of ILV fluctuations. The change in HF power of ILV fluctuations during only this particular condition may be related to postural factors, bronchoconstriction resulting from β-sympathetic blockade, and/or the random-interval breathing protocol. Regardless of the mechanism, this result suggests that the HF power will be an ineffective marker of the PNS in situations where breathing is altered (e.g., exercise).

As discussed above, a basic idea of the P_1 and P_2 indexes is to eliminate the contributions of respiration so as to result in more specific measures of the PNS. Our results showed that both of these indexes were, in fact, able to correctly predict the effects of all studied autonomic nervous blockade conditions. The P_2 index was a better predictor than the P_1 index in terms of statistical significance but did not decrease as much after vagal and double blockade.

In theory, without confounding input alterations, the LF/HF ratio of HR variability should generally be a good measure of the SNS when only the SNS changes or the SNS and PNS change in opposite directions and a poor marker when only the PNS changes or both CANS change in the same direction. Indeed, our results showed that this index was able to correctly predict the effects of β-sympathetic blockade but not double blockade on the SNS. The index even showed a tendency to increase after double blockade in the standing posture. In addition, the LF/HF ratio increased by a factor of two after vagal blockade, although not to any level of statistical signif-
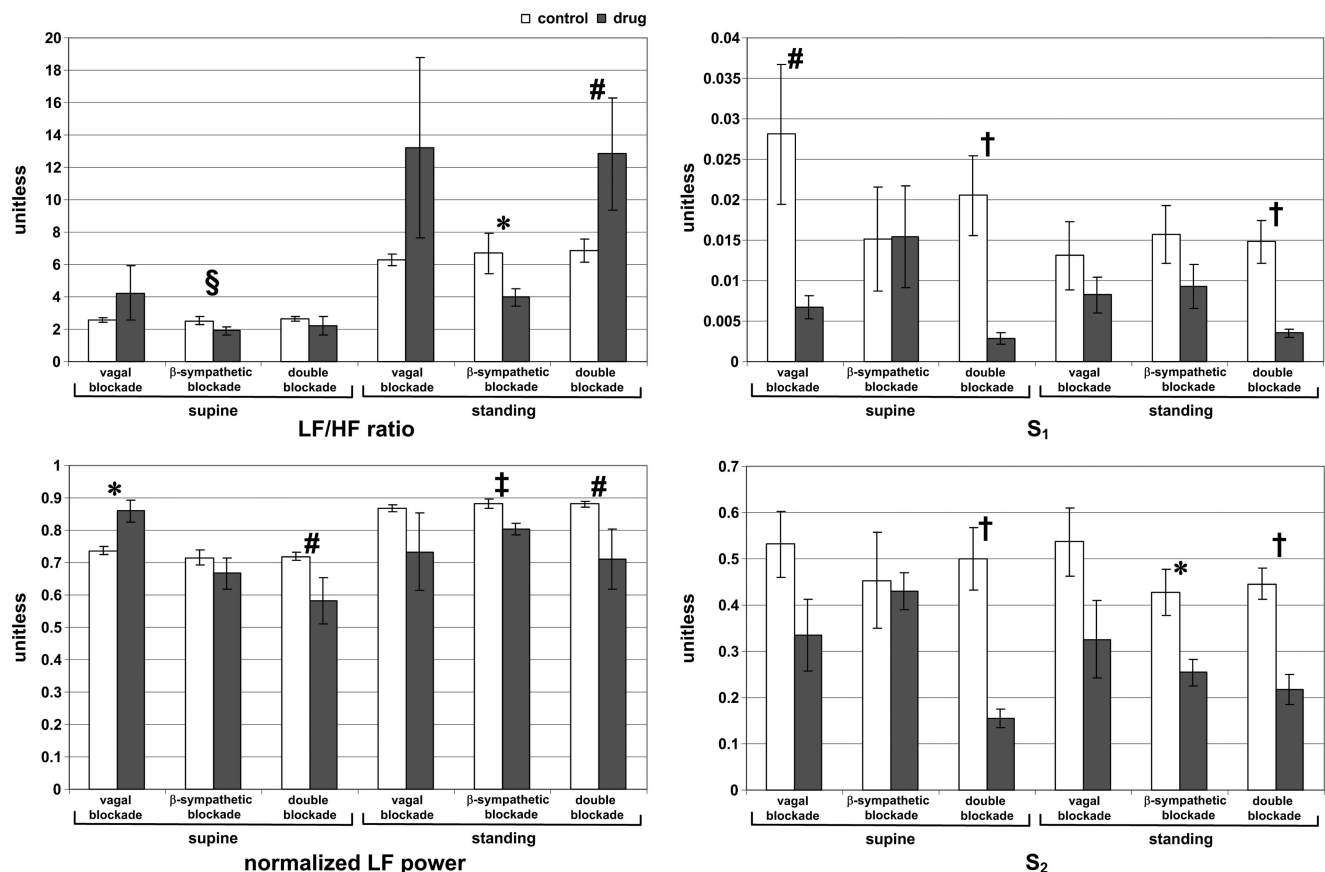
Fig. 6. Group average results (mean ± SE) for the conventional low frequency (LF)-to-HF ratio (LF/HF ratio) and normalized LF power of HR variability and the S_1 and S_2 indexes of the SNS derived by multisignal analysis of cardiorespiratory variability from 14 human subjects before (control) and after vagal, β-sympathetic, and double (vagal + β-sympathetic) blockade in the supine and standing postures. $\#P < 0.10$; $*P < 0.05$; $\S P < 0.01$; $\dagger P < 0.005$; $\ddagger P < 0.001$.

icance due to the large variance resulting from a division by zero-like effect. Overall, the LF/HF ratio appeared to be a somewhat better marker of sympathovagal balance in the present study, which is consistent with its original intention (22). However, we note that even if it were a perfect index of sympathovagal balance and the HF power were a perfect index of the PNS, they could not, in general, be utilized in tandem to quantify the SNS. For example, if the LF/HF ratio increased while the HF power decreased, this could indicate that the SNS was enhanced, remained the same, or was diminished but not to the extent of the PNS.

The normalized LF power of HR variability differs from the LF/HF ratio in that it includes LF power in the denominator [i.e., LF/(LF+HF) (31)]. In theory, this extra term should improve the ability to predict the effects of double blockade on the SNS (as the term will not go exactly to 0 in practice) and should markedly blunt changes following vagal and β-sympathetic blockade. Consistent with this theory, the normalized LF power was superior to the LF/HF ratio in predicting the effects of double blockade on the SNS and inferior in predicting the effects of β-sympathetic blockade. Moreover, the normalized LF power did not change as much as the LF/HF ratio after vagal blockade. However, the increase in the former index following vagal blockade in the supine posture actually showed statistical significance because of the reduced variance due to the presence of the extra denominator term. Overall, the nor-

malized LF power appeared to be a better index of the SNS than sympathovagal balance in our study.

Like the HF power of HR variability, the predictive capacity of both the LF/HF ratio and normalized LF power can, in theory, be adversely affected by alterations in the inputs to HR. In our study, the LF and HF powers of the ABP and ILV input fluctuations did significantly decrease during some of the experimental conditions. However, the contributions of these input changes to the LF/HF ratio and normalized LF power were generally more difficult to interpret.

As discussed above, the basic idea of the S_1 and S_2 indexes is to circumvent the frequency domain overlap of the SNS and PNS, while eliminating input contributions, by separating autonomically mediated transfer functions in the time domain using physiological knowledge and thereby arrive at more effective markers of the SNS. Indeed, the S_1 index decreased to a larger degree after double blockade and with a greater level of statistical significance than the normalized LF power. However, this SNS index did not decrease following β-sympathetic blockade and actually decreased after vagal blockade in the supine posture. Thus, the S_1 index did not provide an overall improved measure of the SNS in our study. On the other hand, the S_2 index did enhance the ability to predict the known drug effects on the SNS. This index correctly decreased following double blockade in both postures and β-sympathetic blockade in the standing posture and did not change after vagal blockade

in the two postures. It was only unable to identify a statistically significant decrease after β-sympathetic blockade in the supine posture, perhaps because sympathetic nervous outflow is very low in this posture (26). Note that even the LF/HF ratio only slightly decreased during this experimental condition. We hypothesize that the improved performance of the S_2 index over the S_1 index was due to differences in the frequency content of ABP and ILV. In particular, the LF ILV fluctuations may have been insufficient to accurately identify the sluggish SNS component of the ILV→HR impulse response. That is, even though the ILV fluctuations here were induced by a random-interval breathing protocol, the probability density of the respiratory intervals decreased exponentially with interval length (7). In contrast, the naturally occurring LF ABP fluctuations appear to have been enough for more reliable estimation of the SNS component of the ABP→HR impulse response.

The major aim of this study was to highlight the enhanced ability of our multisignal analysis of cardiorespiratory variability over HR power spectral analysis in correctly predicting large changes in the CANS induced by selective pharmacological autonomic nervous blockade. However, our results also revealed the capacity of these indexes to predict postural changes. In particular, all three PNS indexes correctly decreased upon standing in the control condition (see Fig. 5), whereas only the LF/HF ratio and normalized LF power correctly increased upon standing in the control condition (see Fig. 6). This result further suggests that the S_1 and S_2 indexes may not be as sensitive to smaller SNS changes. This insensitivity could be partly due to any nonautonomic nervous contributions to the ILV→HR and ABP→HR impulse responses such as mechanical modulation of the sinoatrial node by respiration (9) and variations in baroreceptor and sinoatrial node responsiveness (28). Future attempts to eliminate nonautonomic nervous contributions from the impulse responses [e.g., as proposed by Porta et al. (28)] may increase the sensitivity of the indexes.

Random-interval breathing was employed in this study to enhance the reliability of the estimated ILV→HR and ABP→HR impulse responses. This protocol is not utilized in standard HR variability analysis and could have negatively impacted the performance of the HR power spectral indexes. However, as described above, the results of these indexes reported herein are consistent with expectation based on previous spontaneous or controlled breathing studies. We therefore believe that these results are generally representative of what would have been obtained with conventional breathing protocols. However, we do speculate that some of the detailed aspects of the results may have been affected. For example, conventional breathing may have reduced the variance of the LF/HF ratio during vagal blockade and therefore result in a statistically significant increase in this index following vagal blockade. This result would have made the LF/HF ratio a much better index of sympathovagal balance but an even poorer index of the SNS and thereby better demonstrate the superiority of the S_2 index as a marker of the SNS.

Our multisignal analysis of cardiorespiratory variability has certain advantages and disadvantages with respect to other recently proposed analyses mentioned above aiming to likewise derive improved indexes of the PNS and SNS. The blind source separation analyses of HR and ABP variability as well

as HR and QT interval variability by Vetter et al. (33, 34) are based on the generally invalid assumption that the two CANS operate independently of each other. Our multisignal analysis is theoretically advantageous in that it makes no assumption about the relationship of the PNS and SNS. However, the blind source separation analyses have the practical advantage of requiring fewer measurements. The principal dynamic mode analysis of HR variability by Chon and co-workers (40, 41) is based on a nonlinear expansion. Remarkably, these investigators were able to show that the first two principal dynamic modes of the estimated first- and second-order Volterra kernels (calculated by invoking orthogonality) just happened to correspond to the PNS and SNS in their random-interval breathing datasets. Our multisignal analysis is theoretically advantageous in that it is physiologically based. Furthermore, it potentially has the practical advantage of not being reliant on random-interval breathing, since it is not a nonlinear analysis, which generally has more stringent demands on the frequency content of the inputs (19), employs the parsimonious weighted-principal component regression method (see the APPENDIX), and is most effective with respect to the ABP→HR impulse response (i.e., the P_2 and S_2 indexes). On the other hand, the principal dynamic mode analysis has the practical advantage of requiring only a surface ECG measurement and may be theoretically advantageous in terms of extracting nonlinear information from HR variability. Future comparisons of our multisignal analysis with the blind source separation and principal dynamic mode analyses during spontaneous breathing and random-interval breathing are certainly warranted.

Potential applications of our multisignal analysis of cardiorespiratory variability include any research or clinical setting in which continuous ABP, HR, and ILV or at least continuous ABP and surface ECGs are available [as ILV may potentially be estimated from surface ECGs (20)]. An example of such a clinical setting is the intensive care unit wherein HR power spectral indexes, as mentioned above, have been shown to be predictive of patient outcome (36). Further demonstrations of the multisignal analysis in providing improved markers of the PNS and SNS as well as enhanced association with mortality and disease are needed, particularly under spontaneous breathing conditions, to ultimately realize these applications.

APPENDIX

The weighted-principal component regression method utilized herein to estimate the parameter sets specifying the ILV→HR and ABP→HR impulse responses in *Eq. 1* is described in detail in Ref. 37. We briefly review the major steps of this method below.

First, the AR parameters $\{a[i]\}$ in *Eq. 1* are initialized to 0, and the terms m, M, and N are set to values that are believed to encompass the actual durations of the ILV→HR and ABP→HR impulse responses (i.e., FIRs). (In this study, we set m, M, and N to -7, 42, and 50, respectively, thereby assuming that each FIR is no greater than 50 samples in duration and accounting for the noncausality of the ILV→HR impulse response.) Then, the upper model in *Eq. 1* is formed into a matrix equation by stacking each individual equation, corresponding to each discrete time n, one on top of the other as follows: $\mathbf{y} = \mathbf{X}\mathbf{h} + \mathbf{w}$, where $\mathbf{y}$, $\mathbf{h}$, and $\mathbf{w}$ are vectors, respectively, comprising the samples of HR, the two FIRs to be estimated ($\{g[i]\}$ and $\{h[i]\}$), and W_{HR}, whereas $\mathbf{X}$ is a matrix consisting of samples of delayed versions of ILV and ABP. Next, matrix $\mathbf{X}$ is postmultiplied by diagonal matrix $\mathbf{W}$, whose diagonal elements decay exponentially so as to assume that the current

output sample is more dependent on recent input samples than distant input samples. Then, the principal components of matrix **XW** ("weighted-principal components") are added into a regression structure, one at a time, in order of descending principal components and regressed on to vector **y** until the minimum description length criterion is minimized (17) so as to arrive at an estimate of vector **x** (i.e., the two FIRs). This calculation is repeated for various exponential weighting decay rates, with the one minimizing vector **w** in the least squares sense ultimately selected. Next, N_{HR} is calculated (i.e., $\mathbf{y} - \mathbf{Xh}$), and the AR parameters are estimated by standard linear least-squares minimization of W_{HR} in the lower model in *Eq. 1* (17). (For simplicity, in this study, P was set to 20. This value was justified by observing that W_{HR} was indeed generally white via standard autocorrelation analysis.) Finally, HR, ABP, and ILV are prefiltered using the estimated AR parameters, and the above steps are repeated until the estimated FIRs converge. Importantly, this method effectively represents the FIRs, asymptotically, with damped sinusoidal basis functions that reflect the dominant frequency content of the inputs. Thus, only a small number of basis functions (or weighted-principal components) should be needed, thereby decreasing the number of parameters to be estimated and thus the estimation error. (In this study, 20–25 basis functions were nominally used, which represents a >75% reduction in the number of estimated parameters.)
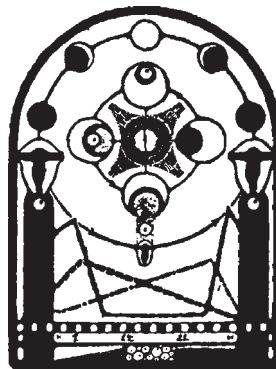
GRANTS

REFERENCES

1. **Akselrod S, Gordon D, Madwed JB, Snidman NC, Shannon DC, Cohen RJ.** Hemodynamic regulation: investigation by spectral analysis. *Am J Physiol Heart Circ Physiol* 249: H867–H875, 1985.
2. **Akselrod S, Gordon D, Ubel FA, Shannon DC, Barger AC, Cohen RJ.** Power spectrum analysis of heart rate fluctuation: a quantitative probe of beat-to-beat cardiovascular control. *Science* 213: 220–222, 1981.
3. **Armoundas AA, Feldman AB, Mukkamala R, Bin H, Mullen TJ, Belk PA, Lee YZ, Cohen RJ.** Statistical accuracy of a moving equivalent dipole method to identify sites of origin of cardiac electrical activation. *IEEE Trans Biomed Eng* 50: 1360–1370, 2003.
4. **Baselli G, Cerutti S, Badilini F, Biancardi L, Porta A, Pagani M, Lombardi F, Rimoldi O, Furlan R, Malliani R.** Model for the assessment of heart period and arterial pressure variability interactions and of respiration influences. *Med Biomed Eng Comput* 32: 143–152, 1994.
5. **Baselli G, Cerutti S, Civardi S, Malliani A, Pagani M.** Cardiovascular variability signals: towards the identification of aclosed-loop model of the neural control mechanisms. *IEEE Trans Biomed Eng* 35: 1033–1046, 1988.
6. **Berger RD, Akselrod S, Gordon D, Cohen RJ.** An efficient algorithm for spectral analysis of heart rate variability. *IEEE Trans Biomed Eng* 33: 900–904, 1986.
7. **Berger RD, Saul JP, Cohen RJ.** Assessment of autonomic response by broad-band respiration. *IEEE Trans Biomed Eng* 36: 1061–1065, 1989.
8. **Berger RD, Saul JP, Cohen RJ.** Transfer function analysis of autonomic regulation. I. Canine atrial rate response. *Am J Physiol Heart Circ Physiol* 256: H142–H152, 1989.
9. **Bernardi L, Keller F, Sanders M, Reddy PS, Griffith B, Meno F, Pinsky MR.** Respiratory sinus arrhythmia in the denervated human heart. *J Appl Physiol* 67: 1447–1455, 1989.
10. **Bigger JT Jr, Fleiss JL, Steinman RC, Rolnitzky LM, Kleiger RE, Rottman JN.** Frequency domain measures of heart period variability and mortality after myocardial infarction. *Circulation* 85: 164–171, 1992.
11. **Binkley PF, Nunziata E, Haas GJ, Nelson SD, Cody RJ.** Parasympathetic withdrawal is an integral component of autonomic imbalance in congestive heart failure: demonstration in human subjects and verification in a paced canine model of ventricular failure. *J Am Coll Cardiol* 18: 464–472, 1991.
12. **Chon KH, Mullen TJ, Cohen RJ.** A dual-input nonlinear system analysis of autonomic modulation of heart rate. *IEEE Trans Biomed Eng* 43: 530–544, 1996.
13. **Dougherty CM, Burr RL.** Comparison of heart rate variability in survivors and nonsurvivors of sudden cardiac arrest. *Am J Cardiol* 70: 441–448, 1992.
14. **Freeman R, Saul JP, Roberts MS, Berger RD, Broadbridge C, Cohen RJ.** Spectral analysis of heart rate in diabetic autonomic neuropathy. A comparison with standard tests of autonomic function. *Arch Neurol* 48: 185–190, 1991.
15. **Guzzetti S, Dassi S, Pecis M, Casati R, Masu AM, Longoni P, Tinelli M, Cerutti S, Pagani M, Malliani A.** Altered pattern of circadian neural control of heart period in mild hypertension. *J Hypertens* 9: 831–838, 1991.
16. **Langewitz W, Rüddel H, Schächinger H.** Reduced parasympathetic cardiac control in patients with hypertension at rest and under mental stress. *Am Heart J* 127: 122–128, 1994.
17. **Ljung L.** *System Identification: Theory for the User.* Englewood Cliffs, NJ: Prentice-Hall, 1987.
18. **Malliani A, Julien C, Billman GE, Cerutti S, Piepoli MF, Bernardi L, Sleight P, Cohen MA, Tan CO, Laude D, Elstad M, Toska K, Evans JM, Eckberg DL.** Cardiovascular variability is/is not an index of autonomic control of circulation. *J Appl Physiol* 101: 684–688, 2006.
19. **Marmarelis PZ, Marmarelis VZ.** *Analysis of Physiological Systems: the White-Noise Approach.* New York: Plenum, 1978.
20. **Moody GB, Mark RG, Zoccola A, Mantero S.** Derivation of respiratory signals from multi-lead ECGs. *Comp Cardiol* 12: 113–116, 1985.
21. **Mullen TJ, Appel ML, Mukkamala R, Mathias JM, Cohen RJ.** System identification of closed-loop cardiovascular control: effects of posture and autonomic blockade. *Am J Physiol Heart Circ Physiol* 272: H448–H461, 1997.
22. **Pagani M, Lombardi F, Guzzetti S, Rimoldi O, Furlan R, Pizzinelli P, Sandrone G, Malfatto G, Dell'Orto S, Piccaluga E.** Power spectral analysis of heart rate and arterial pressure variabilities as a marker of sympatho-vagal interaction in man and conscious dog. *Circ Res* 59: 178–193, 1986.
23. **Pagani M, Malfatto G, Pierini S, Casati R, Masu AM, Poli M, Guzzetti S, Lombardi F, Cerutti S, Malliani A.** Spectral analysis of heart rate variability in the assessment of autonomic diabetic neuropathy. *J Auton Nerv Syst* 23: 143–153, 1988.
24. **Parati G, Mancia G, Rienzo MD, Castiglioni P, Taylor JA, Studinger P.** Point:Counterpoint: Cardiovascular variability is/is not an index of autonomic control of circulation. *J Appl Physiol* 101: 676–682, 2006.
25. **Parati G, Saul JP, Di Rienzo M, Mancia G.** Spectral analysis of blood pressure and heart rate variability in evaluating cardiovascular regulation. A critical appraisal. *Hypertension* 25: 1276–1286, 1995.
26. **Pomeranz B, Macaulay RJ, Caudill MA, Kutz I, Adam D, Gordon D, Kilborn KM, Barger AC, Shannon DC, Cohen RJ, Benson H.** Assessment of autonomic function in humans by heart rate spectral analysis. *Am J Physiol Heart Circ Physiol* 248: H151–H153, 1985.
27. **Porta A, Baselli G, Rimoldi O, Malliani A, Pagani M.** Assessing baroreflex gain from spontaneous variability in conscious dogs: role of causality and respiration. *Am J Physiol Heart Circ Physiol* 279: H2558–H2567, 2000.
28. **Porta A, Montano N, Pagani M, Malliani A, Baselli G, Somers VK, van de Borne P.** Non-invasive model-based estimation of the sinus node dynamic properties from spontaneous cardiovascular variability series. *Med Biol Eng Comput* 41: 52–61, 2003.
29. **Saul JP, Arai Y, Berger RD, Lilly LS, Colucci WS, Cohen RJ.** Assessment of autonomic regulation in chronic congestive heart failure by heart rate spectral analysis. *Am J Cardiol* 61: 1292–1299, 1988.
30. **Saul JP, Berger RD, Albrecht P, Stein SP, Chen MH, Cohen RJ.** Transfer function analysis of the circulation: unique insights into cardiovascular regulation. *Am J Physiol Heart Circ Physiol* 261: H1231–H1245, 1991.
31. **Task Force of the European Society of Cardiology, North American Society of Pacing Electrophysiology.** Heart rate variability: standards of measurement, physiological interpretation, and clinical use. *Circulation* 93: 1043–1065, 1996.
32. **Triedman JK, Perrott MH, Cohen RJ, Saul JP.** Respiratory sinus

arrhythmia: time domain characterization using autoregressive moving average analysis. *Am J Physiol Heart Circ Physiol* 268: H2232–H2238, 1995.

33. **Vetter R, Vesin JM, Celka P, Scherrer U.** Observer of the human cardiac sympathetic nerve activity using noncausal blind source separation. *IEEE Trans Biomed Eng* 46: 322–330, 1999.

34. **Vetter R, Virag N, Vesin JM, Celka P, Scherrer U.** Observer of autonomic cardiac outflow based on blind source separation of ECG parameters. *IEEE Trans Biomed Eng* 47: 578–582, 2000.

35. **Wellstead PE, Edmunds JM.** Least-squares identification of closed-loop systems. *Int J Control* 21: 689–699, 1975.

36. **Winchell RJ, Hoyt DB.** Spectral analysis of heart rate variability in the ICU: a measure of autonomic function. *J Surg Res* 63: 11–16, 1996.

37. **Xiao X, Mukkamala R, Cohen RJ.** A weighted-principal component regression method for the identification of physiologic systems. *IEEE Trans Biomed Eng* 53: 1521–1530, 2006.

38. **Xiao X, Mukkamala R, Sheynberg N, Grenon SM, Ehrman MD, Mullen TJ, Ramsdell CD, Williams GH, Cohen RJ.** Effects of simulated microgravity on closed-loop cardiovascular regulation and orthostatic intolerance: analysis by means of system identification. *J Appl Physiol* 96: 489–497, 2004.

39. **Xiao X, Mullen TJ, Mukkamala R.** System identification: a multi-signal approach for probing neural cardiovascular regulation. *Physiol Meas* 26: R41–R71, 2005.

40. **Zhong Y, Jan K, Ju KH, Chon KH.** Quantifying cardiac sympathetic and parasympathetic nervous activities using principal dynamic modes analysis of heart rate variability. *Am J Physiol Heart Circ Physiol* 291: H1475–H1483, 2006.

41. **Zhong Y, Wang H, Ju KH, Jan KM, Chon KH.** Nonlinear analysis of the separate contributions of autonomic nervous systems to heart rate variability using principal dynamic modes. *IEEE Trans Biomed Eng* 51: 255–262, 2004.

Continuous cardiac output monitoring in humans by invasive and noninvasive peripheral blood pressure waveform analysis

Zhenwei Lu and Ramakrishna Mukkamala

You might find this additional information useful...

This article cites 33 articles, 14 of which you can access free at:
http://jap.physiology.org/cgi/content/full/101/2/598#BIBL

Medline items on this article's topics can be found at http://highwire.stanford.edu/lists/artbytopic.dtl
on the following topics:

- Medicine .. Blood Pressure
- Medicine .. Cardiac Output
- Medicine .. Emergency Cardiovascular Treatment
- Medicine .. General / Adult
- Medicine .. Critical Care
- Veterinary Science .. Humans

Updated information and services including high-resolution figures, can be found at:
http://jap.physiology.org/cgi/content/full/101/2/598

Additional material and information about *Journal of Applied Physiology* can be found at:
http://www.the-aps.org/publications/jappl

This information is current as of July 19, 2006 .

TRANSLATIONAL PHYSIOLOGY

Continuous cardiac output monitoring in humans by invasive and noninvasive peripheral blood pressure waveform analysis

Zhenwei Lu and Ramakrishna Mukkamala

Department of Electrical and Computer Engineering, Michigan State University, East Lansing, Michigan

Lu, Zhenwei, and Ramakrishna Mukkamala. Continuous cardiac output monitoring in humans by invasive and noninvasive peripheral blood pressure waveform analysis. *J Appl Physiol* 101: 598–608, 2006; doi:10.1152/japplphysiol.01488.2005.—We present an evaluation of a novel technique for continuous (i.e., automatic) monitoring of relative cardiac output (CO) changes by long time interval analysis of a peripheral arterial blood pressure (ABP) waveform in humans. We specifically tested the mathematical analysis technique based on existing invasive and noninvasive hemodynamic data sets. With the former data set, we compared the application of the technique to peripheral ABP waveforms obtained via radial artery catheterization with simultaneous thermodilution CO measurements in 15 intensive care unit patients in which CO was changing because of disease progression and therapy. With the latter data set, we compared the application of the technique to noninvasive peripheral ABP waveforms obtained via a finger-cuff photoplethysmography system with simultaneous Doppler ultrasound CO measurements made by an expert in 10 healthy subjects during pharmacological and postural interventions. We report an overall CO root-mean-squared normalized error of 15.3% with respect to the invasive hemodynamic data set and 15.1% with respect to the noninvasive hemodynamic data set. Moreover, the CO errors from the invasive and noninvasive hemodynamic data sets were only mildly correlated with mean ABP (ρ = 0.41, 0.37) and even less correlated with CO (ρ = −0.14, −0.17), heart rate (ρ = 0.04, 0.19), total peripheral resistance (ρ = 0.38, 0.10), CO changes (ρ = −0.26, −0.20), and absolute CO changes (ρ = 0.03, 0.38). With further development and successful prospective testing, the technique may potentially be employed for continuous hemodynamic monitoring in the acute setting such as critical care and emergency care.

Doppler ultrasound; Finapres; pulse contour analysis; radial artery catheterization; thermodilution

THE STANDARD CLINICAL METHOD for measuring cardiac output (CO) is currently thermodilution. After insertion of a pulmonary artery catheter, this method involves injecting a bolus of cold saline in the right atrium, measuring temperature downstream in the pulmonary artery, and computing the average CO on the basis of conservation laws (9). Because an operator is required to administer the bolus injection, thermodilution measurements may only be obtained intermittently. However, perhaps a more significant shortcoming of thermodilution is that its high level of invasiveness limits its use to only a minority (e.g., 10–20%) of all critically ill patients (32). In fact, thermodilution usage may decline to even lower levels because of

recent reports indicating that the invasive pulmonary artery catheter may not improve patient outcome (e.g., Ref. 35). Thus the need for a less invasive CO monitoring method may become even more urgent in the future. Although Doppler ultrasound and transthoracic bioimpedance have been introduced as noninvasive CO monitoring methods, neither of them has been able to replace thermodilution. Doppler ultrasound methods, which measure the Doppler shift in the frequency of an ultrasound beam reflected from the flowing aortic blood (9), require an expert operator to stabilize an external ultrasound transducer as well as expensive capital equipment (19). Transthoracic bioimpedance, which involves measuring changes in the electrical impedance of the thorax during the cardiac cycle (9, 19), may not be sufficiently accurate, especially in critically ill patients who often have excessive lung fluids (7).

On the other hand, peripheral arterial blood pressure (ABP), which is related to CO through the arterial tree, may be measured reliably and continuously via radial artery catheterization, which is less invasive than pulmonary artery catheterization. Indeed, this relatively safe procedure is performed in a majority (e.g., 50–80%) of all critically ill patients (33). Moreover, over the past few decades, totally noninvasive methods have been developed and refined to continuously measure peripheral ABP on the basis of finger-cuff photoplethysmography (16) and arterial tonometry (17). These noninvasive methods are even available as commercial systems at present (see, for example, the Finometer and Portapres, Finapres Medical Systems, The Netherlands and the T-Line Blood Pressure Monitoring System, Tensys Medical, San Diego, CA).

Beginning with the seminal work of Frank in 1899 (13) and Erlanger and Hooker in 1904 (12), numerous cardiovascular researchers have sought analysis techniques to compute CO to within a constant scale factor from the contour of ABP waveforms so as to permit continuous (i.e., automatic and without the need for an operator), quantitative measurements of relative changes in CO and expand the clinical monitoring of CO. (Note that some researchers have also sought to calibrate the proportional CO estimates via empirical formula.) Although a wide variety of "pulse contour analysis" techniques have been proposed, they are all conceptually the same to the extent that the waveform analysis is performed only over time scales within a cardiac cycle (e.g., see Fig. 1) (26). However, over such short time scales, peripheral ABP waveforms are domi-
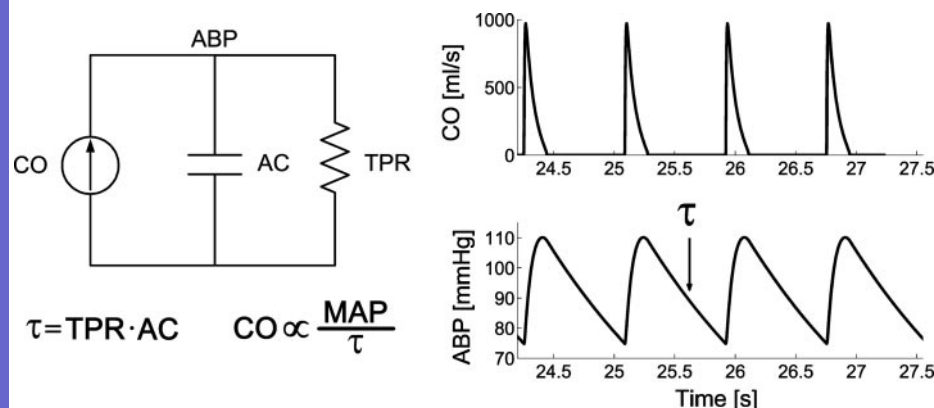
Journal of Applied Physiology

Fig. 1. Previous technique for monitoring cardiac output (CO) by analysis of an arterial blood pressure (ABP) waveform (6, 31). According to the windkessel model (*left*), ABP should decay like a pure exponential during each diastolic interval with a time constant (τ) equal to the product of the total peripheral resistance (TPR) and the nearly constant arterial compliance (AC). Thus the technique involves first fitting a monoexponential function to the diastolic interval of each ABP pulse to determine τ (*right*) and then dividing the time-averaged ABP (MAP) with τ to estimate proportional CO. Figure from Ref. 26; © 2006 IEEE.

nated by highly complex waves propagating back and forth in the distributed arterial tree (28). Thus the previous analysis techniques have generally proven to be too inaccurate (in terms of estimating proportional CO) for clinical use.

Our ongoing hypothesis is that proportional CO may be more accurately monitored from all ABP variations, especially those occurring over time scales greater than a cardiac cycle. This novel hypothesis originates from transmission line theory, which predicts that the confounding effects of wave phenomena will diminish with increasing time scale (28). We have recently developed a technique that exploits this hypothesis to quantitatively monitor relative changes in CO by mathematically analyzing a single peripheral ABP waveform over long time intervals (about 6 min) (26). We have previously tested the technique in a set of acute swine experiments, and our CO estimates showed strong agreement with gold standard aortic flow probe CO measurements over a wide physiological range (26).

In this paper, we present an evaluation of the technique in humans based on previously published invasive and noninvasive hemodynamic data sets (10, 24, 25, 27). With these data, we were specifically able to compare the application of the technique to *1*) invasive peripheral ABP waveforms obtained via radial artery catheterization with reference thermodilution measurements in 15 intensive care unit (ICU) patients in which CO was changing because of disease progression and therapy, and *2*) noninvasive peripheral ABP waveforms obtained via a commercial finger-cuff photoplethysmography system with reference Doppler ultrasound measurements made by an expert in 10 healthy subjects in which CO was altered through pharmacological and postural interventions.

METHODS

Mathematical Analysis Technique

Our technique for monitoring relative CO changes by mathematically analyzing a peripheral ABP waveform was introduced in Ref. 26 and is described in detail therein. Here, we review the background, underlying concepts, and implementation of the technique from a physiological perspective while including its mathematical steps.
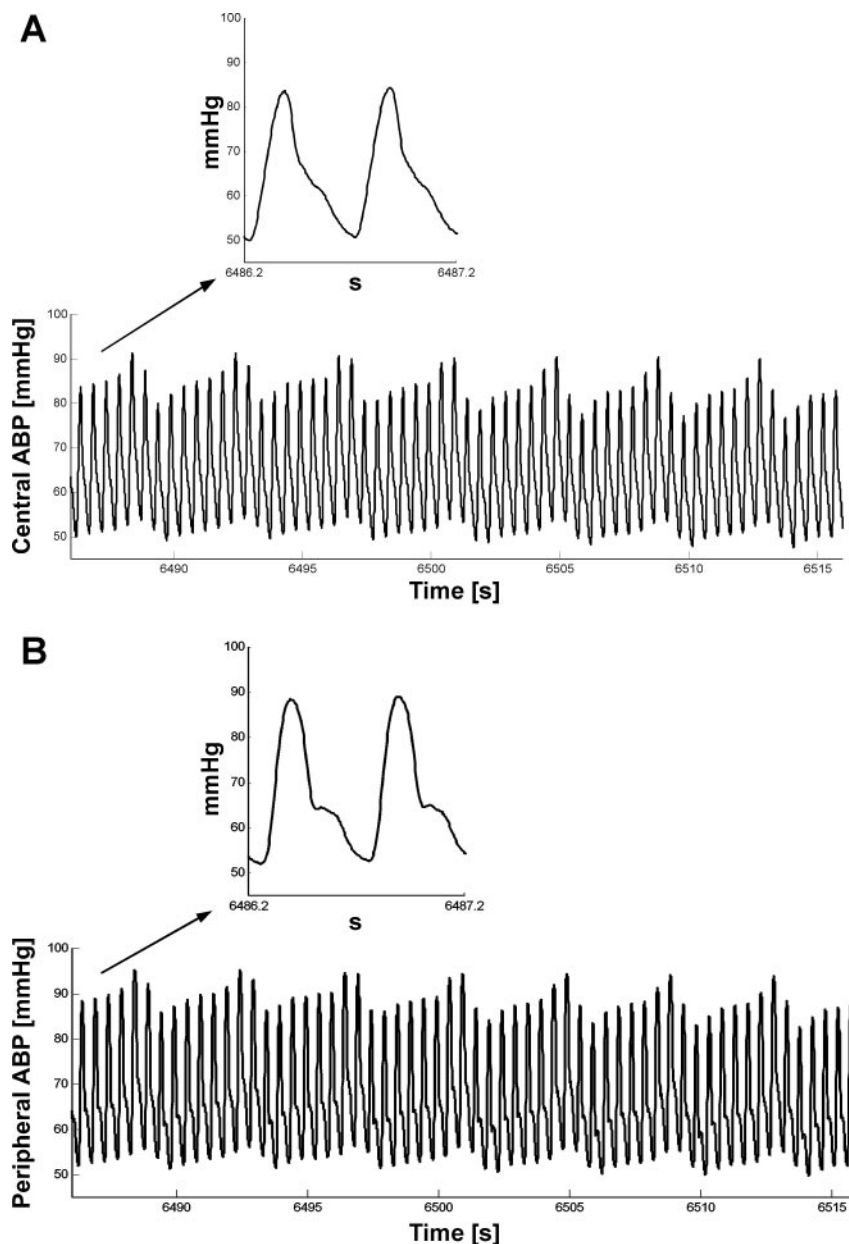
Background and underlying concepts. The technique that we have developed builds on the previous pulse contour analysis work of Bourgeois et al. (6) as well as Osborn et al. (31). These investigators assumed that the arterial tree could be well represented by a two-element windkessel model accounting for the lumped compliance of the large arteries (arterial compliance, AC) and the total peripheral resistance (TPR) of the small arteries (see electrical analog in Fig. 1). They further assumed that TPR does not vary within a diastolic

interval [as justified by the relatively slow local and autonomic nervous mechanisms responsible for modulating TPR (3, 14)] and that AC is approximately constant over a wide pressure range and on the time scale of days to months (see experimental evidence in Refs. 5, 6, 15, 26, 31, and DISCUSSION). On the basis of these assumptions, these investigators predicted that ABP should decay like a pure exponential during each diastolic interval with a time constant equal to the product of TPR and AC (windkessel time constant, τ). Thus their pulse contour analysis involved first fitting a monoexponential function to each diastolic ABP interval to measure τ and then dividing the time-averaged ABP with τ to compute CO to within a constant scale factor equal to 1/AC (see Fig. 1).

This pulse contour analysis proved to be successful when applied to ABP waveforms measured centrally in the aorta, because the diastolic interval of these waveforms can resemble an exponential decay after incisura (see Fig. 2). However, central ABP is rarely measured clinically because of the risk of blood clot formation and embolization. Moreover, in readily available peripheral ABP waveforms, an exponential diastolic decay is usually not apparent (see Fig. 2). Indeed, it is well known that the contour of the arterial pulse changes significantly as it traverses through the arterial tree (30). The reason is that the arterial tree is not simply a lumped system as the windkessel model suggests, but rather a complicated distributed system with impedance mismatches throughout due to vessel tapering, bifurcations, and caliber changes. Thus the diastolic (and systolic) intervals of peripheral ABP waveforms are corrupted by complex wave reflections that occur at each and every site of impedance mismatch. [Note that the complexity of these sites and their varying distances from the aorta result in reflected waves with large phasic differences, which can tend to mitigate the cumulative effects of these waves on the central ABP waveform, i.e., destructive interference (28).] The above pulse contour analysis therefore cannot be applied to readily measured peripheral ABP waveforms.

According to transmission line theory, however, the confounding effects of wave phenomena will diminish with increasing time scale. That is, the wave effects significantly obscure peripheral ABP waveforms over short time scales (high frequencies) without complicating the waveform over longer time scales (low frequencies). For example, consider the limiting case in which the time scale is sufficiently long such that the wavelengths of the propagating waves are much larger than the dimension of the arterial tree. At such time scales, the arterial tree acts as a single blood reservoir, and the windkessel model is therefore valid. So, for example, if pulsatile activity abruptly ceased, then peripheral ABP may eventually decay like a pure exponential as soon as the faster wave reflections vanish. This concept is demonstrated in Fig. 2, which illustrates two ABP waveforms measured at the same time but at different sites in the arterial tree. The short time scale or within-beat variations are different in the two ABP waveforms (Fig. 2, *A* and *B*, *top*, *inset*), as the characteristics of the highly complex wave effects differ at the two measurement sites. In contrast,

Fig. 2. Two ABP waveforms simultaneously measured centrally in the aorta (*A*) and peripherally in the radial artery (*B*) of a swine. The short time scale (intrabeat) variations in the ABP waveforms (*top, insets*) differ because of highly complex wave propagation and reflection. Note that these wave effects obscure pure exponential diastolic decays in the peripheral ABP waveform, and the previous cardiac output monitoring technique in Fig. 1 is therefore not applicable to these readily available waveforms. On the other hand, the long time scale (beat-to-beat) variations in the ABP waveforms (*bottom*) are more similar as the confounding effects of wave phenomena are less significant over these time scales. This implies that, if pulsatile activity were to abruptly cease, then peripheral ABP would eventually decay like a pure exponential (according to the time constant τ of the windkessel model of Fig. 1) once the faster wave effects vanished. Figure from Ref. 26; © 2006 IEEE.

the long time scale or beat-to-beat variations are much more similar (Fig. 2, *A* and *B*, *bottom*), as the confounding effects of wave phenomena are less significant over these time scales. (See, for example, Refs. 1 and 2 for a discussion of the mechanisms responsible for eliciting spontaneous, beat-to-beat ABP variations.)

Implementation steps. Our technique therefore mathematically analyzes a digitized peripheral ABP waveform over long time intervals (~6 min) to determine the pure exponential decay that would eventually result if pulsatile activity abruptly ceased. More specifically, the ABP response to a single, solitary cardiac contraction [$h(t)$ in Fig. 3] is estimated from the ABP waveform. Then, the windkessel time constant τ is determined by fitting a monoexponential function to the tail end of this response once the faster wave reflections have vanished (Fig. 3). Finally, proportional CO is computed via Ohm's law. Figure 3 illustrates the technique, which is specifically implemented in four steps as follows.

First, a signal representing the cardiac contractions [$x(t)$] is constructed from the ABP waveform on the basis of a slightly modified impulse ejection model. That is, $x(t)$ is formed as an impulse train in which each impulse is located at the onset of upstroke of an ABP pulse (resulting from a normal or ectopic beat) and has an area equal to the ensuing pulse pressure (PP; maximum ABP value minus the ABP value at the onset of upstroke) determined after low-pass filtering the ABP waveform (with a cutoff frequency of 2 Hz) to attenuate corruption due to high-frequency wave phenomena in the waveform (filtered PP).

Then, the impulse response function [$h(t)$] is estimated that, when convolved with $x(t)$, best fits the (unfiltered) ABP waveform [$y(t)$] in the least squares sense. [Note that, whereas ~6-min intervals of $x(t)$ and $y(t)$ are utilized to estimate $h(t)$, only a few seconds of $x(t)$ and $y(t)$ are shown in Fig. 3 for the purpose of clarity.] By definition, the estimated $h(t)$ represents the (scaled) ABP response to a single, solitary cardiac contraction. The impulse response function is specifically estimated according to the following autoregressive exogenous input equation:

$$y(t) = \sum_{k=1}^{m} a_k y(t-k) + \sum_{k=1}^{n} b_k x(t-k) + e(t) \qquad (1)$$
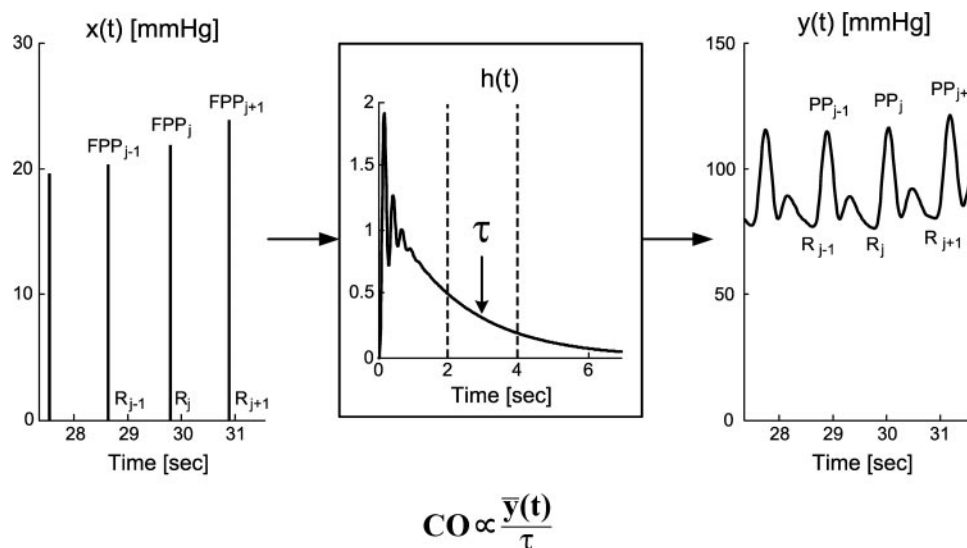
$$CO \propto \frac{\overline{y}(t)}{\tau}$$

Fig. 3. Our technique for monitoring CO from a peripheral ABP waveform (26). The measured ABP waveform [$y(t)$] is analyzed over long time intervals ($\sim$6-min) so as to mathematically estimate the ABP response to a single cardiac contraction [$h(t)$]. [Note that, although $\sim$6-min intervals of $y(t)$ are utilized to estimate $h(t)$, only a few seconds of $y(t)$ are illustrated for the purpose of clarity.] Then, the time constant τ of the windkessel model of Fig. 1 is determined by fitting a monoexponential function to the tail end of $h(t)$ once the faster wave reflections have vanished. Finally, proportional CO is computed by dividing the time-averaged ABP [$\overline{y}(t)$] with τ. In principle, τ is accurately determined by analysis of the subtle, beat-to-beat ABP variations in which the complex wave effects cease to be a significant factor (see Fig. 2). PP, pulse pressure; FPP, PP determined after low-pass filtering $y(t)$; R, onset time of upstroke of each ABP pulse; j, beat number; $x(t)$, a constructed cardiac contractions signal corresponding to the $\sim$6-min interval of $y(t)$; and $h(t)$, an estimated impulse response coupling $x(t)$ to $y(t)$. Figure adapted from Ref. 26; © 2006 IEEE.

where $e(t)$ is the unmeasured residual error, $\{a_k, b_k\}$ are unknown parameters, and m and n limit the number of these parameters (model order) (21). For a fixed model order, the parameters are estimated from $x(t)$ and $y(t)$ through the least squares minimization of the residual error, which has a closed-form solution (21). The model order is determined by minimizing the minimum description length (MDL) criterion, which penalizes for unnecessary parameters (21). [For the invasive hemodynamic data set below in which $x(t)$ and $y(t)$ were sampled at 90 Hz, the minimum MDL value was specifically identified over the model orders ranging from $m = n = 1$ to $m = n = 15$, with the final selected model order typically being no less than $m = n = 12$. For the noninvasive hemodynamic data set below in which $x(t)$ and $y(t)$ were sampled at 50 Hz, the minimum MDL value was identified over the model orders ranging from $m = n = 1$ to $m = n = 10$, with the final selected model order generally being no less than $m = n = 8$. These model order ranges were established on the basis of our previous swine study (26).] With the estimated parameters $\{\hat{a}_k, \hat{b}_k\}$, $h(t)$ is computed as follows:

$$h(t) = \sum_{k=1}^{m} \hat{a}_k h(t-k) + \sum_{k=1}^{n} \hat{b}_k \delta(t-k) \qquad (2)$$

where $\delta(t)$ is the unit impulse function.

Next, τ is determined over the interval of $h(t)$ ranging from 2 to 4 s after the time of its maximum value on the basis of the following exponential equation:

$$h(t) = Ae^{-t/\tau} + w(t) \qquad (3)$$

[This time interval was established empirically by almost always observing a pure exponential decay in $h(t)$ over this period in the hemodynamic data sets studied herein.] The parameters A and τ are estimated through the least squares minimization of the unmeasured residual error $w(t)$. This optimization problem is solved in closed form by log transformation of $h(t)$ (21). In theory, accurate determination of the windkessel time constant τ is achieved by virtue of $h(t)$ coupling the long time scale or beat-to-beat variations in $x(t)$ to $y(t)$ (see Fig. 4).

That is, the technique is not just trivially extrapolating the ABP waveform at the end of diastole.
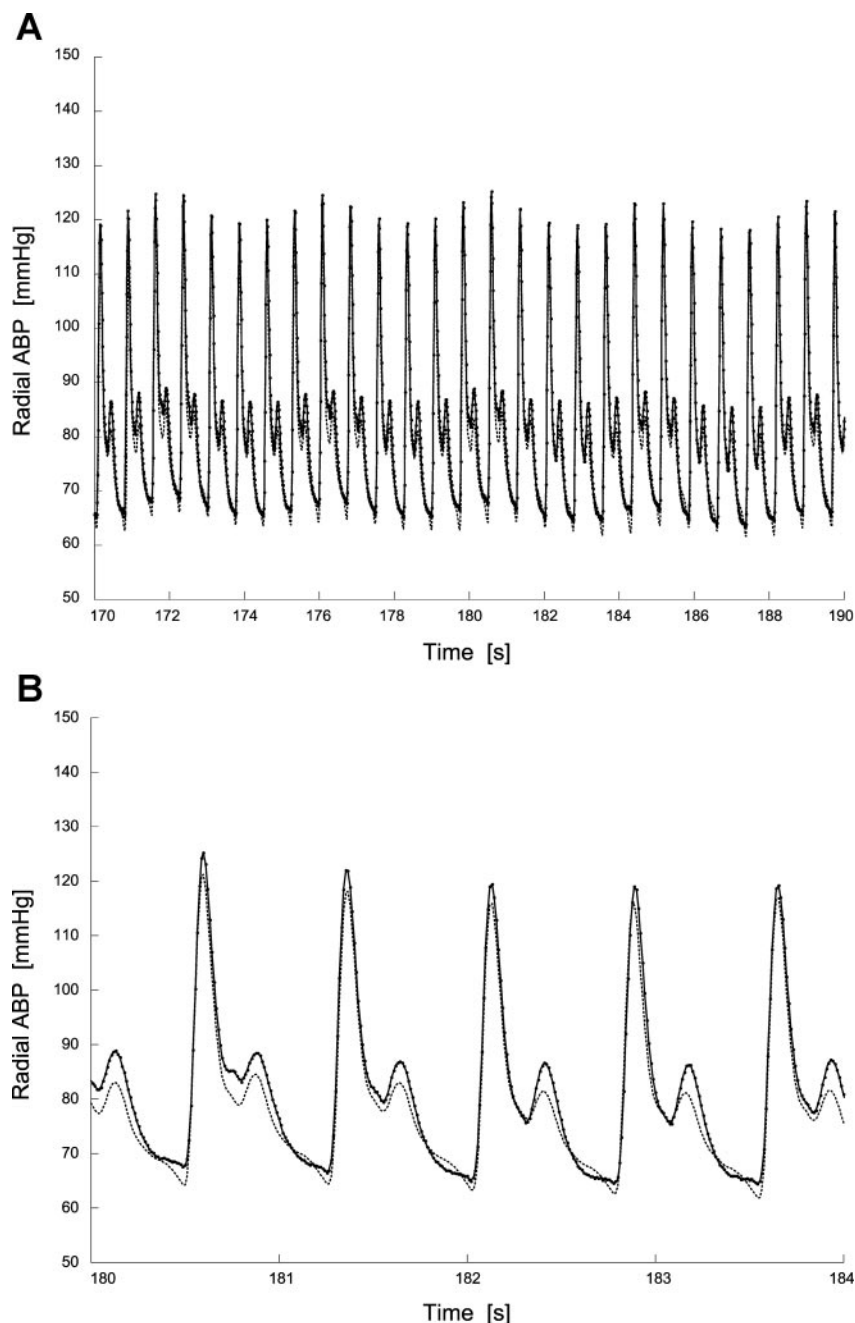
Finally, CO is computed to within a constant scale factor equal to 1/AC by dividing the time-averaged ABP with τ. Note that the above mathematical steps can easily be implemented in near real time with only a delay on order of a few seconds with a standard home personal computer.

Invasive Human Hemodynamic Data Set

The hemodynamic data utilized to evaluate the mathematical analysis technique with respect to human invasive peripheral ABP waveforms were obtained from the MIMIC (Multi-parameter Intelligent Monitoring for Intensive Care) database, which is described in detail elsewhere and freely available on the web (23–25). Briefly, this database includes 72 ICU patient records, typically ranging from 24 to 48 h in duration, that were archived from patient monitors in the medical, surgical, and cardiac intensive care units of the hospital formerly known as the Beth Israel Hospital, Boston, MA. Each of these records consists of continuous waveforms sampled at 125 Hz, such as invasive peripheral ABP via radial artery catheterization and surface ECG leads, as well as 1-min trends, such as thermodilution CO, mean ABP (MAP), and heart rate (HR). Sixteen of the 72 patient records were applicable to the present evaluation study, as they included *1*) radial ABP waveforms, and *2*) more than one reference thermodilution CO measurement. Within each of these records, CO was changing because of disease progression and therapy.

On the basis of these 16 MIMIC patient records, we created a data set for technique evaluation as follows. First, we downloaded from these records all of the distinct, 1-min thermodilution CO measurements and 6-min contiguous segments of the corresponding radial ABP waveforms (from 2.5 min preceding the 1-min CO measurements to 2.5 min after these measurements). Then, we visually examined each of the radial ABP waveforms and extracted the longest contiguous, artifact-free segment from each of these waveforms (see DISCUSSION). Finally, we excluded from the study all radial ABP waveforms that were less than 5 min in duration, had a significant

Fig. 4. Representative example of a measured (actual) and fitted (predicted) human invasive radial ABP waveform by the technique of Fig. 3. *A*: actual and predicted ABP waveforms over 20 s. *B*: close-up view over 4 s. Solid line, actual ABP waveform; dotted line, 1-step prediction ABP waveform; dashed line, full prediction ABP waveform (21). Because both predicted ABP waveforms correspond closely to the actual ABP waveform over time scales greater than a cardiac cycle, the subsequent estimation of the windkessel time constant τ and proportional cardiac output (see Fig. 3) should be accurate.

linear trend ($\geq$20 mmHg change), or represented the only waveform segment within a patient record (because the technique estimates changes in CO). Note that radial ABP waveforms with significant linear trends were removed from the study, because the corresponding thermodilution measurements, which strictly represent average CO over intervals of typically less than 1 min, are unlikely to provide an adequate reference CO to the entire 5- to 6-min period of unsteady ABP. A total of 101 pairs of simultaneous measurements of artifact-free, invasive radial ABP waveforms and reference thermodilution CO values from 15 ICU patients [10 men and 5 women; age: 67 $\pm$ 12 yr (mean $\pm$ SD)] remained for technique evaluation. Table 1 summarizes the clinical class and hemodynamic data for each of these patients.

Noninvasive Human Hemodynamic Data Set

The hemodynamic data utilized to evaluate the mathematical analysis technique with respect to human noninvasive peripheral ABP

waveforms were obtained from previous experiments designed to address different specific aims and are described in detail elsewhere (10, 27). Here, we briefly describe those aspects of the experiments that are relevant to the present study.

Ten healthy human volunteers [5 men and 5 women, age: 25 $\pm$ 4 yr (mean $\pm$ SD)] participated in the experiments. Each subject was instrumented for noninvasive measurement of a peripheral ABP waveform, instantaneous CO, and other cardiorespiratory signals. The peripheral ABP waveform was measured with a commercial finger-cuff photoplethysmography system (2300 Finapres continuous blood pressure monitor, Ohmeda; Englewood, CO), and instantaneous CO was measured according to a previously described Doppler ultrasound technique (11) implemented by an expert. Specifically, aortic blood velocity was measured with a bidirectional ultrasound Doppler velocimeter (CFM 750, GE Vingmed; Horten, Norway), which was operated in pulsed mode at 2 MHz with the hand-held transducer

Table 1. *Summary of the intensive care unit patient records and results of the invasive human hemodynamic data set*

Patient Record	Clinical Class	Number of Comparisons	CO Range, l/min	MAP Range, mmHg	TPR Range, PRU	HR Range, beats/min	CO RMSNE, %
041	Bleed	2	8.5–9.5	74–81	0.5–0.6	78–104	0.5
055	Respiratory failure	7	3.9–5.2	78–106	0.9–1.4	88–106	6.9
281	NA	4	3.7–4.9	94–99	1.2–1.6	100–114	6.8
410	Sepsis	7	4.3–9.4	74–97	0.6–1.1	60–94	22.3
411	Respiratory failure	6	3.2–4.6	84–94	1.2–1.7	50–61	14.4
451	CHF	5	4.1–5.8	51–58	0.5–0.9	74–84	15.0
453	Post-op valve	12	3.4–4.8	60–79	0.9–1.3	50–89	10.7
454	Post-op valve	5	3.7–4.8	67–74	0.9–1.1	49–70	5.4
456	Post-op CABG	8	3.8–8.5	57–100	0.6–1.0	67–108	22.5
474	NA	5	3.8–4.4	72–79	1.1–1.2	86–94	15.6
476	Post-op CABG	6	4.2–4.6	58–71	0.8–0.9	90–105	11.2
477	Post-op CABG	6	4.5–6	54–75	0.6–0.8	79–111	10.6
480	Post-op CABG	6	5–6.7	63–75	0.6–0.8	85–112	11.1
484	NA	9	5.1–7.5	62–78	0.6–0.8	79–96	12.4
485	NA	13	2.9–4.7	69–87	1.0–1.8	94–126	23.0
TOTAL		101	2.9–9.5	51–106	0.5–1.8	49–126	15.3

The technique of Fig. 3 as applied to 101 invasive radial arterial blood pressure waveform segments from 15 intensive care unit patients achieved an overall cardiac output (CO) root-mean-squared normalized error (RMSNE) of 15.3% with respect to reference thermodilution measurements. MAP, mean arterial blood pressure; TPR, total peripheral resistance; HR, heart rate; CHF, congestive heart failure; CABG, coronary artery bypass graft; NA, not available; Post-op, postoperative.

placed on the suprasternal notch. The area of the rigid aortic ring was determined in a separate session by parasternal sector-scanner imaging (CFM-750, GE Vingmed). Instantaneous CO was then calculated via the product of the measured instantaneous maximum blood velocity and the area of the aortic valve orifice (see DISCUSSION).

Each instrumented subject was studied on 2 separate days, before and after the administration of atropine (0.04 mg/kg) and/or propranolol (14.6 mg) during 4° head-down tilt, supine, and 30° upright tilt postures, for a total of 10 experimental conditions. Specifically, on 1 day, ~6-min intervals of the noninvasive measurements were continuously recorded while the subject was at rest at a sampling frequency of 50 Hz for each of the following experimental conditions: *1*) 4° head-down tilt, control (no medications); *2*) supine, control; *3*) supine, propranolol; *4*) supine, double blockade (propranolol+atropine); and *5*) 4° head-down tilt, double blockade. On the other day, the noninvasive measurements were likewise collected for each of the following experimental conditions: *1*) supine, control; *2*) 30° upright tilt, control; *3*) 30° upright tilt, atropine; *4*) 30° upright tilt, double blockade; and *5*) supine, double blockade. At least 5 min were allowed for hemodynamic equilibration between each experimental condition.

On the basis of these noninvasive recordings, we created a data set for technique evaluation as follows. First, we visually examined each noninvasive finger ABP waveform and instantaneous CO waveform and extracted the longest contiguous, artifact-free segment from each waveform. Then we excluded from the study all instantaneous CO waveforms that were less than 1 min in duration and all finger ABP waveforms that were less than 5 min in duration or had unreasonably high-pressure values (see DISCUSSION). Next, the reference CO value corresponding to each of the remaining instantaneous CO waveforms was determined by computing its time average. Then, because the hemodynamic data collected from the supine, control and supine, double blockade conditions hardly differed from 1 experimental day to the next, these data were combined (as the technique estimates changes in CO) by averaging the reference CO values and the (subsequently determined) corresponding proportional CO estimates over the 2 experimental days. Finally, because the 4° head-down tilt posture did not induce a significant hemodynamic change with respect to the supine posture, these data were discarded from the study. (Note that, if the 4° head-down tilt data were instead combined with the corresponding supine data, the overall results reported below would differ by <1%.) A total of 57 pairs of simultaneous measurements of

artifact-free, noninvasive finger ABP waveforms and reference Doppler ultrasound CO values from 10 healthy subjects remained for technique evaluation. Table 2 summarizes the hemodynamic data for each of the subjects.

Statistical Analysis

After applying the mathematical analysis technique to all of the invasive and noninvasive peripheral ABP waveforms in the two human data sets, we quantitatively compared the resulting, proportional CO estimates with their reference, absolute CO values in each data set as follows. First, we scaled the proportional CO estimates to have the same mean value as the corresponding reference CO within each patient or subject. Then, we pooled the data together from all the patients or subjects in each data set and performed Bland-Altman analysis to comprehensively visualize the CO error (difference between calibrated CO estimate and reference CO value normalized by the reference CO value and given in percent), including its bias (μ) and precision (σ) (4). We also computed the CO root-mean-squared normalized error (RMSNE = $\sqrt{\mu^2 + \sigma^2}$) as a scalar metric indicating

Table 2. *Summary of the healthy young adult records and results of the noninvasive human hemodynamic data set*

Subject Record	Number of Comparisons	CO Range, l/min	MAP Range, mmHg	TPR Range, PRU	HR Range, beats/min	CO RMSNE, %
LD	5	3.6–6.8	82–128	1.0–1.9	43–108	13.0
WP	6	4.3–6.3	68–93	0.7–1.1	60–113	16.9
CG	6	4.5–7.7	75–118	0.9–1.3	48–98	20.2
JE	6	4.5–8.2	85–125	0.9–1.4	51–135	14.6
AE	6	3.5–5.3	79–124	1.2–1.5	32–72	18.3
DL	4	3.5–4.7	92–104	1.2–1.9	60–88	14.8
GB	6	4.6–7.2	65–83	0.6–1.0	56–126	13.3
LB	6	4.3–7.1	70–95	0.8–1.1	47–100	9.0
MR	6	4.4–6.8	75–102	0.8–1.2	50–115	12.1
NB	6	3.7–8.4	72–116	0.8–1.5	48–99	15.3
TOTAL	57	3.5–8.4	65–128	0.6–1.9	32–135	15.1

The technique of Fig. 3 as applied to 57 noninvasive finger arterial blood pressure waveform segments from 10 healthy young adults achieved an overall CO RMSNE of 15.1% with respect to reference Doppler ultrasound measurements made by an expert.
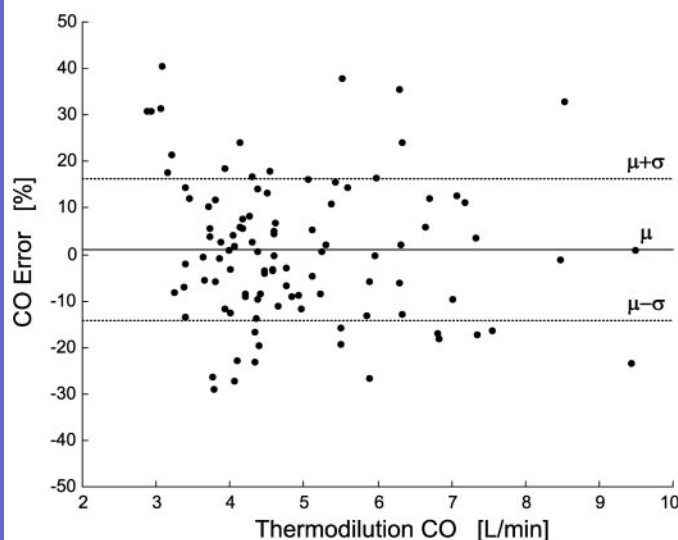
Fig. 5. Bland-Altman plot comprehensively illustrating the results of the invasive hemodynamic data set specifically in terms of the CO error of the technique of Fig. 3 vs. the reference thermodilution CO. The CO error here is defined to be the difference between a calibrated CO estimate and the reference thermodilution CO value normalized by the reference thermodilution CO value and given in percent. The technique as applied to 101 invasive radial arterial blood pressure waveform segments from 15 intensive care unit patients achieved an overall CO error bias of $\mu = 0.60\%$ and precision of $\sigma = 15.28\%$ with respect to the reference thermodilution measurements.

the size of the overall CO error. [Note that, because the bias component will be small (but not exactly zero) here because of the scaling, the CO RMSNEs reported below are mainly due to its precision component.] These metrics indicate the ability of the technique to measure changes in CO relative to its mean value within an individual. We also computed the correlation coefficients (ρ) between the pooled CO error. The corresponding values of CO, MAP, TPR, HR, and CO change with respect to its mean value within each patient or subject (ΔCO), and the magnitude of these CO changes ($|\Delta$CO$|$) in each data set to determine the extent to which the hemodynamic conditions affected the performance of the technique.

RESULTS

Figure 4 illustrates a representative example of a measured (actual) and fitted (predicted) human peripheral ABP waveform by the mathematical analysis technique. Note that the figure includes two predicted ABP waveforms. Each sample of the ABP waveform indicated with the dotted line is predicted from the past samples of the actual $y(t)$ and the input $x(t)$ in Fig. 3 (i.e., one-step ABP prediction), whereas each sample of the ABP waveform indicated with the dashed line is predicted from only the input $x(t)$ (i.e., full ABP prediction) (21). Because one-step ABP prediction is what is optimized by the technique (to obtain a closed-form solution; see *Eq. 1*) and is an easier task than full ABP prediction, the one-step prediction ABP waveform is more accurate and, in fact, virtually superimposable on the actual ABP waveform indicated with the solid line. Nevertheless, the correspondence between the actual and full prediction ABP waveforms is quite good, especially on a beat-to-beat basis. As discussed above, because both predicted ABP waveforms correspond closely to the actual ABP waveform over time scales greater than a cardiac cycle, the subsequent estimation of the windkessel time constant τ and

proportional CO via Ohm's law (see Fig. 3) should, in principle, be accurate.

Figures 5 and 6, respectively, illustrate the overall results of evaluating the technique with respect to the invasive and noninvasive hemodynamic data sets in terms of Bland-Altman plots of the CO error. (Note that the *x*-axis of these plots is reference CO rather than the average of reference CO and calibrated, estimated CO.) Tables 1 and 2, respectively, summarize the CO RMSNE of the technique with respect to each patient in the invasive hemodynamic data set and each subject in the noninvasive hemodynamic data set. Indeed, these tables and figures indicate that the technique as applied to invasive radial ABP waveforms was in strong agreement with thermodilution measurements in 15 ICU patients with an overall CO RMSNE of 15.3%, whereas the technique as applied to noninvasive finger ABP waveforms was in equally strong agreement with Doppler ultrasound measurements made by an expert in 10 healthy subjects with an overall CO RMSNE of 15.1%. Moreover, the CO error resulting from the invasive hemodynamic data set was essentially uncorrelated with CO ($\rho = -0.14$), HR ($\rho = 0.04$), ΔCO ($\rho = -0.26$), and $|\Delta$CO$|$ ($\rho = 0.03$) and only mildly correlated with MAP ($\rho = 0.41$) and TPR ($\rho = 0.38$), whereas the CO error resulting from the noninvasive hemodynamic data set was essentially uncorrelated with CO ($\rho = -0.17$), TPR ($\rho = 0.10$), HR ($\rho = 0.19$), and ΔCO ($\rho = 0.20$) and only mildly correlated with MAP ($\rho = 0.37$) and $|\Delta$CO$|$ ($\rho = 0.38$). Finally, in the noninvasive hemodynamic data set in which the interventions were known (see DISCUSSION), the CO RMSNE for each intervention (atropine, propranolol, and/or a 30° upright shift in posture) ranged from 8.1 to 20.8%, with the higher errors obtained during the double blockade conditions.

Fig. 6. Bland-Altman plot comprehensively illustrating the results of the noninvasive hemodynamic data set specifically in terms of the CO error of the technique of Fig. 3 vs. the reference Doppler ultrasound CO measurements made by an expert. The CO error here is defined to be the difference between a calibrated CO estimate and the reference Doppler ultrasound CO value normalized by the reference Doppler ultrasound CO value and given in percent. The technique as applied to 57 noninvasive finger ABP waveform segments from 10 healthy young adults achieved an overall CO error bias of $\mu = 0.57\%$ and precision of $\sigma = 15.08\%$ with respect to the reference Doppler ultrasound measurements.

DISCUSSION

In summary, we have recently introduced a new technique for continuous [i.e., automatic and without the need for an operator) monitoring of relative changes in CO by long time interval analysis of a peripheral ABP waveform (see Ref. 26 and Figs. 1–4 herein). We have previously demonstrated the validity of the technique with respect to intra-arterial femoral and radial ABP waveforms obtained from open-chest swine instrumented with aortic flow probes over a wide physiological range (26). Here, we present an evaluation of the technique in humans based on previously published invasive and noninvasive hemodynamic data sets (10, 24, 25, 27). Although the evaluation described herein was retrospective, it is noteworthy that neither of these data sets was designed for the evaluation of our technique or any other pulse contour analysis technique. With the former data set, we compared the application of the technique to invasive radial ABP waveforms with reference thermodilution measurements in 15 ICU patients in which CO was changing because of disease progression and therapy. With the latter data set, we compared the application of the technique to noninvasive finger ABP waveforms with reference Doppler ultrasound measurements made by an expert in 10 healthy subjects during pharmacological and postural interventions. We report an overall CO estimation error of about 15% with respect to each of these human data sets (see Tables 1 and 2 and Figs. 5 and 6).

Potential Sources of CO Error

The CO errors reported here could be partly explained by inadequacies in the quality and accuracy of the hemodynamic measurements within the studied invasive and noninvasive data sets. However, as described below, we excluded from the study all data segments of poor quality (e.g., corrupted by significant noise artifact) so as to benchmark technique performance. On the other hand, nothing could be done in this retrospective study to improve on the accuracy of the measurements, which is largely intrinsic to the employed transducers.

The radial ABP waveforms in the invasive data set were measured with generally accurate, intra-arterial catheters. However, in the MIMIC database on which this data set was based, ABP waveform artifact was sometimes present. The artifact may have been due, for example, to patient movement, arterial line flushing, catheter obstruction, loss of signal, and proximal ABP cuff inflation. We excluded from the study all radial ABP waveforms that were significantly corrupted by such artifact (~11% of the available, simultaneous pairs of radial ABP waveforms and thermodilution measurements). Although we identified ABP artifact here by visual means, it may be possible to automatically and reliably detect ABP artifact in real time [e.g., with a simultaneous surface ECG measurement based on an algorithm recently introduced by Zong et al. (39)] so as to warn the clinician that the CO estimate derived from the ABP analysis may not be valid or preclude the output of such a CO estimate. Note that, for reasons described above, we also excluded from the study all radial ABP waveforms with linear trends of ≥20 mmHg (~13% of the available, simultaneous pairs of radial ABP waveforms and thermodilution measurements).

In contrast to the radial ABP waveforms in the invasive data set, it was not possible to assess the quality of the corresponding thermodilution measurements. However, the error in clinical thermodilution measurements is known to be in the 15–20% range (18, 36). Assuming such an error, Critchley and Critchley (8) argued that a new CO measurement method should be accepted as an alternative to thermodilution, provided that their limits of agreements are within ±30%. We note that the level of agreement between our technique and thermodilution measurements from 15 ICU patients is essentially in this range (see Table 1 and Fig. 5).

The noninvasive hemodynamic data utilized in this study were obtained from controlled experiments, and none of the noninvasive finger ABP waveforms were excluded from the study because of noise artifact. However, two noninvasive finger ABP waveforms were excluded from the study because of unreasonably high pressure levels. This artifact may have been due to an upward drift in finger ABP caused by prolonged application of cuff pressure (34). Note that this finger-cuff photoplethysmography artifact may be attenuated or eliminated by intermittent finger exercise (34) or with the currently available Portapres system, which alternates the application of cuff pressure between different fingers.

Although artifact in the noninvasive finger ABP waveforms was not a significant factor here, the intrinsic level of accuracy of the employed Finapres system may have affected our results. In a review of Finapres technology, Imholz et al. (16) gathered 43 previous studies comparing the Finapres system with intra-arterial or noninvasive, discrete ABP measurements and reported that the systolic and mean pressure levels of the Finapres system were not within the limits of accuracy suggested by the American Association for the Advancement of Medical Instruments. On the other hand, Omboni et al. (29) showed that the Finapres system and radial artery catheterization produce similar beat-to-beat (mean) ABP fluctuations. That is, although the Finapres system distorts the peripheral ABP waveform over short time scales, it may have little effect on the waveform over longer time scales. Thus, because the technique analyzes the ABP waveform over long time intervals, the inherent inaccuracies of the Finapres system may not have been a major contributor to the CO error reported herein. However, we cannot confirm this possibility, because simultaneous intra-arterial ABP recordings were not available.

The reference Doppler ultrasound measurements in the noninvasive data set were made by an expert, and only four of these CO measurements were excluded from the study because of poor signal quality. Despite the generally excellent signal quality, the assumptions underlying the Doppler ultrasound technique could have been partially violated, thereby affecting our results. These assumptions include the following: *1)* the velocity profile in the aortic valve orifice is rectangular and this velocity is conserved as the central maximum velocity of a jet 3–4 cm downstream; *2)* the insonication angle is 20°; and *3)* the aortic valve is circular (11). However, *assumptions 2 and 3* are likely to have little effect on the accuracy of the measured relative changes in CO, whereas the same argument has been made for *assumption 1* (37). Because our technique is designed to measure relative changes in CO and we evaluated it here as such (see *Statistical Analysis*), we believe that the Doppler ultrasound measurements serve as a reasonably accurate reference here (i.e., at least as accurate as standard thermodilution measurements).

Other potential sources of the CO errors reported here are any violations to the assumptions on which the technique is based. These assumptions include the following: *1*) AC is constant within each individual; *2*) peripheral venous pressure is negligible with respect to ABP; *3*) ABP exceeds the critical closing pressure; and *4*) the time constant governing arterial viscoelastic effects is negligible with respect to the windkessel time constant (26). The first of these assumptions is perhaps the most controversial, because there is currently no generally accepted, gold-standard method for measuring in vivo AC. Nevertheless, we believe that in vivo AC must be nearly constant over a wide hemodynamic range in at least some animals on the basis of the success of the pulse contour analysis of Bourgeois et al. (5, 6) and Osborn et al. (31) with respect to canine central ABP waveforms and the present mathematical analysis technique with respect to swine peripheral ABP waveforms (26). We are unaware of any existing in vivo data likewise demonstrating constancy of the human AC. However, Hallock and Benson (15) did show that, although the compliance of excised human aortas of various ages at autopsy (ranging from young adults to the elderly) decreased with increasing pressure, in vitro aortic compliance could be approximated as constant over a wide pressure range. If in vivo AC sharply changed in the opposite direction of MAP within each individual record of our study, then our technique would have grossly overestimated CO at high MAP levels and underestimated CO at low MAP levels (i.e., a strong, positive correlation between CO error and MAP). Although the correlation between CO error and MAP is positive, the degree of correlation is mild (see above), suggesting that in vivo AC within each of the 15 ICU patient and 10 healthy young adult records may have been approximately constant.

Comparison to Intrabeat Pulse Contour Analysis Techniques

In a previous paper introducing our mathematical analysis technique (26), we used signal-to-noise theory to argue that estimating the average windkessel time constant τ (and thus average, proportional CO via Ohm's law) by analyzing a peripheral ABP waveform over time intervals greater than a cardiac cycle should be more accurate than analyzing the ABP waveform over individual cardiac cycles and then averaging the beat-to-beat results. To support this theoretical argument, we fitted complex exponentials function(s) to individual diastolic decay intervals of swine peripheral ABP waveforms to estimate τ on a beat-to-beat basis, averaged the resulting individual τ estimates, and then computed average, proportional CO via Ohm's law. The best result we were able to achieve with this intrabeat analysis was an overall CO RMSNE that was 52% larger than that obtained by our technique. We repeated this intrabeat analysis with respect to the human invasive and noninvasive hemodynamic data sets here and obtained overall CO RMSNEs that were, respectively, 23 and 81% higher than those obtained by our technique. (Note that one possible reason that this intrabeat analysis is much less effective with respect to the noninvasive hemodynamic data set is that, as described above, the noninvasive ABP waveforms may suffer from high-frequency distortion due to the employed Finapres system). We believe that these comparative studies confirm the theory that important information is indeed present in beat-to-beat ABP variations and that analysis of these subtle variations leads to improved average, proportional CO estimation in practice. However, we note that future studies should also be conducted to compare our technique with the recent intrabeat techniques of Wesseling et al. (38) and Linton and Linton (20), which also require a single peripheral ABP waveform for analysis.

Limitations of the Long Time Interval Analysis Technique

Two limitations of the current form of the long time interval analysis technique are: *1*) beat-to-beat CO monitoring is not feasible and *2*) artifact is a more significant problem (compared with beat-to-beat pulse contour analysis techniques such as the aforementioned). With respect to the former limitation, we feel that attempts to improve the accuracy of average, proportional CO estimation, even at the cost of temporal resolution, are worthwhile from a clinical point of view. For example, although many previous pulse contour analysis techniques can offer beat-to-beat proportional CO monitoring, they have still not been widely adopted in clinical practice, presumably because of accuracy concerns. Moreover, automatic estimation of proportional CO at intervals on the order of seconds but representing the last 6 min (i.e., boxcar moving average) would represent a significant improvement on discrete, operator-required determinations of CO by the clinical thermodilution method (assuming similar accuracy). With respect to the second limitation, the requirement of ~6-min intervals of relatively artifact-free ABP waveforms does not substantially limit the practical applicability of the technique. For example, only ~11% of the invasive radial ABP waveforms from the real-world MIMIC database were discarded in our study because of artifact. Moreover, the 6-min intervals of analysis may be reduced to smaller intervals (e.g., 1 min) without materially affecting the accuracy of the estimates (e.g., CO RMSNE of 16.1% in the invasive hemodynamic data set and 15.7% in the noninvasive hemodynamic data set). Future formal studies are needed to determine the minimum interval for analysis that does not significantly compromise the accuracy of the technique.

Limitations of the Human Evaluation Study

In the invasive hemodynamic data set, CO was naturally changing within each ICU patient record because of disease progression and therapy. Typical ICU therapy is known to include medications such as dobutamine, dopamine, intravenous fluids, and nitroprusside (i.e., both cardiac and vascular interventions) (22). However, because time-stamped annotations were not available here, we were not able to evaluate the technique in the ICU patients with respect to each of these common therapeutic interventions. In contrast, in the noninvasive hemodynamic data set, CO was changing in each healthy subject because of precisely known interventions of atropine, propranolol, and/or a 30° upright shift in posture. As described above, the CO RMSNEs were largest during the double blockade conditions, presumably because beat-to-beat HR variability was totally abolished. Although vascular changes (TPR and fluid shifts) occurred reflexively on administration of atropine and propranolol as well as via the postural shift (see Table 2), we were not able to test the technique with respect to noninvasive ABP waveforms during interventions that directly act on the vasculature (e.g., phenylephrine, nitroprusside). Finally,

because the reference thermodilution CO in the invasive hemodynamic data set could not be assumed to be valid during unsteady conditions (e.g., ABP waveform segments with significant trends) and the noninvasive ABP waveforms were only recorded during steady conditions (*Invasive Human Hemodynamic Data Set*), we were not able to evaluate the technique in humans during unsteady conditions (i.e., rapid changes in CO). However, we have previously shown that the technique performs quite accurately during unsteady conditions in swine instrumented with aortic flow probes measuring instantaneous flow (26). Moreover, in the present human study, we were at least able to show that the technique performed approximately the same regardless of the size or direction of the CO change, as the correlations between the CO error and ΔCO and |ΔCO| were only mild (*Noninvasive Human Hemodynamic Data Set*).

Potential Applications of the Mathematical Analysis Technique

Our technique mathematically analyzes a single peripheral ABP waveform over long time intervals to continuously (i.e., automatically and without the need for an operator) measure CO to within a constant scale factor. The technique may therefore be utilized to quantitatively monitor relative changes in CO. The proportional CO may be calibrated, if desired, with a single, absolute CO measurement (e.g., thermodilution). For normal individuals, it may be possible to determine the proportionality constant from a nomogram. However, we believe determination of the proportionality constant is unnecessary in the context of continuous monitoring in the acute setting in which only CO changes are clinically relevant.

The results of this retrospective human evaluation study indicate that the technique may be sufficiently accurate in terms of estimating relative changes in CO with respect to invasive radial ABP waveforms from critically ill patients and noninvasive finger ABP waveforms from healthy subjects. With further mathematical analysis development (including the incorporation of an automated artifact detector) and successful prospective testing, the technique may potentially be applied to continuously monitor CO in the acute setting. The most prominent such application is in critically ill patients in the ICU and operating and recovery rooms. In critically ill patients instrumented with both pulmonary and radial artery catheters, the technique could be calibrated with a single thermodilution measurement to permit subsequent continuous monitoring of absolute CO. In the numerous critically ill patients with only radial artery catheters installed (see Introduction), the technique could provide continuous, quantitative monitoring of relative changes in CO. Other such applications in which noninvasive peripheral ABP transducers would be most appropriate include patients in the emergency room and the hospital ward, trauma patients in transport, as well as soldiers in combat. The human evaluation study described herein represents an initial step toward the realization of such applications.

REFERENCES

1. **Akselrod S, Gordon D, Madwed JB, Snidman NC, Shannon DC, and Cohen RJ.** Hemodynamic regulation: investigation by spectral analysis. *Am J Physiol Heart Circ Physiol* 249: H867–H875, 1985.

2. **Appel ML, Berger RD, Saul JP, Smith JM, and Cohen RJ.** Beat to beat variability in cardiovascular variables: noise or music? *J Am Coll Cardiol* 14: 1139–1148, 1989.

3. **Berger RD, Saul JP, and Cohen RJ.** Transfer function analysis of autonomic regulation. I. Canine atrial rate response. *Am J Physiol Heart Circ Physiol* 256: H142–H152, 1989.

4. **Bland JM and Altman DG.** Statistical methods for assessing agreement between two methods of clinical measurement. *Lancet* 1: 307–310, 1986.

5. **Bourgeois MJ, Gilbert BK, Donald DE, and Wood EH.** Characteristics of aortic diastolic pressure decay with application to the continuous monitoring of changes in peripheral resistance. *Circ Res* 35: 56–66, 1974.

6. **Bourgeois MJ, Gilbert BK, von Bernuth G, and Wood EH.** Continuous determination of beat-to-beat stroke volume from aortic pressure pulses in the dog. *Circ Res* 39: 15–24, 1976.

7. **Critchley LAH.** Impedance cardiography. The impact of new technology. *Anaesthesia* 53: 677–684, 1998.

8. **Critchley LAH and Critchley JAJH.** A meta-analysis of studies using bias and precision statistics to compare cardiac output measurement techniques. *J Clin Monit Comput* 15: 85–91, 1999.

9. **Ehlers KC, Mylrea KC, Waterson CK, and Calkins JM.** Cardiac output measurements. A review of current techniques and research. *Ann Biomed Eng* 14: 219–239, 1986.

10. **Elstad M, Toska K, Chon KH, Raeder EA, and Cohen RJ.** Respiratory sinus arrhythmia: opposite effects on systolic and mean arterial pressure in supine humans. *J Physiol* 536: 251–259, 2001.

11. **Eriksen M and Walloe L.** Improved method for cardiac output determination in man using ultrasound Doppler technique. *Med Biol Eng Comput* 28: 555–560, 1990.

12. **Erlanger J and Hooker DR.** An experimental study of blood-pressure and of pulse-pressure in man. *Bull Johns Hopkins Hosp* 12: 145–378, 1904.

13. **Frank O.** Die Grundform des arteriellen Pulses. *Erste Abhandlung Mathematische Analyse Z Biol* 37: 483–526, 1899.

14. **Granger HJ and Guyton AC.** Autoregulation of the total systemic circulation following destruction of the central nervous system in the dog. *Circ Res* 25: 379–388, 1969.

15. **Hallock P and Benson JC.** Studies on the elastic properties of human isolated aorta. *Am J Physiol* 16: 595–602, 1937.

16. **Imholz BPM, Wieling W, van Montfrans GA, and Wesseling KH.** Fifteen years experience with finger arterial pressure monitoring: assessment of the technology. *Cardiovasc Res* 38: 605–616, 1998.

17. **Kenner T.** ABP and its measurement. *Basic Res Cardiol* 83: 107–121, 1988.

18. **Levett JM and Replogle RL.** Thermodilution cardiac output: a critical analysis and review of the literature. *J Surg Res* 27: 392–404, 1979.

19. **Linton DM and Gilon D.** Advances in noninvasive cardiac output monitoring. *Ann Cardiac Anaesth* 5: 141–148, 2002.

20. **Linton NWF and Linton RAF.** Estimation of changes in cardiac output from the ABP waveform in the upper limb. *Br J Anaesth* 86: 486–496, 2001.

21. **Ljung L.** *System Identification: Theory for the User.* Englewood Cliffs, NJ: PTR Prentice-Hall, 1987.

22. **Marino PL.** *The ICU Book.* Baltimore, MD: Williams & Wilkins, 1998.

23. **MIMIC Database.** http://www.physionet.org/physiobank/database/mimicdb/.

24. **Moody GB and Mark RG.** A database to support development and evaluation of intelligent intensive care monitoring. *Comput Cardiol* 23: 657–660, 1996.

25. **Moody GB, Mark RG, and Goldberger AL.** PhysioNet: a web-based resource for study of physiologic signals. *IEEE Eng Med Biol Mag* 20: 70–75, 2001.

26. **Mukkamala R, Reisner AT, Hojman HM, Mark RG, and Cohen RJ.** Continuous cardiac output monitoring by peripheral blood pressure waveform analysis. *IEEE Trans Biomed Eng* 53: 459–467, 2006.

27. **Mukkamala R, Toska K, and Cohen RJ.** Noninvasive identification of the total peripheral resistance baroreflex. *Am J Physiol Heart Circ Physiol* 284: H947–H959, 2003.

28. **Noordergraaf A.** *Circulatory System Dynamics*. New York: Academic, 1978.
29. **Omboni S, Parati G, Fratola A, Mutti E, DiRienzo M, Castiglioni P, and Mancia G.** Spectral and sequence analysis of finger blood pressure variability. Comparison with analysis of intra-arterial recordings. *Hypertension* 22: 26–33, 1993.
30. **O'Rourke MF and Yaginuma T.** Wave reflections and the arterial pulse. *Arch Intern Med* 144: 366–371, 1984.
31. **Osborn JJ, Russell JAG, Beaumont J, deLanerolle P, McChesney B, and Garfield F.** The measurement of relative stroke volume from aortic pulse contour pulse pressure. *Vasc Dis* 5: 165–177, 1968.
32. **Rapoport J, Teres D, Steingrub J, Higgins T, McGee W, and Lemeshow S.** Patient characteristics and ICU organizational factors that influence frequency of pulmonary artery catheterization. *JAMA* 283: 2559–2567, 2000.
33. **Rhodes A and Sunderland R.** Arterial pulse power analysis: the lidco^tm plus system. In: *Functional Hemodynamic Monitoring. Update in Intensive Care and Emergency Medicine*, edited by Pinksy MR and Payen D. Berlin: Springer-Verlag, 2005, 183–192.
34. **Ristuccia HL, Grossman P, Watkins LL, and Lown B.** Incremental bias in Finapres estimation of baseline blood pressure levels over time. *Hypertension* 29: 1039–1043, 1997.
35. **Shah MR, Hasselblad V, Stevenson LW, Binanay C, O'Connor CM, Sopko G, and Califf RM.** Impact of the pulmonary artery catheter in critically ill patients: meta-analysis of randomized clinical trials. *JAMA* 294: 1664–1670, 2005.
36. **Stetz CW, Miller RG, Kelly GE, and Raffin TA.** Reliability of the thermodilution method in the determination of cardiac output in clinical practice. *Am Rev Respir Dis* 126: 1001–1004, 2982.
37. **Toska K.** *Short-term Cardiovascular Control in Humans* (PhD Thesis). Oslo: University of Oslo, 1995.
38. **Wesseling KH, Jansen JRC, Settels JJ, and Schreuder JJ.** Computation of aortic flow from pressure in humans using a nonlinear, three-element model. *Am J Physiol* 74: 2566–2573, 1993.
39. **Zong W, Moody GB, and Mark RG.** Reduction of false arterial blood pressure alarms using signal quality assessment and relationships between the electrocardiogram and arterial blood pressure. *Med Biol Eng Comput* 42: 698–706, 2004.

Journal of Applied Physiology

Cardiac Output Monitoring by Long Time Interval Analysis of a Radial Arterial Blood Pressure Waveform with Correction for Arterial Compliance Changes using Pulse Transit Time

Mohsen Moslehpour, Guanqun Zhang, and Ramakrishna Mukkamala, *Member, IEEE*

Abstract—We previously developed a technique for estimating relative cardiac output (CO) change by long time interval analysis of a radial arterial blood pressure waveform. This technique analyzes the slow, beat-to-beat changes in the waveform to circumvent the confounding wave reflections but assumes constant arterial compliance (AC). Here, we sought to correct the CO estimates of the technique for potential AC changes using pulse transit time – a conveniently measured index of AC. For proof-of-concept, we compared the original and corrected techniques using invasive swine hemodynamic data. The corrected technique reduced the overall calibrated CO estimation error by 18% relative to the original technique.

I. Introduction

A potential approach for achieving continuous and minimally invasive cardiac output (CO) monitoring in surgery and intensive care patients is by mathematical analysis of an arterial blood pressure (ABP) waveform obtained with a radial artery catheter that is already in place. A number of such "pulse contour analysis" techniques have, in fact, been proposed [1]. Generally speaking, while these techniques have been shown to work reasonably well during relatively steady conditions, they have been shown to be inaccurate during the crucial periods of hemodynamic instability (i.e., widely varying CO and/or ABP) [2].

We now believe that two challenges must be overcome for pulse contour analysis to be able to provide accurate estimates of relative CO change during instability. First and foremost, arterial wave reflections, which shape the radial ABP waveform, must be taken into account. Yet, most pulse contour analysis techniques (e.g., pulse pressure (PP) times heart rate (HR)) actually ignore the confounding wave reflections [1]. Secondly, changes in total arterial compliance (AC), which can also alter the radial ABP waveform morphology, must be compensated for in the analysis. While many pulse contour analysis techniques

M. Moslehpour is with the Department of Electrical and Computer Engineering, Michigan State University, East Lansing, MI 48824 USA (e-mail: moslehpo@msu.edu).

G. Zhang. is with the Department of Electrical and Computer Engineering, Michigan State University, East Lansing, MI 48824 USA (e-mail: zhanggu2@msu.edu).

R. Mukkamala is with the Department of Electrical and Computer Engineering, Michigan State University, East Lansing, MI 48824 USA (phone: 517-353-3120; fax: 517-353-1980; e-mail: rama@egr.msu.edu).

have sought to do so, current ones employ empirical curves relating in vitro AC to ABP [3, 4] and consequently can be prone to error due to any vasomotor tone induced AC changes in addition to inter-subject variability.

We previously developed a technique for estimating relative CO change by long time interval analysis of a radial (or other peripheral) ABP waveform [1]. The idea of the technique is to circumvent the confounding wave reflections by analyzing the slow, beat-to-beat variations in the waveform wherein such phenomena are minimal. Up to now, the main assumption of the technique has been that AC is constant. While we have shown that this assumption can be reasonable in several conditions [1, 5, 6], its validity becomes less tenable with increasing changes in ABP and possibly other conditions of interest.

In this study, we sought to correct the CO estimates of our long time interval analysis technique for potential AC changes using pulse transit time (PTT) – a conveniently measured index of AC. To demonstrate proof-of-concept, we compared the corrected and original techniques based on invasive hemodynamic data from swine.

II. Methods

A. Original and Corrected Techniques

The original long time interval analysis technique is shown in Fig. 1. First, a cardiac contractions signal (x(t)) is constructed from the radial ABP waveform (y(t)) by forming an impulse train in which the impulses are located at the waveform feet and are scaled by the ensuing PPs. Then, a parameterized impulse response (h(t)) is identified, which when convolved with x(t), best fits y(t) in the least squares sense. Next, the Windkessel time constant (τ), which is equal to total peripheral resistance (TPR) times AC, is determined by fitting an exponential to the tail end of h(t) once the faster wave reflections have vanished. (In theory, reliable determination of τ is attained by accurate coupling of the beat-to-beat variations in x(t) to y(t).). Finally, proportional CO is computed by dividing mean ABP (MAP) with τ. Thus, the 1/AC scale factor is assumed to be constant for each subject. (See [1] for full details.)

To correct this technique for possible AC changes, simultaneous measurements of PTT are utilized. According to the well-known Bramwell-Hill equation, PTT is related to AC as follows:

$$PTT = \sqrt{\frac{\rho l}{A} AC},$$

where ρ is the density of blood, l is the arterial length, and A is the arterial cross-sectional area. Note that since the aorta is the main contributor to AC, PTT here is specifically obtained through the aorta. Thus, the original technique may be corrected for any AC change precisely as follows:

$$CO \propto PTT^2 \frac{MAP}{\tau}.$$

Note that the scale factor now becomes ρl/A. Of these three parameters, only A is expected to be able to change in a subject. However, A has been shown to change much less than AC [7]. Thus, the corrected technique may provide an improved estimate of proportional CO in a subject, particularly during hemodynamic instability.
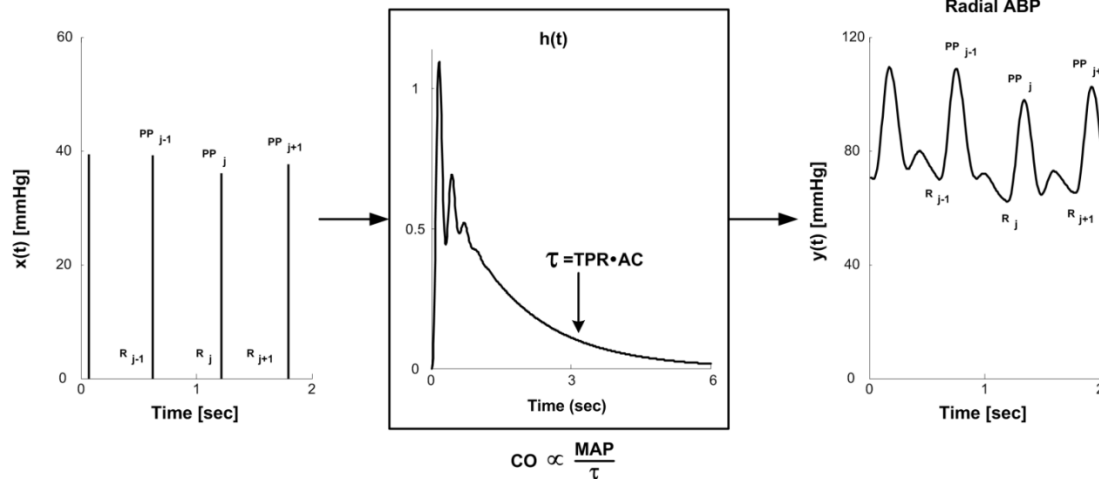

Fig. 1. Original long time interval analysis technique for estimating relative cardiac output (CO) change from a radial arterial blood pressure (ABP) waveform.

B. Technique Evaluation

Both techniques were evaluated using previously collected hemodynamic data [1]. These data included invasive radial and femoral ABP waveforms and aortic flow probe CO from five swine during various drug and volume interventions. MAP/τ was estimated from six-minute segments of the radial ABP waveforms. PTT was measured from the corresponding segments of the aortic flow and femoral ABP waveforms as the average foot-to-foot time delay between these waveforms. The proportional CO estimates of each technique were then scaled to have the same mean value as the aortic flow probe CO for each animal. The root-mean-square of the relative errors between the calibrated CO estimates of each technique and the reference measurements was then computed over all the animals.

III. RESULTS

Fig. 2 shows the results from one animal in which the calibrated CO estimates of each technique are plotted against the reference CO measurements. The corrected technique noticeably reduced the overall scatter about the identity line in the plots. The root-mean-squared-errors over all the animals were 15.7% for the original technique and 12.9% for the corrected technique.

IV. DISCUSSION

In summary, we employed PTT measurements in an attempt to correct the relative CO change estimates of our long time interval radial ABP waveform analysis technique for any AC change. We tested this corrected technique using previously collected data from swine during various drug and volume interventions. Our results showed that the technique was able to reduce the calibrated CO estimation error by 18% relative to the uncorrected technique.

Our available data included only invasive PTT measurements. Thus, the results here demonstrate proof-of-concept. In practice, PTT could be measured non-invasively using, for example, arterial tonometry or pulse oximetry. Further, the average standard deviation of MAP over all the animals was ~15 mmHg. We suspect that the corrected technique will afford greater improvements in CO estimation accuracy during more severe changes to MAP and other modes of hemodynamic instability. Future testing to address both of these issues would be worthwhile.
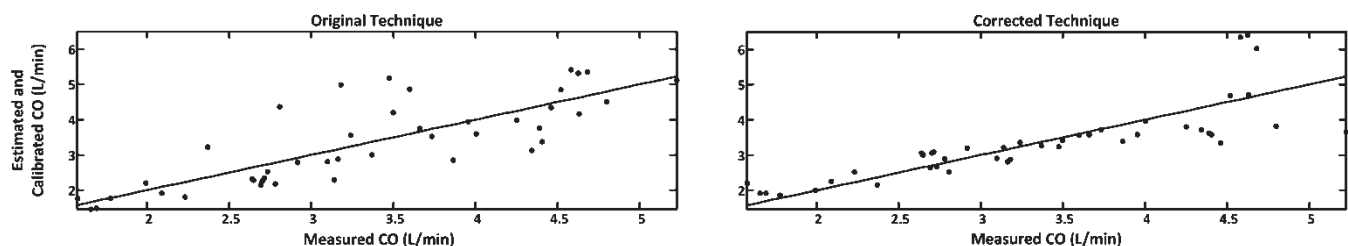

Fig. 2. Results from one animal.

REFERENCES

[1] R. Mukkamala, A.T. Reisner, H.M. Hojman, R.G. Mark, R.J. Cohen, "Continuous cardiac output monitoring by peripheral blood pressure waveform analysis," *IEEE Trans. Biomed. Eng.*, vol. 53, no 3, pp. 459-467, March 2006.

[2] C.H. Lee, J.Y. Wang, K.L. Huang, H.W. Chiu, T.C. Fei, T.S. Chen, H. Chang, "Unreliability of pulse contour-derived cardiac output in piglets simulating acute hemorrhagic shock and rapid volume expansion," *J. Traum.*, vol. 68, no 6, pp. 1357-1361, Jun. 2010.

[3] A. Rhodes, R. Sunderland, "Arterial Pulse Power Analysis: The LiDCOm plus System," *Upd. Int. Car.*, vol. 42, pp. 183-192, 2005.

[4] K.H. Wesseling, J.R. Jansen, J.J. Settels, J.J. Schreuder, "Computation of aortic flow from pressure in humans using a nonlinear, three-element model," *J. Appl. Physiol.*, vol. 74, no 5, pp. 2566-2573, May 1993.

[5] Z. Lu, R. Mukkamala, "Continuous cardiac output and left atrial pressure monitoring by pulmonary artery pressure waveform analysis," *Conf. Proc. IEEE Eng. Med. Biol. Soc.*, pp. 214-217, 2006.

[6] A.T. Reisner, D. Xu, K.L. Ryan, V.A. Convertino, C.A. Rickards, R. Mukkamala, "Monitoring non-invasive cardiac output and stroke volume during experimental human hypovolaemia and resuscitation," *Brit. J. Anaesth.*, vol. 106, pp. 23-30, Jan. 2011.

[7] G.J. Langewouters, K.H. Wesseling, W.J.A. Goedhard, "The static elastic properties of 45 human thoracic and 20 abdominal aortas *in vitro* and the parameters of a new model," *J. Biomech.*, vol. 17, pp. 425-435, 1984.

Continuous Left Ventricular Ejection Fraction Monitoring by Aortic Pressure Waveform Analysis

Gokul Swamy,[1] Jacob Kuiper,[1] Madhu S. R. Gudur,[1] N. Bari Olivier,[2]
and Ramakrishna Mukkamala[1]

[1]Department of Electrical and Computer Engineering, Michigan State University, 2120 Engineering Building, East Lansing, MI 48824, USA; and [2]Department of Small Animal Clinical Sciences, Michigan State University, East Lansing, MI 48824, USA

Abstract—We developed a technique to monitor left ventricular ejection fraction (EF) by model-based analysis of the aortic pressure waveform. First, the aortic pressure waveform is represented with a lumped parameter circulatory model. Then, the model is fitted to each beat of the waveform to estimate its lumped parameters to within a constant scale factor equal to the arterial compliance (C_a). Finally, the proportional parameter estimates are utilized to compute beat-to-beat absolute EF by cancelation of the C_a scale factor. In this way, in contrast to conventional imaging, EF may be continuously monitored without any ventricular geometry assumptions. Moreover, with the proportional parameter estimates, relative changes in beat-to-beat left ventricular end-diastolic volume (EDV), cardiac output (CO), and maximum left ventricular elastance (E_{max}) may also be monitored. To evaluate the technique, we measured aortic pressure waveforms, reference EF and EDV via standard echocardiography, and other cardiovascular variables from six dogs during various pharmacological influences and total intravascular volume changes. Our results showed overall EF and calibrated EDV root-mean-squared-errors of 5.6% and 4.1 mL, and reliable estimation of relative E_{max} and beat-to-beat CO changes. These results demonstrate, perhaps for the first time, the feasibility of estimating EF from only a blood pressure waveform.

Keywords—Arteries, Blood pressure, Cardiac output, End-diastolic volume, Hemodynamics, Left ventricle, Parameter estimation, Pulse contour analysis, Variable elastance model, Windkessel model.

NOMENCLATURE

Mathematical Symbols

C_a	arterial compliance (mL/mmHg)
$E_{lv}(t)$	time-varying ventricular elastance function (mmHg/mL)
E_{max}	maximum left ventricular elastance (mmHg/mL)
E_{min}	minimum left ventricular elastance (mmHg/mL)
n	discrete time or sample index (unitless)
n_{bs}	sample index denoting beginning of the systolic ejection interval (unitless)
n_{es}	sample index denoting end of the systolic ejection interval (unitless)
$P_a(t)$	aortic pressure waveform (mmHg)
R_a	total peripheral resistance (mmHg-s/mL)
T	sampling period (s)
T_s	time duration to reach E_{max} from E_{min} (s)
τ	windkessel time constant ($= R_a C_a$) (s)
t	time (s)
t_{bi}	time of beginning of the isovolumic contraction phase (s)
t_{bs}	time of beginning of the systolic ejection interval (s)
t_{es}	time of end of the systolic ejection interval (s)
$V_{lv}(t)$	left ventricular (total) volume waveform (mL)
V_{lv}^0	left ventricular unstressed volume (mL)

Acronyms

CO	cardiac output (L/min)
ECG	electrocardiogram (mV)
EDV	left ventricular end-diastolic volume (mL)
EF	left ventricular ejection fraction (%)
ESV	left ventricular end-systolic volume (mL)
HR	heart rate (bpm)
MAP	mean aortic pressure (mmHg)
RMSE	root-mean-squared-error (mL for EDV and % for EF)
RMSNE	root-mean-squared-normalized-error (%)
SV	left ventricular stroke volume (mL)

Address correspondence to Ramakrishna Mukkamala, Department of Electrical and Computer Engineering, Michigan State University, 2120 Engineering Building, East Lansing, MI 48824, USA. Electronic mail: rama@egr.msu.edu

INTRODUCTION

Left ventricular ejection fraction (EF)—the ratio of the stroke volume (SV) to the end-diastolic volume (EDV) of the left ventricle—is widely recognized as one of the most clinically significant indices of cardiac function. This recognition is largely due to its ability to predict mortality in patients with heart failure and coronary artery disease[5,12] as well as to readily distinguish between systolic and diastolic dysfunction.[19] Serial changes in EF at rest and transient rate of changes in EF during exercise may offer additional prognostic value.[10,34]

The standard clinical method for measuring EF is through imaging the left ventricular volume via echocardiography, radionuclide techniques, contrast angiography, ultra-fast computed tomography, or magnetic resonance imaging.[28] Each of these imaging methods offers certain advantages over the others in terms of, for example, level of accuracy, invasiveness, and radiation exposure. However, they generally share the major disadvantages of requiring a trained operator to make each individual measurement and expensive capital equipment. While sonomicrometry, the conductance catheter, and the nonimaging nuclear monitor are currently available for automated and continuous monitoring of left ventricular volume,[8,13,29] these alternative methods suffer from significant practical disadvantages (e.g., high level of invasiveness) that have prevented them from supplanting or even complementing imaging methods in clinical practice.

Thus, there is a need for a practical method capable of automated and continuous EF monitoring. Indeed, this need may be regarded as urgent due to the rapidly growing population with chronic heart disease[2] together with the projected shortage of clinical staff.[40]

Based on our previous work in the field of hemodynamic monitoring,[21,25,37,38,42] our hypothesis is that EF may be accurately estimated by deciphering the information embedded in the temporal variations of blood pressure waveforms. In this way, EF may be continuously monitored in various inpatient settings with routinely employed invasive catheter systems[22] as well as automatically measured in outpatient clinics and at home with commercial noninvasive transducers (see, e.g., the Finometer and Portapres, Finapres Medical Systems, The Netherlands and the T-Line Blood Pressure Monitoring System, Tensys Medical, San Diego, CA). As an initial step toward this ultimate end point, our specific aim here was to establish a technique for continuously estimating EF from the aortic pressure waveform. To achieve this aim, we developed a model-based analysis technique that is able to monitor beat-to-beat EF along with relative changes in beat-to-beat EDV and other important

hemodynamic variables as well as performed experiments on dogs to evaluate the technique with respect to standard echocardiography during various pharmacological influences and total intravascular volume changes. Preliminary versions of this work have been reported.[24,39]

MATERIALS AND METHODS

Model-Based Analysis Technique

The model-based analysis technique is generally implemented in three steps. First, the aortic pressure waveform is represented with a circulatory model. Second, the model is fitted to each beat of the waveform so as to estimate its parameters to within a constant scale factor. Third, the proportional parameter estimates are utilized to compute beat-to-beat absolute EF by cancelation of the scale factor as well as monitor other beat-to-beat proportional hemodynamic variables. The details of these steps followed by a summary of the major underlying assumptions are presented below.

First, the measured and sampled aortic pressure waveform is assumed to be well represented with the lumped parameter model of the left ventricle (lv), aortic valve, and arteries (a) shown in Fig. 1a in electrical analog form. Here, voltage is analogous to pressure (P), charge, to volume (V), and current, to flow rate. In particular, the left ventricle is represented with the variable capacitance or compliance (C) model whose elastance ($E = 1/C$) oscillates over time (t) so as to drive the flow of blood.[30,35] The aortic valve is modeled by an ideal diode (i.e., $P_{lv}(t) = P_a(t)$ during the systolic ejection interval wherein the valve is opened) thereby making aortic stenosis a contraindication of the technique (see the Limitation: Aortic Valve Disease subsection in the Discussion section). The arteries are represented with a two-parameter Windkessel model accounting for the compliance of the large arteries and the resistance (R) of the small arteries.[36] In addition to compliance, the left ventricle (and large arteries) is parameterized with a zero-pressure (0) filling volume (i.e., unstressed volume). Finally, C_a is assumed to be constant over a monitoring period (e.g., days to weeks), whereas the remaining parameters are assumed to be constant only over each cardiac cycle.

Thus, the pressure–volume relationship of the left ventricle model and the differential equation governing the entire model during the systolic ejection interval are given as follows:

$$V_{lv}(t) = \frac{P_a(t)}{E_{lv}(t)} + V_{lv}^0, \quad t_{bs} < t \leq t_{es}, \quad (1)$$
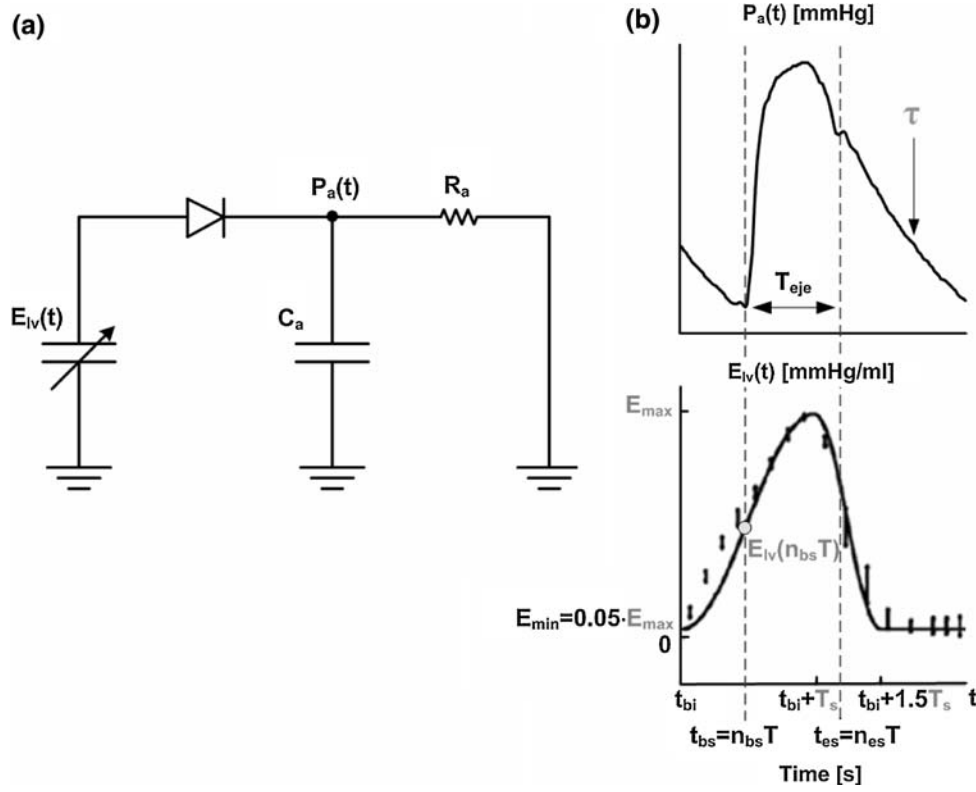
FIGURE 1. (a) Lumped parameter model of the left ventricle and arteries. (b) $E_{lv}(t)$ in the model is assumed to vary over time according to a parametric raised cosine function (solid line in lower panel). This function is well justified, as it provides a good fit to normalized experimental variable elastance data (discrete values in lower panel). (Lower panel adapted from Heldt et al.[16]) The four parameters in gray (upper and lower panels) are to be estimated from the aortic pressure waveform, with E_{max} and $E_{lv}(n_{bs}T)$ specifically determined to within a constant C_a scale factor. See nomenclature for their definitions.

$$-\frac{d}{dt}\frac{P_a(t)}{E_{lv}(t)} = C_a\frac{d}{dt}P_a(t) + \frac{P_a(t)}{R_a}, \quad t_{bs} < t \le t_{es}, \quad (2)$$

where the term $P_a(t)/E_{lv}(t)$ is the stressed left ventricular volume during the systolic ejection interval, and the subscripts bs and es, respectively, stand for the beginning and end of the systolic ejection interval. Integrating Eq. (2) from t_{bs} to some time t within the systolic ejection interval, while dividing by the constant scale factor C_a, yields the following equation:

$$\frac{P_a(t_{bs})}{C_a E_{lv}(t_{bs})} - \frac{P_a(t)}{C_a E_{lv}(t)}$$
$$= P_a(t) - P_a(t_{bs}) + \frac{1}{\tau}\int_{t_{bs}}^{t} P_a(\lambda)d\lambda, \quad t_{bs} < t \le t_{es}, \quad (3)$$

where $\tau = R_a C_a$ is the Windkessel time constant. Note that the left-hand side of this equation is proportional to the volume of blood that has been ejected by the left ventricle by time t in the systolic ejection interval, while the right-hand side is proportional to the volume of blood that has entered the arteries by this time. Thus, when $t = t_{es}$, both sides of the equation indicate proportional SV or SV/C_a. Further note that the term

$P_a(t)/C_a E_{lv}(t)$ here is proportional to the stressed volume that is remaining in the left ventricle at time t in the systolic ejection interval. Thus, the terms $P_a(t_{bs})/C_a E_{lv}(t_{bs})$ and $P_a(t_{es})/C_a E_{lv}(t_{es})$, respectively, represent proportional stressed left ventricular volume at the beginning time of the systolic ejection interval wherein ejection has yet to commence (i.e., proportional stressed EDV or stressed EDV/C_a) and at the end time of the systolic ejection interval wherein ejection has ceased (i.e., proportional stressed left ventricular end-systolic volume (ESV) or stressed ESV/C_a).

Second, to fit the model to the samples of the aortic pressure waveform so as to estimate its parameters, Eq. (3) is discretized by replacing t with nT, where T is the sampling period and n denotes discrete time, and approximating the integral via the trapezoidal formula as follows:

$$\frac{P_a(n_{bs}T)}{C_a E_{lv}(n_{bs}T)} - \frac{P_a(nT)}{C_a E_{lv}(nT)} = P_a(nT) - P_a(n_{bs}T)$$
$$+ \frac{T}{2\tau}\sum_{k=n_{bs}+1}^{n}(P_a(kT) + P_a((k-1)T)), \quad n_{bs} < n \le n_{es}.$$
$$(4)$$

Here, T and $P_a(nT)$ for $n_{bs} \leq n \leq n_{es}$ (i.e., aortic pressure samples within the systolic ejection interval) are known, while τ (i.e., proportional total peripheral resistance) and $C_a E_{lv}(nT)$ for $n_{bs} \leq n \leq n_{es}$ (i.e., proportional left ventricular elastance samples within the systolic ejection interval) are unknown. It is evident that Eq. (4) does not provide a basis for uniquely determining these unknown proportional model parameters and thus the proportional stressed left ventricular volume terms, as it represents an underdetermined set of equations with $n_{es} - n_{bs}$ equations and $n_{es} - n_{bs} + 2$ unknowns (where $n_{es} - n_{bs} \approx 80$ for $T = 4$ ms).

To arrive at a solvable (i.e., overdetermined) set of equations, a parametric function is assumed to succinctly characterize the temporal evolution of $E_{lv}(t)$ over each cardiac cycle. In particular, the following, previously proposed parametric raised cosine function[16] is employed:

$$E_{lv}(t) = \begin{cases} E_{min} + \frac{E_{max} - E_{min}}{2}\left\{1 - \cos\left(\frac{\pi(t - t_{bi})}{T_s}\right)\right\}, & t_{bi} \leq t < t_{bi} + T_s \\ E_{min} + \frac{E_{max} - E_{min}}{2}\left\{1 + \cos\left(\frac{2\pi t(t - (t_{bi} + T_s))}{T_s}\right)\right\}, & t_{bi} + T_s \leq t < t_{bi} + 1.5T_s \\ E_{min}, & t_{bi} + 1.5T_s \leq t \end{cases} \quad (5)$$

where E_{min} and E_{max}, respectively, represent the minimum and maximum ventricular elastances over a cardiac cycle; T_s indicates the time duration to reach E_{max} from E_{min}; and the subscript bi stands for the beginning of the isovolumic contraction phase (see solid line in lower panel of Fig. 1b). Substitution of Eq. (5) into Eq. (4) reduces the number of unknowns to five, namely τ, $C_a E_{max}$, $C_a E_{min}$, T_s, and $C_a E_{lv}(n_{bs}T)$ (i.e., proportional left ventricular elastance at the beginning time of the systolic ejection interval). Further, $C_a E_{min}$ is assumed to be equal to $0.05 \cdot C_a E_{max}$ so as to reduce the number of unknowns to four (see gray font in Fig. 1b for a plot of this function). The four unknowns are then estimated for each beat in two steps.

In the initial step, τ is estimated from the diastolic interval of the aortic pressure waveform. (The diastolic interval is specifically defined as the time period between the dicrotic notch in the waveform (see Fig. 1b) denoting aortic valve closure (i.e., $n_{es}T$ of the beat) and the ensuing minimum pressure (i.e., $n_{bs}T$ of the next beat). The time of the dicrotic notch is automatically identified as the time of the minimum of the first difference of the waveform over the time period from the preceding peak systolic pressure to the minimum pressure.) In particular, since the lumped

parameter model predicts that aortic pressure should decay like a pure exponential during the diastolic interval, τ is estimated by least squares fitting of an exponential to this interval (see Fig. 1b). Optimal fitting is achieved in closed-form after log transformation of aortic pressure. Since the time constants governing R_a changes are significantly longer than the cardiac cycle duration,[3] the τ estimates are then averaged over 10 successive cardiac cycles to attenuate any noise.

In the subsequent step, the estimated τ is substituted into Eq. (4), and the remaining unknowns in this equation, $C_a E_{max}, T_s$, and $C_a E_{lv}(n_{bs}T)$, are estimated by least squares fitting of the equation to the systolic ejection interval of the aortic pressure waveform (i.e., the remainder of the beat). Optimal fitting is achieved by numerical search over the following physiologic range of the three unknowns: (1) 0 (physical minimum value) $< C_a E_{max} \leq 15$ (3 times the nominal value reported in the literature[6,7,18,35]; (2) $1/3QT \leq T_s \leq 4/3QT$, where the QT interval is obtained from a simultaneous electrocardiogram (ECG) measurement (with the underlying assumption that the electrical QT interval is a rough approximation of the mechanical time interval between the start of the upstroke to the end of the downstroke of $E_{lv}(t)$); and (3) $C_a E_{lv}(t_{bi} + T_s - T_{eje}) \leq C_a E_{lv}(n_{bs}T) \leq C_a E_{lv}(t_{bi} + T_s)$, where T_{eje} is the duration of the systolic ejection interval (to ensure that the end time of the systolic ejection interval does not occur prior to the time of E_{max}). With the estimated $C_a E_{max}, T_s$, and $C_a E_{lv}(n_{bs}T)$, $C_a E_{lv}(nT)$ is computed for $n_{bs} < n \leq n_{es}$ through Eq. (5).

Third, beat-to-beat absolute EF is computed from the resulting $C_a E_{lv}(nT)$ for $n_{bs} \leq n \leq n_{es}$ and the measured $P(t)$ by cancelation of the C_a scale factor as follows:

$$EF = \frac{\frac{SV}{C_a}}{\frac{EDV}{C_a}} = \frac{\frac{P_a(n_{bs}T)}{C_a E_{lv}(n_{bs}T)} - \frac{P_a(n_{es}T)}{C_a E_{lv}(n_{es}T)}}{\frac{P_a(n_{bs}T)}{C_a E_{lv}(n_{bs}T)} + \frac{V_{lv}^0}{C_a}}, \quad (6)$$

where V_{lv}^0/C_a (i.e., proportional unstressed left ventricular volume), in contrast to the other terms in the right-hand side of this equation, is neither estimated nor measured but rather assumed to take on a nominal value (see the Data Analysis section). Note that the term $P_a(n_{es}T)/C_a E_{lv}(n_{es}T)$ (i.e., proportional stressed

ESV) should correspond to the minimum value of $P_a(nT)/C_a E_{lv}(nT)$ over $n_{bs} < n \leq n_{es}$ (i.e., proportional stressed left ventricular volume samples within the systolic ejection interval). However, such correspondence may not always hold due to imperfect identification of the end time of the systolic ejection interval (or, equivalently, the beginning time of the diastolic interval). In these instances, $P_a(n_{es}T)/C_a E_{lv}(n_{es}T)$ in Eq. (6) is replaced with the minimum value of $P_a(nT)/C_a E_{lv}(nT)$ over $n_{bs} < n \leq n_{es}$.

Note that by-products of the above three steps are beat-to-beat proportional estimates of EDV, SV, cardiac output (CO = HR·SV, where HR is heart rate), R_a, and E_{max} (which is known to be a relatively specific index of ventricular contractility.[30,35] Thus, relative changes in these important hemodynamic variables may be monitored as well.

As indicated above, the model-based analysis technique arises from several assumptions. To summarize, the major underlying assumptions are as follows:

Assumption 1: lumped parameter model representation of the aortic pressure waveform

Assumption 2: constant arterial compliance

Assumption 3: three parameter raised cosine function representation of left ventricular elastance during the systolic ejection interval

Assumption 4: nominal value for proportional unstressed left ventricular volume

Justification for each of these assumptions is provided in the Discussion section.

Software to execute the model-based analysis technique in the MATLAB programming language along with exemplary data to reproduce Fig. 6 herein are presently available at the following website: http://www.egr.msu.edu/pspml/Journal.html.

Experimental Procedures

To evaluate the model-based analysis technique, experiments were performed in six normal adult dogs (beagle, 10–15 kg). All experimental procedures were reviewed and approved by the MSU All-University Committee on Animal Use and Care.

In one dog, a sterile surgical procedure was employed for implanting chronic recording transducers as follows. General anesthesia was induced with an intravenous injection of propofol (2.2–6.6 mg/kg) and maintained with inhaled isoflorane (1.5–2.5%), and mechanical ventilation was instituted. A left lateral thoracotomy was performed. An ultrasonic flow probe was placed around the ascending aorta for gold standard reference SV and CO (Transonic Systems, Ithaca, NY),

while a tygon catheter was placed in the left atrial appendage for unrelated purposes. The chest was evacuated and closed in layers, with the cable and catheter tunneled subcutaneously and exteriorized between the scapulae. The dog was then allowed 10 days for recovery.

The chronically instrumented dog and the remaining five dogs were then studied as follows. General anesthesia was induced and maintained as described above but mechanical ventilation was not employed. A micromanometer-tipped catheter was inserted into a femoral artery and positioned under fluoroscopic guidance in the descending thoracic aorta (see the Assumptions of the Model-Based Analysis Technique subsection within the Discussion section) for the aortic pressure waveform (Millar Instruments, Houston, TX). A similar catheter was also placed in the opposite femoral artery of half the dogs for future studies. A catheter was inserted into a cephalic vein for drug and isotonic fluid administration, and surface electrodes were placed for two frontal ECG leads. All of the analog transducer outputs were interfaced to a personal computer through an A/D conversion system (DataQ Instruments, Akron, OH). The cardiovascular measurements were then recorded in each dog at a sampling rate of 400–1000 Hz over the course of 50–170 min during a baseline period and a subset of the following pharmacological influences and total intravascular volume changes to alter EF and other hemodynamic variables: infusions of dobutamine (5–20 μg/kg/min), esmolol (50–200 μg/kg/min), verapamil (1–64 μg/kg/min), phenylephrine (2–8 μg/kg/min), nitroprusside (1–4 μg/kg/min), and saline (300 mL) as well as progressive hemorrhage (40–120 mL). Each pharmacological influence was followed by a recovery period in which aortic pressure returned to approximately its baseline level. During the recording session, trans-thoracic two-dimensional echocardiography (GE Vivid 7, Horton, Norway) was intermittently used for four-chamber left apical imaging to calculate reference EF and EDV. (This single-plane method was shown to be nearly equivalent to a biplane method in terms of measuring absolute EF and relative changes in EDV and ESV.[36]) A 5- to 10-beat cine echocardiographic recording at >90 frames/s was obtained at a time for the chronically instrumented dog, whereas 5- to 10-beat cine echocardiographic recordings at the same frame rate were obtained in triplicate for the five acutely studied dogs.

Data Analysis

The model-based analysis technique was applied off-line to the aortic pressure waveforms resampled to 250 Hz with the QT interval automatically detected

from the surface ECGs using a previously introduced wavelet-based method[23] and V_{lv}^0/C_a set to the nominal canine value of 15 mmHg as prescribed elsewhere.[6,7,35] The resulting beat-to-beat EF and proportional EDV and E_{max} estimates were then averaged over multiple beats for evaluation against the reference measurements and known drug effects as follows.

Reference EDV and ESV, and thus EF, were established by manually tracing the endocardial border of the single-plane images, excluding papillary muscles, at end-diastole and end-systole and then applying Simpson's rule.[31] This method was performed for two beats of each cine echocardiographic recording, and the resulting values were then averaged over the two beats. For the five acutely studied dogs, the values were further averaged over each set of triplicate cine echocardiographic recordings. Thus, in these dogs, the reference EF and EDV represent six beat averages. For the chronically instrumented dog, the reference echocardiographic values were validated in part by noting a tight correspondence between the echocardiographic SV and the gold standard aortic flow probe SV ($\rho = 0.92$).

To compare the average proportional EDV estimates with the corresponding absolute reference values, the estimates were first scaled to have the same mean as the reference values in each dog. (Note that this calibration step provided a C_a estimate for each dog.) The average EF and average calibrated EDV estimates were then evaluated against their corresponding reference values through (1) standard Bland–Altman analysis for a comprehensive illustration of the estimation errors as a function of the reference values (rather than the average of the estimated and reference values) and an indication of the bias μ and precision σ of the estimation errors[4] and (2) the root-mean-square of the estimation errors ($RMSE = \sqrt{\mu^2 + \sigma^2}$) for a simple scalar metric indicating the overall error size. In addition, the average changes in the EF and calibrated EDV estimates that occurred relative to the baseline period during each of the pharmacological influences and total intravascular volume changes were qualitatively compared to the corresponding reference changes. Similarly, the average proportional E_{max} estimates were qualitatively evaluated in terms of whether they changed in the physiologically expected manner in response to the positive inotrope dobutamine and the negative inotrope esmolol. (Note that verapamil acted more like a vasodilator in our study.) Finally, for the chronically instrumented dog, the resulting beat-to-beat proportional CO estimates were similarly calibrated and then compared to the corresponding absolute reference aortic flow probe values through the RMSNE (i.e., RMS of the estimation errors normalized (N) by the reference values), as CO errors are customarily reported in percent.[11]

RESULTS

Figure 2 illustrates exemplary segments of the aortic pressure waveform measured from one of the dogs during baseline, dobutamine, and volume infusion conditions. Note that the aortic pressure waveform consistently exhibited a smooth upstroke during the systolic ejection interval and an exponential decay during the diastolic interval despite large variations in EF and mean aortic pressure (MAP). This result generally held for the entirety of the waveform as well as for the waveforms of the remaining five dogs. Thus, the lumped parameter model of Fig. 1a, which accounts for smooth dynamics, was representative of the measured aortic pressure waveforms.

Tables 1 and 2, respectively, include the hemodynamic range for each dog and the average changes in echocardiographic EF and EDV over all the dogs that occurred relative to the baseline period during each of the pharmacological influences and total intravascular volume changes. The employed influences and volume changes imposed a wide spectrum of hemodynamic conditions but did not result in a state of severe systolic dysfunction. EF increased most during dobutamine and decreased most during esmolol and phenylephrine, whereas EDV was enhanced most during phenylephrine and dobutamine and was diminished most during nitroprusside.

Table 1 and Fig. 3 summarize the results of quantitatively comparing the model-based analysis technique to the reference echocardiographic measurements. In particular, Table 2 also includes the average EF and calibrated EDV RMSEs for each dog, while Fig. 3 illustrates Bland–Altman plots of all of the average EF and calibrated EDV errors for the six dogs. The average EF RMSE was 5.6% over all the dogs and was generally consistent in each dog, deviating most in dog 1 with a value of 8.5%. Further, the average EF RMSE showed only a small bias component of ~1%. While the average EF errors did show a negative correlation with the corresponding reference echocardiographic EF values ($\rho = -0.61$), removal of the few large errors in the very high reference EF range ($> \sim 80\%$) substantially reduced this correlation. The average calibrated EDV RMSE was 4.1 mL over all the dogs and was likewise generally consistent in each dog, except for dog 1 with a value of 8.6 mL. The average calibrated EDV RMSE has no bias component due merely to the calibration step. Further, the average calibrated EDV errors were uncorrelated with the corresponding reference echocardiographic EDV values ($\rho = 0.06$). The average C_a value over all the dogs resulting from the EDV calibration step was 0.27 ± 0.11 (SD) mL/mmHg. (Note that the average C_a value that resulted from an analogous CO calibration step was virtually the same.)
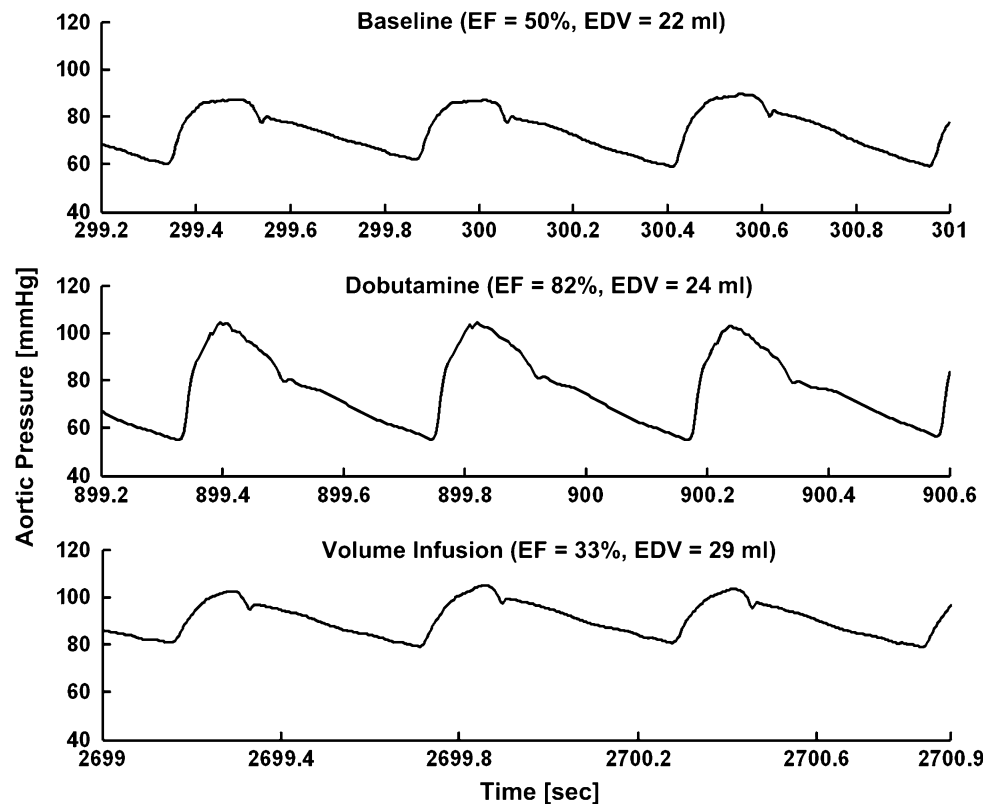
FIGURE 2. Exemplary segments of the aortic pressure waveform measured from the descending thoracic aorta in dog 2 during baseline, dobutamine, and volume infusion conditions.

TABLE 1. Hemodynamic range and quantitative results of the model-based analysis technique for each dog.

Dog	Number of comparisons	EF range (%)	EDV range (mL)	HR range (beats/min)	MAP range (mmHg)	EF RMSE (%)	EDV RMSE (mL)
1	7	53–90	28–46	103–132	67–156	8.5	8.6
2	9	33–84	17–29	94–174	60–94	6.1	1.9
3	10	56–74	21–25	147–179	58–118	4.1	4.5
4	10	52–69	18–23	107–144	42–82	3.4	4.3
5	17	37–74	10–15	60–172	36–116	5.5	1.4
6	9	43–74	13–18	80–140	53–128	5.8	3.3
Total	62	33–90	10–46	60–179	36–156	5.6	4.1

EF is left ventricular ejection fraction; EDV, left ventricular end-diastolic volume; HR, heart rate; MAP, mean aortic pressure; and RMSE, root-mean-squared-error. The EF and EDV ranges were established with the reference echocardiographic measurements.

Figure 4 illustrates the results from all six dogs in terms of a plot of the average EF estimates vs. the corresponding reference echocardiographic values. (Note that an analogous plot of the calibrated EDV results may misleadingly reveal strong correlation simply due to the calibration step.) Figures 5 and 6 illustrate the results from dogs 2 and 5 in terms of trends in the EF, calibrated EDV, and $C_a E_{max}$ estimates (dark lines) as a function of time, along with the corresponding intermittent reference echocardiographic values (gray circles) and the employed pharmacological influences and total intravascular volume changes (underlines). These figures not only further reveal the correspondence between the model-based analysis technique and echocardiography but also demonstrate the advantage of the new technique in providing continuous hemodynamic monitoring.

Table 2 also includes the average changes in the EF and EDV estimates over all the dogs that occurred relative to the baseline period during each of the

TABLE 2. Average changes in EF and EDV via echocardiography and estimated by the model-based analysis technique relative to the baseline period for each of the pharmacological influences and total intravascular volume changes.

Influence/Volume change	Average EF change (%)		Average EDV change (%)	
	Echocardiography	Estimated	Echocardiography	Estimated
Dobutamine	35.6	21.6	20.1	10.9
Phenylephrine	−22.0	−25.5	21.1	52.8
Hemorrhage	1.7	2.3	−5.1	−4.9
Saline	−16.1	−11.4	13.3	12.1
Nitroprusside	14.6	10.8	−7.1	−6.4
Esmolol	−25.7	−17.2	9.8	16.0
Verapamil	4.8	12.2	1.7	−6.7

Values are from one dog for saline, nitroprusside, and verapamil and represent the mean over two dogs for the remaining influences and volume change.
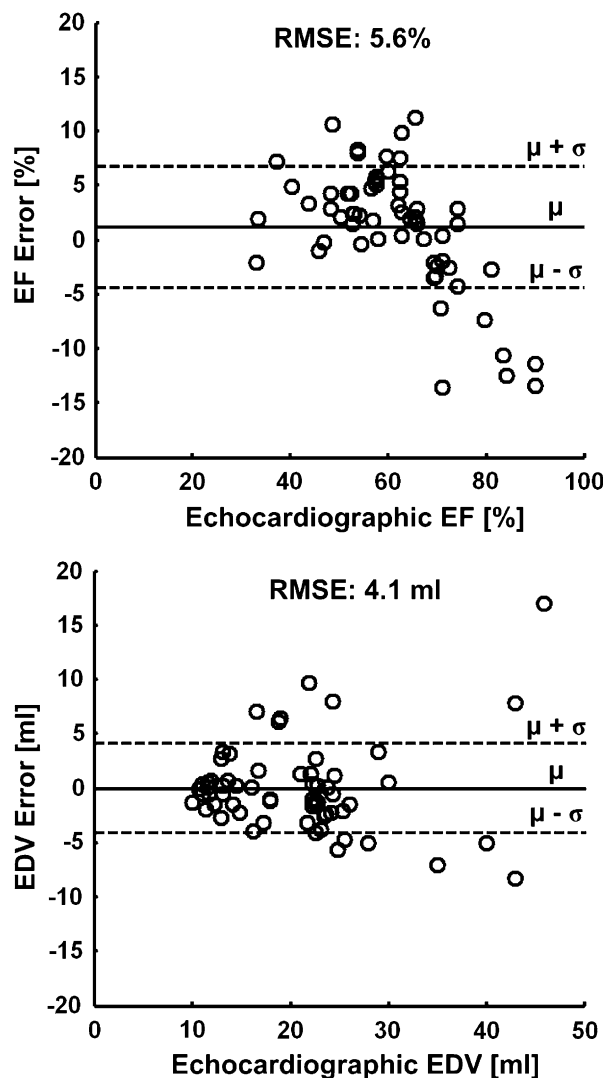

FIGURE 3. Results for all six dogs in terms of Bland–Altman plots of the average left ventricular ejection fraction (EF) and average calibrated left ventricular end-diastolic volume (EDV) errors as a function of the corresponding reference echocardiographic values. The parameter μ indicates the mean of the errors; σ, the standard deviation of the errors; and RMSE the root-mean-square of the errors (i.e., $\sqrt{\mu^2 + \sigma^2}$).
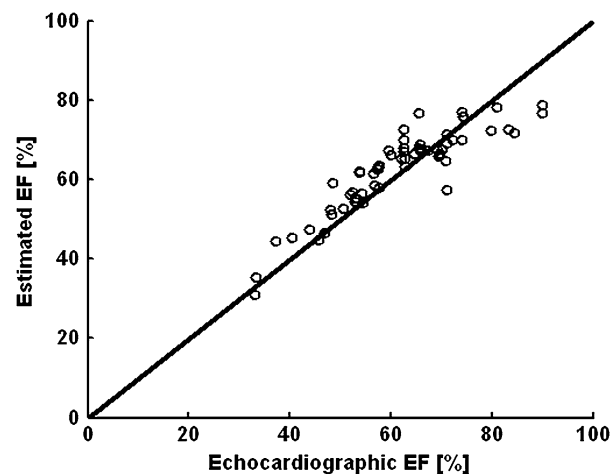

FIGURE 4. Results for all six dogs in terms of a plot of the average EF estimates vs. the corresponding reference echocardiographic EF values.

pharmacological influences and total intravascular volume changes. As can be determined from the corresponding reference changes also in the table, the estimated changes were correct in direction (sign) for all influences and volume changes except for the EDV increase during verapamil, which was modest (1.7 mL). The magnitudes of the estimated changes were also generally reliable, being least accurate for the EDV change during phenylephrine. In addition, as shown in Figs. 5 and 6, C_aE_{max} increased during dobutamine and decreased during esmolol, which is consistent with expectation. Note that, in absence of a reference E_{max} measurement, it is difficult to confirm the step increase in C_aE_{max} that occurred during verapamil in Fig. 6. However, this step increase could represent an actual change as a result of a compensatory response to the precipitous drop in total peripheral resistance that occurred at the same time.

Finally, the beat-to-beat calibrated CO RMSNE was 10.0% for dog 1. This RMSNE had no bias component again because of the calibration step.

FIGURE 5. Results for dog 2 in terms of the trends in the EF, calibrated EDV, and C_aE_{max} estimates (dark lines) as a function of time, along with the corresponding intermittent reference echocardiographic values (gray circles) and the employed pharmacological influences and total intravascular volume changes (underlines).
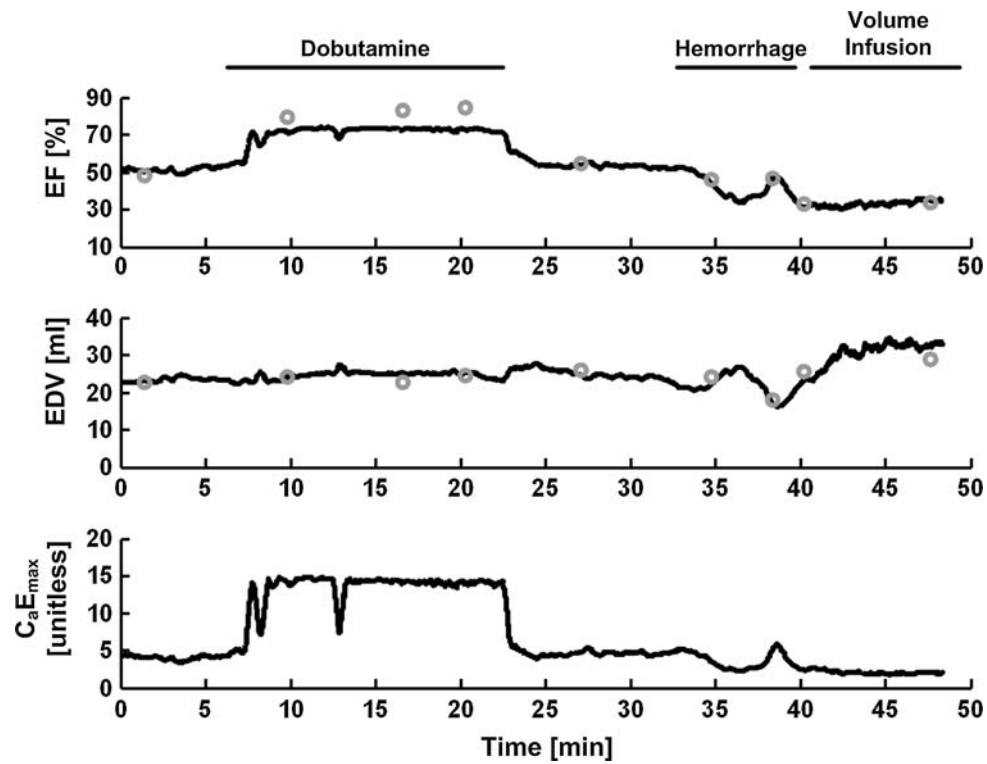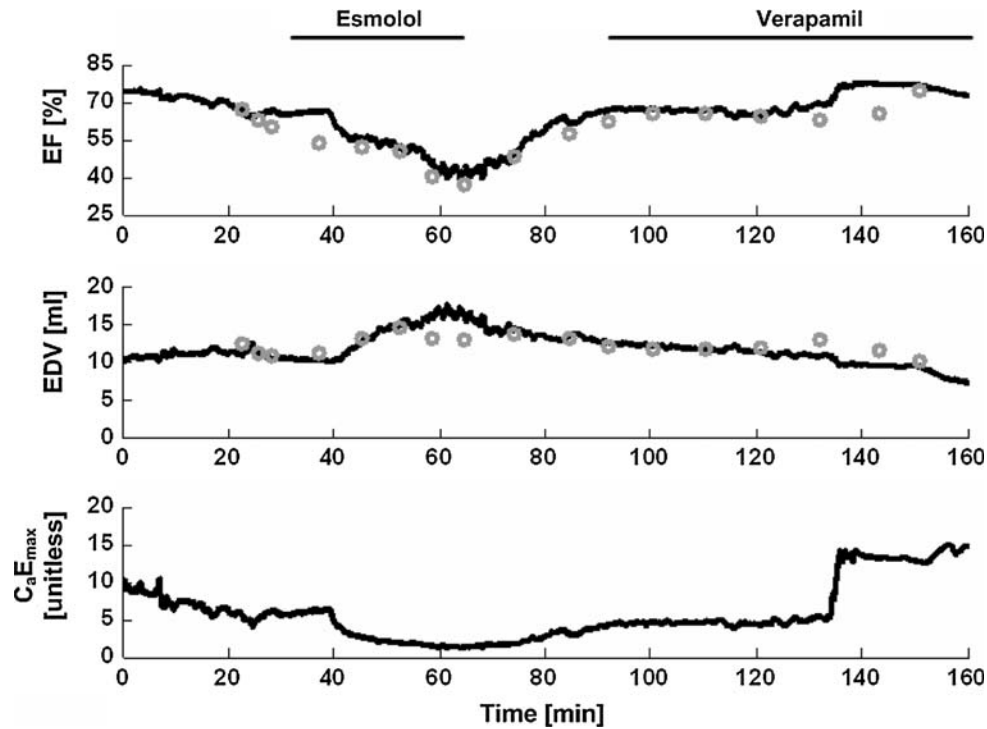

FIGURE 6. Results for dog 5 in terms of the trends in the EF, calibrated EDV, and C_aE_{max} estimates (dark lines) as a function of time, along with the corresponding intermittent reference echocardiographic values (gray circles) and the employed pharmacological influences (underlines).

DISCUSSION

A principal aim of our ongoing research has been to establish new techniques for continuous, automated, and less invasive monitoring of central hemodynamic variables of clinical significance by mathematical analysis of blood pressure waveforms. We have recently introduced and experimentally validated techniques to: (1) estimate relative changes in average CO by long time interval analysis of a single peripheral artery pressure waveform[21,25]; (2) estimate the aortic pressure waveform as well as relative changes in beat-to-beat CO by multichannel blind system identification analysis of two or more peripheral artery pressure waveforms followed by Windkessel modeling[37,38]; and (3) estimate average left atrial pressure as well as relative changes in average CO by extended long time interval analysis of the pulmonary artery pressure waveform.[42] In this study, we sought to complement these previous efforts by tackling the related but different problem of continuous EF monitoring by blood pressure waveform analysis. In contrast to our previous techniques, the novel technique that we introduced and experimentally verified herein for estimating EF is based on physical modeling of the entire blood pressure waveform including its systolic ejection intervals.

More specifically, first, the aortic pressure waveform is represented with a lumped parameter model comprising a three-parameter variable elastance model of the left ventricle connected via a one-way, nonviscous valve to a Windkessel model of the arteries accounting for R_a and the nearly constant C_a. Then, this circulatory model is fitted to each beat of the waveform so as to estimate its lumped parameters to within a scale factor equal to C_a. Finally, these proportional parameter estimates along with a nominal value for V_{lv}^0/C_a are utilized to compute beat-to-beat absolute EF by cancelation of the C_a scale factor. In this way, in contrast to conventional imaging methods, EF may be continuously monitored without making any assumptions about the left ventricular geometry. In addition, with the proportional parameter estimates, relative changes in EDV, SV, CO, R_a, and E_{max} may also be monitored on a beat-to-beat basis. Note that the traditional method for determining E_{max}, in particular, is much more cumbersome, requiring simultaneous measurements of left ventricular pressure and volume during alterations to the preload and/or afterload.[30,35]

To evaluate the technique, we measured aortic pressure waveforms, intermittent average reference EF and EDV via standard echocardiography, and other cardiovascular variables from six dogs during various pharmacological influences and total intravascular volume changes. Our results revealed a close correspondence between the EF and EDV estimates and their reference values, both visually and quantitatively, with overall RMSEs in average EF and average calibrated EDV of 5.6% and 4.1 mL. The average C_a value of 0.27 ± 0.11 mL/mmHg resulting from the EDV calibration step compares reasonably well to the corresponding value of 0.42 ± 0.06 mL/mmHg previously reported from six dogs.[6] Differences in the C_a values could be at least partly explained by the somewhat larger animals in the previous study as well as the small sample sizes of the two studies. Our results also showed that the changes in the EF and calibrated EDV estimates that occurred during each of the influences and volume changes generally compared well with the corresponding reference changes. Finally, our results provided some evidence for reliable estimation of changes in average E_{max} and beat-to-beat CO.

This study is notable in that it may be the first to demonstrate the feasibility of estimating EF from only a blood pressure waveform.

Assumptions of the Model-Based Analysis Technique

Our model-based analysis technique is based on four major assumptions. We defend each of these assumptions below using known physiology and previous experimental findings.

Assumption 1: Lumped Parameter Model Representation of the Aortic Pressure Waveform

It is well known that the arteries are not simply a lumped system but rather a complicated distributed system with impedance mismatches throughout due to vessel tapering, bifurcations, and caliber changes. As a result, peripheral artery pressure waveforms are heavily corrupted by wave reflections and generally require a distributed model for their representation. However, aortic pressure waveforms are less complicated by wave reflections due to destructive interference and attenuation of the reflected waves reaching the aorta[26] as well as significant time delays between forward and backward waves in the aorta.[1] Thus, aortic pressure waveforms may be more amenable to a lumped parameter model representation. Indeed, consistent with the prediction of the lumped parameter model utilized herein, Bourgeois *et al.*[6] showed that aortic pressure waveforms measured specifically from the descending thoracic aorta exhibit pure exponential diastolic decays over a wide hemodynamic range. We therefore placed the aortic catheter in the descending thoracic aorta in this study, and the resulting aortic pressure waveforms generally confirmed their finding.

Assumption 2: Constant Arterial Compliance

To estimate EF and relative changes in other hemodynamic variables including EDV and CO, the

assumption is precisely that C_a is constant over a monitoring period (e.g., days to weeks) in a given subject. Note that this assumption is relaxed in terms of estimating just EF, as C_a must be invariant only within each cardiac cycle. Indeed, it is well known that C_a decreases gradually over the course of years in a subject.[15] However, previous studies have indicated that C_a tends to decrease with increasing arterial pressure.[15,20] If this inverse relationship were strongly present in the dogs studied herein, EF would be significantly and consistently underestimated, while EDV would be grossly overestimated at high arterial pressures and underestimated at low arterial pressures. However, the EF error bias was small, and the EDV error was only mildly correlated with MAP ($\rho = 0.28$). Thus, C_a may have been sufficiently constant in our study even though MAP was varied over a wide range, which is consistent with previous studies including those by Bourgeois et al.[6,7] (see the Previous Related Techniques subsection below) and us.[21,25,38]

Assumption 3: Three-Parameter Raised Cosine Function Representation of Left Ventricular Elastance During the Systolic Ejection Interval

In a surprising but compelling study, Senzaki et al.[32] showed that experimentally measured $E_{lv}(t)$, normalized both in amplitude and time, were remarkably consistent in 87 patients despite extremely wide variations in their ventricular states. Heldt et al.[16] then showed that these normalized data could be well fitted, especially during the systolic ejection interval (i.e., the higher elastance range), by a raised cosine function with three unknown parameters, E_{min}, E_{max}, and T_s as shown in Fig. 1b. Furthermore, E_{min} may be simply approximated as $0.05 \cdot E_{max}$ as shown by the data of Senzaki et al.[32] (reproduced in Fig. 1b). Thus, $E_{lv}(t)$ during the systolic ejection interval may indeed be well represented using a raised cosine function with three unknown parameters, E_{max}, T_s, and $E_{lv}(n_{bs}T)$. Note that independent estimation of (proportional) E_{min} here would likely be unreliable anyhow, as it would essentially amount to an extrapolation. That is, E_{min} is not directly "seen" by aortic pressure, as the aortic valve is closed during diastole. Further note that attempts to represent $E_{lv}(t)$ with a Gaussian, trapezoidal, exponential, or sinusoidal function[14] and/or allow the ratio of the time period of the downstroke of $E_{lv}(t)$ to T_s to vary (rather than be fixed to 0.5) did not improve our EF estimation results. Finally, it should be emphasized that, while the assumption here constrains the shape of the left ventricular elastance function, its amplitude and width are allowed to vary to account for any changes that may occur in cardiac functioning.

Assumption 4: Nominal Value for Proportional Unstressed Left Ventricular Volume

It is generally appreciated that V_{lv}^0 is usually much smaller than EDV. Thus, in many subjects including the healthy dogs studied herein, V_{lv}^0/C_a may indeed be set to a nominal value or even neglected (i.e., no calibration) without substantially sacrificing the EF estimation accuracy. In fact, varying V_{lv}^0/C_a from 10 to 20 mmHg in this study only altered the EF RMSE by 2%. Alternatively, V_{lv}^0/C_a may be determined by obtaining an independent measurement of EF via imaging and then finding the value of V_{lv}^0/C_a that equalizes the EF estimated by aortic pressure waveform analysis to the independent EF measurement (i.e., single calibration). This alternative approach would be preferred in subjects with cardiac dilatation. Further, for these subjects, large changes in the EF estimated by aortic pressure waveform analysis with the determined V_{lv}^0/C_a may, in turn be utilized as a cue to re-image the heart (i.e., multiple calibrations). Finally, note that it is possible that the ratio of SV to stressed EDV (i.e., $V_{lv}^0/C_a = 0$) could prove to be a valuable indicator of left ventricular function.

Potential Sources of Error

Any violation to the four above assumptions certainly represents a source of the errors reported herein. Another source of the errors is likely imperfect reference echocardiographic measurements due to, for example, individual variations in the trans-thoracic imaging window,[28] inaccuracies in endocardial contour definition,[17] and violation to the underlying ventricular geometry assumptions.[27] Indeed, we suspect that the relatively large EF errors at reference EF values $> \sim 80\%$ were a result of the ventricular geometry assumptions of echocardiography breaking down at the very small ESVs. In addition, we surmise that the EF and EDV RMSEs were largest for dog 1, because the reference values were established by averaging over fewer beats than the other dogs. On the other hand, we do not believe that measurement inaccuracies in the aortic pressure waveforms were a major source of the errors, as high fidelity, micromanometer-tipped catheters were employed.

Computational Speed

Our implementation of the model-based analysis technique included a brute force search over a physiologic range to estimate the three parameters of the raised cosine left ventricular elastance function during the systolic ejection interval. However, the technique may be implemented much more efficiently by exploiting the

fact that the parameters usually do not change much from one beat to the next. For example, we estimated the parameters for one beat using the brute force search and then estimated the parameters for subsequent beats using a local simplex method with the parameter estimates of the previous beat specified as its initial seed. We actually implemented the brute force search for every tenth beat rather than for just the initial beat to attenuate any propagation of error due to, for example, ventricular ectopy. This implementation produced almost the same average EF estimates as the original brute force search and was ten times faster than real time when executed on MATLAB with a standard PC.

Limitation: Aortic Valve Disease

Aortic regurgitation and stenosis are clinically relevant cases for which our model-based analysis technique is not applicable. The case of aortic stenosis may be relatively easy to handle by placing a resistor for estimation in series with the diode as done previously.[14,41] Certainly, such an extension of the technique would require validation through experimental subjects with aortic stenosis. However, the case of aortic regurgitation is considerably more difficult and may be unsolvable. Further, the effects of aortic regurgitation on the performance of the technique are not easy to predict. If aortic regurgitation were present, the technique would likely track total (forward and backward) flow rather than the more important forward flow. Thus, proportional CO and perhaps proportional EDV would be overestimated, while EF may be less affected due to a cancelation of errors.

Previous Related Techniques

We find no techniques in the literature aiming to likewise monitor EF from only blood pressure waveforms. However, we are aware of two closely related previous techniques.

Bourgeois *et al.*[7] developed a technique to monitor relative changes in beat-to-beat SV by analysis of the aortic pressure waveform using the two-parameter Windkessel model of the arteries employed herein. Their technique specifically involved estimating SV to within a constant $1/C_a$ scale factor for each beat using the right-hand side of Eq. (3) with $t = t_{es}$ and τ determined by fitting an exponential to each diastolic interval of the waveform. These investigators applied their technique to canine aortic pressure waveforms measured from the descending thoracic aorta wherein pure exponential diastolic decays are visually apparent (see the Assumptions of the Model-Based Analysis Technique subsection above). As a result, they were able to show excellent agreement between their

technique and the gold standard aortic flow probe over a wide hemodynamic range. Our study builds upon the seminal work of Bourgeois *et al.*[7] by modeling the left ventricle in addition to the arteries so as to also permit the monitoring of beat-to-beat absolute EF and proportional EDV and E_{max}.

Guarini *et al.*[14] and Urzua *et al.*[41] developed a technique to monitor beat-to-beat ventricular and arterial parameters based on analysis of the radial artery pressure waveform. Their technique specifically involved representing the waveform with a parametric variable elastance model of the left ventricle in series with a third-order lumped parameter model of the arteries and then estimating the model parameters for each beat using a two-step procedure conceptually similar to the one utilized herein. However, since these investigators desired the absolute values of the model parameters rather than EF, their technique also necessitated an operator-dependent thermodilution CO measurement. Thus, the technique is not automated and continuous. Moreover, unlike the aortic pressure waveform, the radial artery pressure waveform is heavily corrupted by wave reflections and is therefore generally unsuitable for representation with lumped parameter models, particularly those of low order (see the Assumptions of the Model-Based Analysis Technique subsection above). Indeed, these investigators did not experimentally verify their technique against reference methods.

Potential Applications and Future Directions

Our model-based analysis technique may potentially be utilized in lieu of, or as a complement to, imaging methods so as to permit continuous monitoring of EF as well as other important proportional hemodynamic variables in subjects without aortic stenosis and regurgitation and instrumented with an aortic catheter. Examples of such subjects include animals in the context of research and patients undergoing cardiac catheterization or with intra-aortic balloon pumps. To eventually realize these applications, we plan to conduct further testing of the technique in both animals and humans, especially with severe systolic dysfunction.

In addition, we intend to adapt the technique to peripheral artery pressure waveforms, which, in contrast to aortic pressure waveforms, are routinely available in clinical practice via invasive catheters and can be measured non-invasively (see the Introduction section). However, as we have discussed, analysis of peripheral artery pressure waveforms is technically more difficult due to significant distortion by wave reflections. To overcome this difficulty, we propose to first mathematically reconstruct the aortic pressure waveform from measured peripheral artery pressure

waveforms using our multichannel blind system identification technique[37,38] or possibly even the conventional generalized transfer function[9,33] and then apply the model-based analysis technique to the reconstructed waveform.

Our hope is that these future directions ultimately lead to widespread automated and continuous EF monitoring by arterial pressure waveform analysis in various inpatients and outpatients as well as heart failure patients at home so as to help meet the increasing patient monitoring demands.

ACKNOWLEDGMENTS

REFERENCES

[1]Albaladejo, P., et al. Heart rate, arterial stiffness, and wave reflections in paced patients. Hypertension 38:949–952, 2001. doi:10.1161/hy1001.096210.

[2]Ansari, M., and M. Barry. Heart failure: how big is the problem? Who are the patients? What does the future hold? Am. Heart J. 146(1):1–4, 2003.

[3]Berger, R. D., J. P. Saul, and R. J. Cohen. Transfer function analysis of autonomic regulation. I. Canine atrial rate response. Am. J. Physiol. Heart Circ. Physiol. 256:126–131, 1989.

[4]Bland, J. M., and D. G. Altman. Statistical methods for assessing agreement between two methods of clinical measurement. Lancet 1(8476):307–310, 1986.

[5]Bosch, X., and P. Theroux. Left ventricular ejection fraction to predict early mortality in patients with non-ST-segment elevation acute coronary syndromes. Am. Heart J. 150:215–220, 2005. doi:10.1016/j.ahj.2004.09.027.

[6]Bourgeois, M. J., et al. Characteristics of aortic diastolic pressure decay with application to the continuous monitoring of changes in peripheral vascular resistance. Circ. Res. 35(1):56–66, 1974.

[7]Bourgeois, M. J., et al. Wood continuous determination of beat-to-beat stroke volume from aortic pressure pulses in the dog. Circ. Res. 39(1):15–24, 1976.

[8]Burkhoff, D. The conductance method of left ventricular volume estimation methodologic limitations put into perspective. Circulation 81(2):703–706, 1990.

[9]Chen, C. H., et al. Estimation of central aortic pressure waveform by mathematical transformation of radial tonometry pressure. Validation of generalized transfer function. Circulation 95:1827–1836, 1997.

[10]Cintron, G., et al. Prognostic significance of serial changes in left ventricular ejection fraction in patients with congestive heart failure. Circulation 87(6):17–23, 1993.

[11]Critchley, L. A. H., and J. A. J. H. Critchley. A meta-analysis of studies using bias and precision statistics to compare cardiac output measurement techniques. J. Clin. Monit. Comput. 15:85–91, 1999. doi:10.1023/A:1009982611386.

[12]Curtis, J. P., et al. The association of left ventricular ejection fraction, mortality, and cause of death in stable outpatients with heart failure. J. Am. Coll. Cardiol. 42(4):736–742, 2003. doi:10.1016/S0735-1097(03)00789-7.

[13]Dellegrottaglie, S., et al. Non-imaging nuclear monitoring of left ventricular function: twenty-five years of technical development and clinical experience. Ital. Heart J. 3(5):300–307, 2002.

[14]Guarini, M., et al. Estimation of cardiac function from computer analysis of the arterial pressure waveform. IEEE Trans. Biomed. Eng. 45(12):1420–1428, 1998. doi:10.1109/10.730436.

[15]Hallock, P., and J. C. Benson. Studies on the elastic properties of human isolated aorta. Am. J. Physiol. 16:595–602, 1937.

[16]Heldt, T., et al. Computational modeling of cardiovascular response to orthostatic stress. J. Appl. Physiol. 92(3):1239–1254, 2002.

[17]Hof, A. W. V., et al. Comparison of radionuclide angiography with three echocardiographic parameters of left ventricular function in patients after myocardial infarction. Int. J. Card. Imaging 14(6):413–418, 1998. doi:10.1023/A:1006082214191.

[18]Igarashi, Y., et al. Transient vs. steady end-systolic pressure-volume relation in dog left ventricle. Am. J. Physiol. Heart Circ. Physiol. 252:998–1004, 1987.

[19]Katz, A. M. Physiology of the Heart. New York: Raven Press, 1992.

[20]Li, J. K., and Y. Zhu. Arterial compliance and its pressure dependence in hypertension and vasodilation. Angiology 45(2):113–117, 1994. doi:10.1177/000331979404500205.

[21]Lu, Z., and R. Mukkamala. Continuous cardiac output monitoring in humans by invasive and non-invasive peripheral blood pressure waveform analysis. J. Appl. Physiol. 101(2):598–608, 2006. doi:10.1152/japplphysiol.01488.2005.

[22]Marino, P. L. The ICU Book. Baltimore, MD: Lippincott Williams & Wilkins, 1998.

[23]Martinez, J. P., et al. A wavelet-based ECG delineator: evaluation on standard databases. IEEE Trans. Biomed. Eng. 51(4):570–581, 2004. doi:10.1109/TBME.2003.821031.

[24]Mukkamala, R., et al. Continuous left ventricular ejection fraction monitoring by central aortic pressure waveform analysis. Conf. Proc. IEEE Eng. Med. Biol. Sci. 28:620–623, 2006.

[25]Mukkamala, R., et al. Continuous cardiac output monitoring by peripheral blood pressure waveform analysis. IEEE Trans. Biomed. Eng. 53(3):459–467, 2006. doi:10.1109/TBME.2005.869780.

[26]Noordergraaf, A. Circulatory System Dynamics. New York: Academic Press, 1978.

[27]Nosir, Y. F., et al. Accurate measurement of left ventricular ejection fraction by three-dimensional echocardiography. Circulation 94(3):460–466, 1996.

[28]Rumberger, J. A., et al. Determination of ventricular ejection fraction: a comparison of available imaging methods. Mayo Clin. Proc. 72:860–870, 1997.

[29]Rushmer, R. F., D. L. Franklin, and R. M. Ellis. Left ventricular dimensions recorded by sonocardiometry. Circ. Res. 4:684–688, 1956.

[30]Sagawa, K., et al. End-systolic pressure/volume ratio: a new index of ventricular contractility. *Am. J. Cardiol.* 40:748–753, 1977. doi:10.1016/0002-9149(77)90192-8.

[31]Schiller, N. B. Two-dimensional echocardiographic determination of left ventricular volume, systolic function, and mass. Summary and discussion of the 1989 recommendations of the American Society of Echocardiography. *Circulation* 84(3):280–287, 1991.

[32]Senzaki, H., C. H. Chen, and D. A. Kass. Single-beat estimation of end-systolic pressure-volume relation in humans. A new method with the potential for non-invasive applications. *Circulation* 94:2497–2506, 1996.

[33]Soderstrom, S., et al. Can a clinically useful aortic pressure wave be derived from a radial pressure wave? *Br. J. Anaesth.* 88:481–488, 2002. doi:10.1093/bja/88.4.481.

[34]Sridhara, B. S., et al. Rate of change of left ventricular ejection fraction during exercise is superior to the peak ejection fraction for predicting functionally significant coronary artery disease. *Br. Heart J.* 70:507–512, 1993. doi:10.1136/hrt.70.6.507.

[35]Suga, H., and K. Sagawa. Instantaneous pressure-volume relationships and their ratio in the excised supported canine left ventricle. *Circ. Res.* 35:117–126, 1974.

[36]Sutton, M. S. J., et al. Quantitation of left ventricular volumes and ejection fraction in post-infarction patients from biplane and single plane two-dimensional echocardiograms. A prospective longitudinal study of 371 patients.

Eur. Heart J. 19(5):808–816, 1998. doi:10.1053/euhj.1997.0852.

[37]Swamy, G., et al. Blind identification of the aortic pressure waveform from multiple peripheral artery pressure waveforms. *Am. J. Physiol.* 292:2257–2264, 2007.

[38]Swamy, G., and R. Mukkamala. Estimation of the aortic pressure waveform and beat-to-beat cardiac output from multiple peripheral artery pressure waveforms. *IEEE Trans. Biomed. Eng.* 55(5):1521–1529, 2008. doi:10.1109/TBME.2007.913408.

[39]Swamy, G., et al. Continuous ejection fraction estimation by model-based analysis of an aortic pressure waveform: comparison to echocardiography. *Conf. Proc. IEEE Eng. Med. Biol. Sci.* 29:963–966, 2007.

[40]U.S. Department of Health and Human Services, HRASA, Bureau of Health Professions, National Center for Health Workforce Analysis. Projected supply, demand and shortages of registered nurses: 2000–2020, 2002.

[41]Urzua, J., et al. Estimation of ventricular volume and elastance from the arterial pressure waveform. *J. Clin. Monit. Comput.* 14(3):177–181, 1998. doi:10.1023/A:1007459404104.

[42]Xu, D., N. B. Olivier, and R. Mukkamala. Continuous cardiac output and left atrial pressure monitoring by long time interval analysis of the pulmonary artery pressure waveform: proof-of-concept in dogs. *J. Appl. Physiol.* 106(2):651–661, 2009.

Estimation of the Aortic Pressure Waveform and Beat-to-Beat Relative Cardiac Output Changes From Multiple Peripheral Artery Pressure Waveforms

Gokul Swamy, *Student Member, IEEE*, and Ramakrishna Mukkamala*, *Member, IEEE*

Abstract—We introduce a patient- and time-specific technique to estimate the clinically more relevant aortic pressure (AP) waveform and beat-to-beat relative changes in cardiac output (CO) from multiple peripheral artery pressure (PAP) waveforms distorted by wave reflections. The basic idea of the technique is to first estimate the AP waveform by applying a new multichannel blind system identification method that we have developed (rather than the conventional generalized transfer function) to the PAP waveforms and then estimate the beat-to-beat proportional CO by fitting a Windkessel model to the estimated waveform in which wave distortion should be attenuated. We present an evaluation of the technique with respect to four swine datasets including simultaneous measurements of two peripheral AP waveforms, a reference AP waveform, and reference aortic flow probe CO during diverse hemodynamic interventions. Our results show an overall AP waveform error of 3.5 mmHg and an overall beat-to-beat CO error of 12.9% (after a single CO calibration in each animal). These estimation errors represent substantial improvements compared to those obtained with several alternative PAP waveform analysis techniques. With further successful testing, the new technique may ultimately be employed for automated and less invasive monitoring of central hemodynamics in various cardiovascular patients.

Index Terms—Aortic pressure (AP), arterial tree, blood pressure, cardiac output (CO), generalized transfer function, hemodynamics, multichannel blind system identification (MBSI), peripheral artery pressure (PAP), wave reflections, Windkessel model.

I. INTRODUCTION

BLOOD ejected by the left ventricle initiates pressure and flow waves that propagate through the arterial tree. These waves are reflected at multiple sites of impedance mismatch caused by arterial bifurcations, narrowing, and stiffening [1], [2]. For example, wave reflections are especially pronounced at the sites of arterial terminations [1]–[3]. The pressure waveform measured at a given site in the arterial tree therefore represents the sum of the forward and backward traveling pressure waves at that particular site [3], [4]. As a result, the arterial pressure waveform becomes progressively distorted as its site of measurement becomes more distal to the aorta [1]. Most notably,

systolic pressure (SP) and pulse pressure (PP) become increasingly amplified [1], [5], and therefore, less indicative of cardiac performance [6]. Indeed, central measurements of SP and PP have been shown to be superior predictors of patient outcome than corresponding measurements made in more peripheral arteries [7], [8]. In addition, aortic pressure (AP, especially from the descending thoracic aorta) is less complicated by wave reflections as compared to peripheral artery pressure (PAP) due in part to attenuation and destructive interference of the reflected waves that reach the aorta [2], [9], [10]. Thus, the entire AP waveform usually reveals the ventricular systolic ejection interval (SEI) through the dicrotic notch [11] and may be represented with a lumped parameter Windkessel model in order to accurately estimate beat-to-beat relative changes in cardiac output (CO), as convincingly demonstrated in [10]. On the other hand, PAP may be measured more safely than AP through catheterization and even noninvasively via finger-cuff photoplethysmography [12] or applanation tonometry [13]. It is therefore PAP waveforms that are routinely monitored in humans [14], even though the AP waveform is known to be of greater clinical value.

As a result, over the past 15 years, there has been considerable interest in estimating the AP waveform from measured PAP waveforms using generalized transfer function techniques [5], [6], [11], [15]–[19]. These techniques essentially involve: 1) initially obtaining simultaneous measurements of AP and PAP waveforms in a group of subjects; 2) estimating a group-averaged transfer function relating the measured PAP to the measured AP; and 3) subsequently applying this transfer function to PAP measured from a new subject in order to estimate the AP waveform. However, these techniques do not account for known interpatient and temporal variability of arterial tree properties [20], [21], and may therefore, be prone to significant estimation error when applied to the diverse patient population encountered in clinical practice.

We have recently developed a patient- and time-specific technique for estimating the AP waveform from multiple PAP waveforms by capitalizing on the powerful multichannel blind system identification (MBSI) approach [22]. The technique specifically involves: 1) modeling two or more measured PAP waveforms as outputs of distinct finite impulse response (FIR) channels driven by the common AP waveform input (see dark blocks in Figs. 1 and 2) estimating the FIRs to within an arbitrary scale factor by applying the standard eigenvector method to the cross-relations between pairs of measured outputs [see (1) and (2)]; 3) reconstructing the AP waveform to within an arbitrary scale factor by deconvolving the estimated FIRs from the
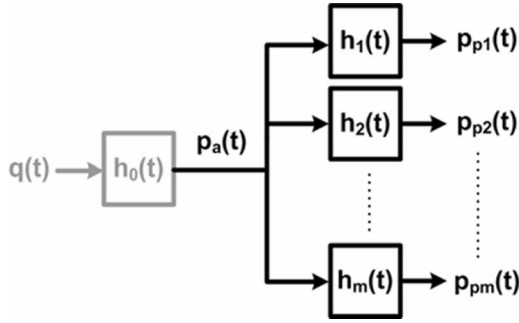
Fig. 1. Dark blocks represent the linear and time-invariant (LTI) relationship between AP and measured PAP (RAP and FAP in our setup). The assumption of coprime impulse responses of dark blocks permits their identification from PAP waveforms and AP waveform reconstruction by MBSI method. An undetermined gain factor is derived by assuming uniform mean arterial pressure. The light block represents the input–output relationship between aortic flow and AP waveforms and is modeled as a two-element (total peripheral resistances R_a, lumped arterial compliance C_a) Windkessel. Beat-to-beat relative CO changes are reconstructed after estimation of the Windkessel time constant $\tau = R_a C_a$ from the reconstructed AP and separating the two factors, by assuming a constant C_a after initial calibration.
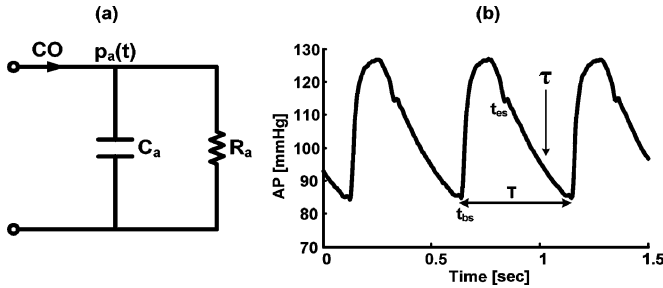

Fig. 2. (a) Lumped parameter Windkessel model providing the basis for the technique to estimate beat-to-beat relative changes in CO from the estimated AP waveform [$p_a(t)$] in which the wave distortion should be greatly attenuated (see Fig. 1). The model accounts for the lumped arterial compliance (C_a) of the large arteries and the total peripheral resistance (R_a) of the small arteries. The technique estimates beat-to-beat proportional CO from the estimated AP waveform based on the governing model equation [see (12)]. (b) Illustration generally indicating how the unknown timing parameters in (12), namely t_{bs} (beginning time of the SEI), t_{es} (ending time of the SEI), T (cardiac cycle duration), and $\tau = R_a C_a$ (time constant of the Windkessel model), are determined from the estimated AP waveform.

measured waveforms; and 4) scaling the reconstructed waveform to absolute pressure by invoking Poiseuille's law. In this way, the technique is able to estimate the AP waveform from PAP waveforms without the need for a generalized transfer function. We have tested this technique with respect to four swine datasets consisting of simultaneous measurements of two PAP waveforms from the femoral and radial arteries and a measured reference AP waveform during diverse hemodynamic interventions [22]. Our results showed that the technique provided more accurate AP waveform estimates than did a generalized transfer function developed from a subset of the same datasets.

In this paper, we introduce an improved technique for estimating the AP waveform as well as beat-to-beat relative changes in CO from multiple PAP waveforms. The technique specifically involves: 1) estimating the AP waveform based on our new MBSI method in which the FIRs are represented with more efficient basis functions than the impulse basis functions assumed by the standard eigenvector method in order to reduce the number of parameters to be estimated and therefore enhance the estimation accuracy and 2) estimating beat-to-beat relative changes in CO by fitting a Windkessel model to the estimated AP waveform in which wave distortion should be greatly attenuated. We show that this new technique is able to estimate the AP waveforms in the four aforementioned swine datasets with greater accuracy than our initial technique. We further show that this enhanced accuracy permits a reliable estimation of beat-to-beat relative changes in CO as compared to gold standard reference aortic flow probe measurements also available in the swine datasets.

II. THE TECHNIQUE

Our technique applies a new MBSI method that we have developed to two or more PAP waveforms to estimate the AP waveform and then fits a Windkessel model to the estimated waveform to estimate beat-to-beat relative changes in CO. We describe the technique later for the simplest case in which two PAP waveforms are available for analysis. Generalization of the technique to more than two measured waveforms readily follows analogous to [23].

First, two measured and sampled PAP waveforms [$p_{pi}(t)$, $i \in [1, 2]$] are modeled as individual outputs of two unknown channels driven by the common unknown and likewise sampled AP waveform [$p_a(t)$] input, as shown with dark blocks and $m = 2$ in Fig. 1. The two discrete-time channels coupling the common input to the two distinct outputs represent the dynamic properties of a different path in the arterial tree. A principal assumption underlying the model is that the channels may be well characterized by coprime FIRs [$h_i(t)$, $i \in [1, 2]$] over each 1 min interval of analysis (see later). Over such short time intervals, the arterial tree is usually operating in near steady-state conditions, thereby clearly supporting the implicit time invariance assumption as well as buttressing the implicit linearity assumption as argued in [24] and references therein. Moreover, since pressure waveforms measured from distinct sites in the arterial tree only differ significantly over short time scales (e.g., within a cardiac cycle) while being quite similar over longer time scales (e.g., mean values as described later) [2], [25], the FIR assumption is also well justified. Finally, the coprime assumption, which is needed to subsequently estimate the FIRs [23], is tenable due to the significant differences in PAP waveforms measured from distinct arterial sites.

Then, by applying the fundamental properties of convolution to the single-input, multioutput model of Fig. 1 (dark blocks), the two FIRs may be estimated based on the resulting cross-relation between the two measured outputs:

$$\sum_{\tau=0}^{L-1} h_1(\tau) p_{p2}(t-\tau) - \sum_{\tau=0}^{L-1} h_2(\tau) p_{p1}(t-\tau) = e(t),$$
$$t \in [L-1, N-1]. \tag{1}$$

Here, $e(t)$ has been included to account for any measurement and/or modeling error, and the variables L and N, respectively, represent the maximum duration of the FIRs (channel order)

and the number of measured PAP waveform samples in a 1 min interval of analysis [23].

The standard method for estimating the FIRs in (1) is to first determine the channel order through eigenvalue analysis and then to estimate the FIR samples or parameters to within an arbitrary scale factor by least squares minimization of $e(t)$ via the eigenvector method [23]. More specifically, (1) may be expressed in a matrix form by stacking each individual equation, corresponding to each t, one on top of the other as follows:

$$\underbrace{\begin{bmatrix} \mathbf{P_{p2}} & -\mathbf{P_{p1}} \end{bmatrix}}_{\mathbf{P}} \underbrace{\begin{bmatrix} \mathbf{h_1} \\ \mathbf{h_2} \end{bmatrix}}_{\mathbf{h}} = \mathbf{e} \qquad (2)$$

where

$$\mathbf{P_{pi}} = \begin{bmatrix} p_{pi}(0) & p_{pi}(1) & \cdots & p_{pi}(L-1) \\ p_{pi}(1) & p_{pi}(2) & \cdots & p_{pi}(L) \\ \vdots & \vdots & \ddots & \vdots \\ p_{pi}(N-L) & p_{pi}(N-L+1) & \cdots & p_{pi}(N-1) \end{bmatrix},$$
$$i \in [1,2] \qquad (3)$$

are $[(N-L+1 \times L]$ Hankel matrices comprising the respective measured output samples, $\mathbf{h_i} = [h_i(L-1)\ h_i(L-2) \cdots h_i(0)]^T$, $i \in [1,2]$, are $[L \times 1]$ vectors specifying the parameters of the two respective FIRs, and $\mathbf{e} = [e(0)\ e(1) \cdots e(N-L)]^T$ is an $[(N-L+1) \times 1]$ vector consisting of the error samples. The channel order L may then be determined by: 1) forming a matrix $\mathbf{P}$ of dimension $[(N-L_{\max}+1) \times 2L_{\max}]$, where $L_{\max}$ is assumed to encompass the true channel order; 2) computing the eigenvalues of the matrix $\mathbf{P}^T\mathbf{P}$; 3) identifying the number of insignificant eigenvalues (n_{ie}); and 4) selecting the optimal value of L as $L_{\mathrm{opt}} = L_{\max} - (n_{ie}-1)$. Then, the least squares, unit two-norm estimate of the vector $\mathbf{h}$ may be conveniently obtained by selecting the eigenvector associated with the minimum eigenvalue of the matrix $\mathbf{P}^T\mathbf{P}$, where $\mathbf{P}$ is of dimension $[(N-L_{\mathrm{opt}}+1) \times 2L_{\mathrm{opt}}]$. The implicit assumption of this standard eigenvector method, which was employed by our initial MBSI technique [22], is that the AP waveform contains at least as many frequency components as the number of estimated FIR parameters ($2L_{\mathrm{opt}}$) [23].

To reduce the number of parameters to be estimated so as to alleviate the frequency content demands on the AP waveform and thereby improve the estimation accuracy, the FIRs are instead compactly represented with damped sinusoidal basis functions as

$$h_i(t) = \sum_{k=1}^{n} \lambda^t (a_{ik} \cos(\omega_{ik}t) + b_{ik} \sin(\omega_{ik}t)), \quad i \in [1,2]$$
$$(4)$$

where $\{\lambda, a_{ik}, b_{ik}, \omega_{ik}\}$ is a set of unknown parameters and n is an unknown number of basis functions. These basis functions were chosen empirically based on our swine datasets (see Section V). Thus, only a small number of basis functions should be needed to represent the FIRs, thereby resulting in a significant reduction in the parameters to be estimated. Then, for a fixed number of basis functions n, the set of parameters is

estimated based on least squares minimization of $e(t)$ in the following cross-relation equation resulting from substitution of (4) into (1):

$$\sum_{k=1}^{n} \left(a_{1k} \sum_{\tau=0}^{L_{\mathrm{opt}}-1} \lambda^\tau \cos(\omega_{1k}\tau) p_{p2}(t-\tau) \right.$$
$$\left. + b_{1k} \sum_{\tau=0}^{L_{\mathrm{opt}}-1} \lambda^\tau \sin(\omega_{1k}\tau) p_{p2}(t-\tau) \right)$$
$$- \sum_{k=1}^{n} \left(a_{2k} \sum_{\tau=0}^{L_{\mathrm{opt}}-1} \lambda^\tau \cos(\omega_{2k}\tau) p_{p1}(t-\tau) \right.$$
$$\left. + b_{2k} \sum_{\tau=0}^{L_{\mathrm{opt}}-1} \lambda^\tau \sin(\omega_{2k}\tau) p_{p1}(t-\tau) \right) = e(t),$$
$$t \in [L_{\mathrm{opt}}-1, N-1] \qquad (5)$$

where L_{opt} is established through eigenvalue analysis as described before with $L_{\max}=15$. To estimate the coefficient parameter sets $\{a_{ik}, b_{ik}\}$ uniquely (rather than to within an arbitrary scale factor), one FIR is constrained to have unity gain as follows:

$$\sum_{k=1}^{n} a_{1k} \sum_{t=0}^{L_{\mathrm{opt}}-1} \lambda^t \cos(\omega_{1k}t) + \sum_{k=1}^{n} b_{1k} \sum_{t=0}^{L_{\mathrm{opt}}-1} \lambda^t \sin(\omega_{1k}t) = 1.$$
$$(6)$$

The constraint here is well justified, as the paths from the aorta to the peripheral arteries offer very little resistance to blood flow due to Poiseuille's law (i.e., the mean values of pressure waveforms from different sites in the arterial tree are nearly the same) [2]. To simplify this constrained optimization problem, the damping parameter λ is set to $\exp(-3/L_{\mathrm{opt}})$ so that the FIRs approximately decay to zero, while the frequencies in the parameter set ω_{ik} are allowed to take on only discrete values according to the Fourier series [i.e., $2\pi l/L_{\mathrm{opt}}$ for $l = 0, 1, \ldots,$ ceil$((L_{\mathrm{opt}}-1)/2)$, where ceil(x) is the smallest integer $\geq x$]. For each set of frequency parameters ω_{ik} considered (see later), the corresponding coefficient parameter sets are estimated through the linear least squares solution. More specifically, similar to (1), (5) and (6) may be expressed in matrix form as follows:

$$\underbrace{\begin{bmatrix} \mathbf{P_2^1} & \mathbf{P_2^2} & -\mathbf{P_1^1} & -\mathbf{P_1^2} \end{bmatrix}}_{\mathbf{A}} \underbrace{\begin{bmatrix} \mathbf{a_1} \\ \mathbf{b_1} \\ \mathbf{a_2} \\ \mathbf{b_2} \end{bmatrix}}_{\mathbf{x}} = \underbrace{\begin{bmatrix} 0 \\ \vdots \\ 0 \\ 1 \end{bmatrix}}_{\mathbf{b}} + \mathbf{e} \qquad (7)$$

where

$$\mathbf{P_i^j} = \begin{bmatrix} \mathbf{P_{pi}} \\ \varphi \end{bmatrix}$$

$$\times \begin{bmatrix} \lambda^{L_{\mathrm{opt}}-1} f((L_{\mathrm{opt}}-1)\omega_{i1}) & \cdots & \lambda^{L_{\mathrm{opt}}-1} f((L_{\mathrm{opt}}-1) \times \omega_{in}) \\ \vdots & \ddots & \vdots \\ \lambda^0 f(0 \times \omega_{i1}) & \cdots & \lambda^0 f(0 \times \omega_{in}) \end{bmatrix},$$

$$f(x) = \begin{cases} \cos(x), & j=1 \\ \sin(x), & j=2 \end{cases} \qquad (8)$$

where $\mathbf{P_{pi}}$ is defined in (3) with $L = L_{opt}$, φ is a $[1 \times L_{opt}]$ vector whose elements are all zeros for $i = 1$ and all ones for $i = 2$, and $\mathbf{a_i} = [a_{i1} \cdots a_{in}]^T$ and $\mathbf{b_i} = [b_{i1} \cdots b_{in}]^T$, $i \in [1, 2]$, are $[n \times 1]$ vectors specifying the coefficient parameters of the two respective FIRs. Then, the least squares estimate of the vector $\mathbf{x}$ in (7) is obtained as $\mathbf{x} = (\mathbf{A}^T\mathbf{A})^{-1}\mathbf{A}^T\mathbf{b}$. Among all of the linear least squares solutions computed for each considered set of frequency parameters $\{\omega_{ik}\}$, the one that minimizes the two-norm of the vector $\mathbf{e}$ in (7) is selected so as to provide the optimal estimate of the parameter set $\{a_{ik}, b_{ik}, \omega_{ik}\}$. Finally, the number of basis functions n is determined iteratively by starting with a single basis function representation and then adding one basis function at a time until the two-norm of the vector $\mathbf{e}$ becomes $<10\%$ of the two-norm of the vector $(\mathbf{p_{p1}} + \mathbf{p_{p2}})/2$, where $\mathbf{p_{pi}} = [p_{pi}(0) \ p_{pi}(1) \ \cdots \ p_{pi}(N-1)]^T$, $i \in [1, 2]$, are $[N \times 1]$ vectors comprising the measured output samples. For further simplicity, in the kth iteration, the frequency parameters are only estimated for the newly added basis function with the frequency parameters of the previous $(k-1)$ basis functions set to the estimates obtained from the $(k-1)$th iteration. In the kth iteration, the number of sets of frequency parameters considered is specifically $(\text{ceil}((L_{opt}-1)/2) - k + 2)^2$. Thus, the two FIRs are assumed to be represented by the same number of basis functions but of generally different frequencies.

Next, with the set of basis function parameters $\{\lambda, a_{ik}, b_{ik}, \omega_{ik}\}$ estimated and the two FIRs fully defined through (4), the common AP waveform input of the model of Fig. 1 (dark blocks) is estimated through multichannel least squares deconvolution, as described in detail in [22] with Tikhonov regularization [27]. The estimated AP waveform is then low-pass filtered in order to further attenuate any high-frequency noise generated in the deconvolution process. It should be noted that the estimated AP waveform will be slightly delayed (<0.1 s) with respect to the actual AP waveform, because the time delay shared by the FIRs cannot be identified with MBSI.

Finally, beat-to-beat relative changes in CO are estimated from the determined AP waveform by employing the Windkessel model of Fig. 2(a), which accounts for the lumped arterial compliance (C_a) of the large arteries and the total peripheral resistance (R_a) of the small arteries, as described in [10]. That is, since C_a may be nearly constant over a wide pressure range and on the time scale of months [9], [20], [25], proportional CO for each cardiac cycle is calculated through the following governing model equation:

$$\text{CO} \propto \frac{1}{T}\left(p_a(t_{es}) - p_a(t_{bs}) + \frac{1}{\tau}\int_{t_{bs}}^{t_{es}} p_a(t)dt\right) \quad (9)$$

where $p_a(t)$ is again the estimated AP waveform, and t_{bs}, t_{es}, T, and $\tau = R_aC_a$ are timing parameters that are determined from this waveform, as shown in Fig. 2(b). More specifically, t_{bs}, which denotes the beginning time of the SEI, is identified as the time of the local minimum that immediately precedes the time of peak SP for the cardiac cycle; t_{es}, which indicates the ending time of the SEI, is identified as the time of the minimum of the derivative of the estimated waveform over the interval

from the time of peak SP to the t_{bs} of the next cardiac cycle; T, which signifies the cardiac cycle duration, is determined as the difference between the t_{bs} of successive cardiac cycles; and τ, which is the time constant of the Windkessel model, is estimated by least squares fitting of a single exponential to the reconstructed waveform over an interval between t_{es} and t_{bs} of the next cardiac cycle, in accordance with the model prediction. Since the time constants governing R_a changes are significantly longer than the cardiac cycle duration [27], the τ estimates are actually averaged over five cardiac cycles to attenuate any noise.

III. METHODS

We evaluated the technique with respect to experimental datasets that were originally collected to address related but different specific aims [28] and previously utilized to investigate our initial MBSI technique for estimating the AP waveform using the standard eigenvector method [22]. Briefly, these datasets consist of various hemodynamic recordings obtained from four swine (30–34 kg) under general anesthesia and mechanical ventilation. The hemodynamic recordings include femoral artery pressure (FAP) and radial artery pressure (RAP) waveforms measured with conventionally employed fluid-filled catheters [14], a gold standard reference AP waveform measured from the descending thoracic aorta with a high frequency response micromanometer-tipped catheter, and gold standard reference beat-to-beat CO measured with an aortic flow probe. (Note that, while damping can be an issue with fluid-filled catheters, the technique should at least be impervious to the damping dynamics of the catheters that are coprime [22].)

These hemodynamic recordings are available at a sampling frequency of 250 Hz for a total of 253 min during infusions of volume, phenylephrine, dobutamine, isoproterenol, esmolol, nitroglycerine, and acetylcholine. Table I shows that these interventions imposed a wide hemodynamic parameter range for each of the four swine datasets [but did not elicit bradycardia for swine or a normal resting heart rate (HR) for dogs or humans].

We applied the technique to all 1 min, nonoverlapping intervals of the FAP and RAP waveforms resampled to 50 Hz.

TABLE I
HEMODYNAMIC PARAMETER RANGE OF THE SWINE EVALUATION DATASETS

Hemodynamic Parameter	Animal 1	2	3	4	Total
MAP Range [mmHg]	54 - 136	58 - 117	45 - 114	48 - 119	45 - 136
SP Range [mmHg]	62 - 182	70 - 148	55 - 144	58 - 157	58 - 157
PP Range [mmHg]	17 - 54	17 - 52	20 - 62	19 - 57	17 - 62
SEI Range [msec]	160 - 400	160 - 340	120 - 240	140 - 300	120 - 400
HR Range [beats/min]	100 - 223	92 - 190	91 - 243	102 - 207	91 - 243
CO Range [L/min]	2.3 - 4.1	1.7 - 6.0	2.4 - 5.7	1.3 - 6.2	1.3 - 6.2

The new technique (see Figs. 1 and 2) as well as alternative PAP waveform analysis techniques were evaluated with respect to four swine datasets consisting of simultaneous measurements of FAP and RAP waveforms, a reference AP waveform, and reference aortic flow probe CO during diverse interventions. MAP, mean arterial pressure; SP, systolic pressure from AP; PP, pulse pressure from AP, SEI, systolic ejection interval from AP; HR, heart rate.

We evaluated the resulting AP waveform estimates with respect to the measured reference waveforms (likewise resampled to 50 Hz) in terms of the root-mean-squared-error (RMSE) of the following parameters: total waveform (i.e., sample-to-sample), beat-to-beat SP, beat-to-beat PP, and beat-to-beat SEI. For comparison, we likewise evaluated the PAP waveforms (with respect to the measured AP waveforms) as well as the AP waveform estimates from our initial MBSI technique and autoregressive exogenous input (ARX)-based generalized transfer functions [11] developed on a subset of the swine datasets as described in [22]. (Prior to conducting these evaluations, we advanced the AP waveform estimates and the PAP waveforms so that they were temporally aligned with the measured AP waveforms using standard cross-correlation. This time alignment was done for the sole purpose of fairly evaluating the various techniques.) Since it is customary to report CO errors in percent [29], we evaluated the resulting beat-to-beat proportional CO estimates with respect to the reference aortic flow probe measurements in terms of the root-mean-squared-normalized-error (RMSNE). This quantity was specifically computed by: 1) scaling the proportional CO estimates to have the same mean value as the reference CO in each animal; 2) normalizing each calibrated CO error with the reference CO value; and 3) computing the RMS of the normalized, calibrated CO errors. For comparison, we likewise evaluated the beat-to-beat proportional CO estimates obtained by fitting the Windkessel model directly to the FAP and RAP waveforms as well as to the AP waveforms estimated by our initial technique and the generalized transfer function.

IV. RESULTS

Fig. 3 illustrates examples of the two FIRs estimated by the technique introduced herein, which employs the new MBSI method, from the swine datasets under three different interventions (see solid lines). The figure also includes the corresponding "actual" FIRs established by estimating the impulse responses relating the *measured* AP waveforms to each of the PAP waveforms using standard ARX least squares identification [30] (see dashed lines). (Note that actual is in quotes here, because these FIRs are themselves estimated quotes here, because these FIRs are themselves estimated quantities.) The favorable agreement between the estimated and "actual" FIRs revealed in these examples was indeed typical throughout the swine datasets. The substantial variability in each estimated FIR under the different interventions that is illustrated in these examples was likewise typical. More precisely, in the swine datasets, the overall variability of the estimated FIRs was 65% for the FAP waveform outputs and 47% for the RAP waveform outputs [where variability here is defined as the standard deviation (SD) of the peak amplitude of the FIRs normalized by the mean peak amplitude].

Table II summarizes the evaluation results for the AP waveforms estimated by the new technique for each of the four swine datasets as well as the corresponding results for the measured PAP waveforms. The overall total waveform RMSE of the AP waveform estimates was 3.5 mmHg (after a modest time alignment), whereas the average overall total waveform RMSE between the PAP waveforms and the measured AP waveforms
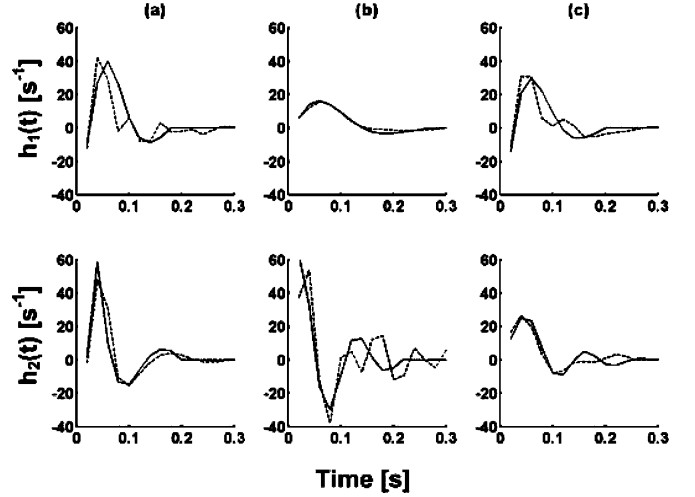

Fig. 3. Examples of the two FIRs estimated by the new technique (solid lines) along with the corresponding "actual" FIRs established by estimating the impulse responses relating the *measured* AP waveform to each of the PAP waveforms (dashed lines) from the swine datasets. (a) Under phenylephrine. (b) Under dobutamine. (c) Under nitroglycerine interventions. The FIRs relating the AP waveform to the FAP waveform are denoted by $h_1(t)$, while the FIRs relating the AP waveform to the RAP waveform are indicated with $h_2(t)$.

was 8.6 mmHg (after a more significant time alignment). Thus, the technique effectively reduced the wave distortion in the measured PAP waveforms by 59%. As a result, the technique also reduced the average overall SP and PP RMSEs by 71% and 61%, respectively. However, the technique did not improve upon the surprisingly small, overall SEI RMSE obtained from the FAP waveforms. Fig. 4(a) provides a visual example illustrating the significant differences between the PAP waveforms and the measured AP waveform, while Fig. 4(b) shows that the AP waveform estimated from these PAP waveforms closely agrees with the directly measured reference waveform.

Table II also provides a comparison of the evaluation results for the AP waveforms estimated by our new technique, our initial MBSI technique, which employs the standard eigenvector method, and previous ARX-based generalized transfer functions for each of the four swine datasets. The overall total waveform RMSE of the AP waveform estimates from our initial technique was 4.6 mmHg, while the average overall total waveform RMSE from the generalized transfer function was 5.4 mmHg. Thus, both MBSI techniques provided more accurate AP waveform estimates than do conventional generalized transfer functions, even though they were developed on a subset of the swine datasets. However, the new technique enhanced the estimation accuracy of our initial technique by 24%. As a result, the new technique provided similar improvements in the estimation of SP and PP (but yielded similar results in the estimation of the SEI). In addition, a more significant advantage of the new technique over the initial technique is indicated later.

Table III includes the evaluation results for the beat-to-beat proportional CO estimated by the new technique via fitting the Windkessel model of Fig. 2(a) to the estimated AP waveform for each of the four swine datasets as well as the corresponding results obtained by directly fitting the model to each of the

TABLE II
QUANTITATIVE SUMMARY OF THE AP WAVEFORM ESTIMATION RESULTS IN
TERMS OF RMSE

Arterial Pressure Waveform	Arterial Pressure Parameter	Animal				
		1	2	3	4	Total
Estimated AP (New Technique)	TW	2.5	3.9	3.4	3.4	3.5
	SP	1.9	5.1	5.0	5.6	4.8
	PP	2.8	5.4	6.4	6.1	5.6
	SEI	22	14	21	22	19
FAP	TW	11.6	7.8	6.3	7.0	8.1
	SP	19.2	13.5	12.0	10.7	13.7
	PP	10.5	14.3	10.2	14.3	12.6
	SEI	22	19	19	20	19
RAP	TW	4.0	10.5	9.4	9.3	9.1
	SP	5.1	24.5	16.7	22.7	19.7
	PP	4.9	19.2	10.3	21.6	15.9
	SEI	20	38	18	48	33
Estimated AP (Initial Technique)	TW	4.4	4.4	3.8	5.7	4.6
	SP	4.1	5.0	5.0	9.4	6.1
	PP	4.3	5.9	7.1	9.9	7.1
	SEI	23	14	22	22	20
Estimated AP (GTF: FAP → AP)	TW	4.8	5.2	6.9	5.6	5.8
	SP	7.4	7.7	12.4	9.6	9.7
	PP	8.6	9.4	13.4	11.2	11.0
	SEI	24	28	46	42	35
Estimated AP (GTF: RAP → AP)	TW	4.2	4.6	6.0	5.1	5.0
	SP	5.3	6.6	8.7	6.5	7.1
	PP	4.8	6.3	8.5	6.8	7.0
	SEI	22	26	35	37	29

The new technique resulted in more accurate AP waveform estimates in the four swine datasets (see Fig. 4) than those obtained from alternative PAP waveform analysis techniques including the conventional generalized transfer function (GTF). The RMSEs are in units of millimeters of mercury for the total waveform (TW), SP, and PP parameters and milliseconds for the SEI parameter.
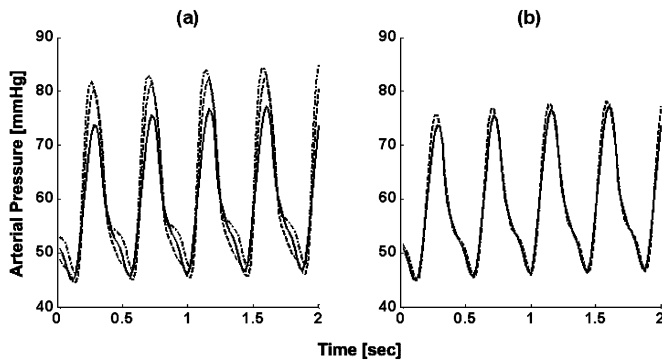

Fig. 4. (a) Example segments of the measured AP (solid), FAP (dash), and RAP (dot-dash) waveforms from one of the four swine datasets (see Table I). (b) Example segments of the AP waveform measured (solid) and estimated (dash) by applying the technique to the two segments of the PAP waveforms (see Fig. 1). See Table II for a complete quantitative summary of the AP waveform estimation results.

PAP waveforms. The overall beat-to-beat CO RMSNE from the AP waveform estimates was 12.9%, whereas the average overall beat-to-beat CO RMSNE from the PAP waveforms was 26%. Thus, the technique enhanced the beat-to-beat CO estimation accuracy by 50%. Interestingly, the overall beat-to-beat CO RMSNE from the FAP waveforms was 49% smaller than the corresponding RMSNE from the RAP waveforms but still 33% larger than the analogous RMSNE obtained with the technique.

TABLE III
QUANTITATIVE SUMMARY OF THE BEAT-TO-BEAT PROPORTIONAL CO
ESTIMATION RESULTS IN TERMS OF RMSNE

Arterial Pressure Waveform for Windkessel modeling	Animal				
	1	2	3	4	Total
Estimated AP (New Technique)	11.8	12.3	15.5	10.5	12.9
FAP	16.6	14.8	17.7	19.6	17.2
RAP	39.0	25.6	22.6	48.6	33.9
Estimated AP (Initial Technique)	44.7	37.8	28.0	37.1	36.3
Estimated AP (GTF: FAP→ AP)	11.6	14.1	26.6	16.0	17.6
Estimated AP (GTF: RAP → AP)	20.0	25.0	19.9	26.0	22.8

The new technique (see Fig. 2) also resulted in more accurate beat-to-beat proportional CO estimates in the four swine datasets (see Fig. 5) than those obtained from alternative PAP waveform analysis techniques. The RMSNEs are in units of percent.

Fig. 5. Beat-to-beat CO estimated (and once calibrated) by applying the technique to the estimated AP waveforms (see Fig. 2) plotted against the gold standard reference aortic flow probe CO measurements for each of the four swine datasets (see Table I). The solid line in each plot is the identity line. See Table III for a complete quantitative summary of the beat-to-beat proportional CO estimation results.

Fig. 5 provides a visual illustration of the close agreement between the estimated and once calibrated beat-to-beat CO from the technique and the gold standard reference aortic flow probe measurements for each of the four swine datasets. Table III also provides a comparison of the evaluation results for the beat-to-beat proportional CO estimated by the new technique and via fitting the Windkessel model to the AP waveform estimates from our initial technique and the generalized transfer functions. The overall beat-to-beat CO RMSNE from the AP waveforms estimated by our initial technique was 36.3%, while the average overall beat-to-beat CO RMSNE from the waveforms estimated by the generalized transfer functions was 20.2%. Thus, the new technique increased the beat-to-beat CO estimation accuracy of the former technique by 63% and the latter technique by 36%.

Note that the beat-to-beat CO RMSNE obtained with our initial technique was even larger than the corresponding RMSNEs from the PAP waveforms. As discussed in Section V, this result was mainly due to outliers in the AP waveform estimation.

V. DISCUSSION

The present study represents a follow-up to our initial efforts in developing a patient- and time-specific technique for mathematically estimating the clinically more relevant AP waveform from less invasively measured PAP waveforms distorted by wave reflections [22]. In our initial study, we developed a technique to estimate the AP waveform from two or more PAP waveforms by employing MBSI rather than using the conventional generalized transfer function or any training data for that matter. In particular, the technique models the measured waveforms as individual outputs of coprime FIR channels driven by the common AP waveform input (see dark blocks in Fig. 1) and then analyzes the differences in the measured outputs, while invoking Poiseuille's law, so as to estimate the FIRs through the standard eigenvector method and ultimately reconstruct the common input via multichannel least squares deconvolution. We applied the technique to FAP and RAP waveforms measured from four swine over a wide hemodynamic range (but limited by a lack of bradycardia conditions for swine and a normal resting HR for dogs or humans), and our results showed superior agreement to simultaneously measured AP waveforms than did generalized transfer functions developed on a subset of the swine data. The main contributions of the present study are in: 1) introducing a new MBSI method to more accurately estimate the FIRs and therefore the AP waveform; 2) proposing to estimate beat-to-beat proportional CO by fitting a lumped parameter Windkessel model to the estimated AP waveform in which the wave distortion should be greatly attenuated (see Figs. 2 and 3), testing the resulting new technique for estimating both the AP waveform and beat-to-beat relative changes in CO, while comparing it to several alternative techniques, based on our four previous swine datasets, which also included gold standard reference aortic flow probe CO measurements (see Table I).

The basic idea of our new MBSI method is to represent the FIRs with more efficient basis functions than the standard impulse basis functions assumed by the eigenvector method. In this way, the number of parameters to be estimated will be reduced, thereby potentially resulting in a marked decrease in the precision component of the FIR estimation error. We specifically chose damped sinusoidal basis functions to compactly represent the FIRs [see (4)]. This choice was made empirically by observing that the "actual" FIRs (as defined before) in one of the swine datasets generally appeared as damped sinusoids. Thus, the bias component of the FIR estimation error may only increase modestly with this choice of basis functions. For simplicity, we assumed that: 1) the damping could be represented with a single parameter whose values was set according to the estimated channel order (wherein any error in this order may be partially compensated for by the remaining adjustable parameters); 2) the frequencies of the sinusoids could take on only discrete values according to the Fourier Series; and 3) each of the FIRs could be represented with the same number of basis functions. Even with these simplifications, the complexity in the least squares estimation of the parameters of the basis functions increases considerably with the number of basis functions. Thus, to render a real-time technique (with a 1 min delay), the parameter estimation was designed to only be optimal for a single basis function representation and suboptimal for a multiple basis function representation. We acknowledge that an orthogonal basis set could permit both optimal and practical parameter estimation. However, it turned out that only one basis function was needed to represent the FIRs in most of the 1 min intervals in the swine datasets. As a result, only 6.6 ± 1.9 (mean $\pm$ SD) parameters were estimated by the new method, whereas 9.0 ± 1.6 parameters were estimated by the standard eigenvector method. Thus, on average, the new method resulted in a 27% reduction in the parameters to be estimated. Another important advantage of the new method was that it accommodated larger FIR orders (by simply redefining the definition of an insignificant eigenvalue), which are more congruent with the "actual" FIRs (see Fig. 3). More specifically, the "actual" FIR order was generally about 15, while the average FIR order estimated by the new method was 10.0 ± 1.4. Note that such large FIR orders would have resulted in large estimation errors with the eigenvector method due to the limited frequency content of the AP waveform.

Our new technique was able to reliably estimate the AP waveform from the FAP and RAP waveforms in the four swine datasets with an overall total waveform RMSE of 3.5 mmHg (see Table II and Fig. 4). This error effectively represents a 59% reduction in wave distortion in the measured PAP waveforms. As a result, the technique was able to similarly reduce the RMSEs of SP and PP, which are perhaps the two most clinically significant parameters of the AP waveform. Significantly, the aforementioned overall total AP waveform RMSE represents a 24% improvement with respect to our initial technique and a 35% improvement with respect to generalized transfer functions. (Note that, while our techniques had the advantage of having access to one more PAP waveform, the generalized transfer functions had the advantage of "seeing" *a priori* data that were very similar to those utilized for its evaluation.) The former improvement is likely due to a reduction in the FIR estimation error variance, while the latter improvement is a result of the substantial variability in the FIRs undoubtedly arising from the various employed interventions and intersubject differences (see Fig. 3 and before). However, the precise mechanisms responsible for this variability are unclear. The work of Stergiopulos *et al.*, which provides a physical basis for the impulse responses in Fig. 1 (dark blocks), may represent a useful starting point for eventually elucidating these mechanisms [31].

As a result of greatly attenuating the wave distortion, our new technique was also able to reliably estimate beat-to-beat relative changes in CO in the four swine datasets with an overall RMSNE of 12.9% (see Table III and Fig. 5). This result is consistent with a compelling, previous study in which beat-to-beat proportional stroke volume was shown to be impressively estimated over a wide hemodynamic range by simply fitting the Windkessel model to the AP waveform (measured specifically from the descending thoracic aorta) [10]. Significantly, the aforementioned

overall beat-to-beat CO RMSNE of our new technique represents an improvement of $\geq 25\%$ with respect to fitting the Windkessel model directly to each of the PAP waveforms and to the AP waveforms estimated by our initial technique and the generalized transfer function. The beat-to-beat proportional CO estimates obtained from the AP waveforms estimated by our initial technique were the least accurate. This result is counter to intuition, because the initial technique was second best in terms of estimating the AP waveform with an overall total waveform RMSE of 4.6 mmHg. However, for about 10% of the analyzed data, the total waveform RMSE was over a third greater. While these "outliers" hardly increased the total waveform RMSE, they did increase the overall beat-to-beat CO RMSNE by over a factor of 2. (Note that this magnification of error is partly due to error introduced in the calibration of the beat-to-beat proportional CO estimates with the estimated mean CO value.) The outliers were likely caused by an insufficient number of frequency components in the AP waveform, as they have essentially been eliminated by the new technique.

As an interesting aside, the beat-to-beat CO RMSNE obtained by direct fitting of the Windkessel model to the FAP waveforms is nearly half that obtained by direct model fitting to the RAP waveforms (see Table III). This result may be due to the surprisingly accurate SEI estimates obtained from the FAP waveforms (see Table II) and their relatively smooth decay during diastole throughout the interventions. It is unclear whether these features hold in human FAP waveforms. On the other hand, the beat-to-beat CO RMSNE obtained from the RAP waveforms was reduced by nearly a third after the generalized transfer function was applied to these waveforms (see Table III). To our knowledge, this result of the generalized transfer function has not been shown before. However, application of the generalized transfer function to the FAP waveforms did not further reduce the already relatively low beat-to-beat CO RMSNE (see Table III) perhaps because the AP waveform estimates here were not as accurate (see Table II).

It would be insightful to obtain a further assessment of the performance of our new technique as a function of each intervention in the swine datasets. However, the durations of the interventions are uneven and, in some instances, small. Thus, it is difficult to draw definitive conclusions about technique performance under each specific intervention, but some general remarks can be made. In particular, the technique performed about the same for all of the interventions as compared to the overall performance of the technique, except for dobutamine. For this intervention, the total waveform RMSE was the largest (40% higher than the overall value). This result could be due to the FIRs of Fig. 1 (dark blocks) being less coprime and/or the AP waveform having fewer frequency components during dobutamine. For example, the FAP and RAP waveforms both appeared smooth (i.e., somewhat like sine waves) in this high chronotropic and vasodilated state presumably because of a reduced diastolic interval and reflection coefficient. On the other hand, the beat-to-beat CO RMSNE was the smallest for dobutamine (34% smaller than the overall value). This paradoxical result is simply due to the fact that the reference CO (i.e., the normalization value) was largest under the potent inotrope.

Our new technique (as well as our initial technique) was inspired by the recent efforts of McCombie *et al.*, who we believe were the first to apply MBSI in the field of hemodynamic monitoring [24]. These investigators specifically proposed a technique to estimate the morphology of the common aortic flow waveform input from multiple PAP waveform outputs and showed its feasibility in a single swine. Fig. 1 (all blocks) illustrates the single input, multioutput model upon which their technique was based. As can be seen from this model, the channels coupling the aortic flow waveform to each PAP waveform include common dynamics, namely the channel relating the aortic flow waveform to the AP waveform $[h_0(t)]$, and are therefore, not coprime. As a result, these investigators had to develop additional signal processing to estimate the common channel, which resulted in a considerably more complicated technique than conventional MBSI. Moreover, since their technique does not provide the scale factor of the estimated input, it cannot be utilized to monitor relative changes in CO. In contrast, our new technique first estimates the AP waveform input in which the coprime channel assumption is more tenable and the arbitrary input scale factor is conveniently determined through Poiseuille's law and then estimates beat-to-beat relative changes in CO by fitting the Windkessel model to the estimated waveform in which the wave distortion is greatly attenuated. We note that it is also possible to estimate the aortic flow waveform by applying the governing Windkessel model differential equation to the AP waveform estimated by our technique. However, the aortic flow waveform estimated in this manner did not closely agree with the reference aortic flow probe waveform in our swine datasets perhaps due to noise arising from implementing the required derivative operation.

Our new technique is related to a previous technique that we have developed for automated and less invasive monitoring of average relative changes in CO by long time interval analysis of a single PAP waveform [25]. The basic idea of this technique is to *circumvent* the highly complex wave reflections by effectively applying the Windkessel model to the waveform variations occurring over time scales greater than a cardiac cycle in which the distributed arterial tree appears to be lumped [2]. In contrast, the technique introduced herein analyzes the waveform over short time scales so as to essentially *remove* the wave reflections through MBSI and then apply the Windkessel model. The advantage of this technique is in providing AP waveform estimates as well as beat-to-beat rather than average proportional CO estimates. The obvious disadvantage is in requiring more than one waveform for analysis. (Note that the CO RMSNE that we reported earlier for our previous technique in [25] is not directly comparable to the results of this study, as the swine evaluation data utilized herein represent only a subset of the data employed in our earlier study.)

The new technique introduced herein permits both automated and less invasive central hemodynamic monitoring through estimation of the AP waveform and beat-to-beat relative changes in CO by mathematical analysis of multiple PAP waveforms. The technique may also possibly prove useful for local hemodynamic monitoring at each PAP waveform measurement site through the corresponding estimated FIR. The technique could

potentially be applied to noninvasive PAP waveforms measured from patients with various cardiovascular diseases (e.g., hypertension, heart failure, shock) in a number of different settings (e.g., emergency rooms, intensive care units, homes) as well as to invasive PAP waveforms obtained from critically ill patients. However, since only one PAP catheter is commonly inserted in these latter patients, application of the technique in this regard would be limited (e.g., to those patients with indications for CO measurements that are currently obtained with the more invasive and operator-required bolus thermodilution method [14]). Future experimental investigations of the technique with respect to invasive and noninvasive PAP waveforms measured from humans are needed to eventually realize these potential applications. In addition, subsequent quantitative studies aimed at developing error metrics (e.g., confidence intervals) on the estimates of the technique would be very useful for such applications.

REFERENCES

[1] A. M. Donald, *Blood Flow in Arteries*. London, U.K.: Arnold, 1960.
[2] A. Noordergraaf, *Circulatory System Dynamics*. New York: Academic, 1978.
[3] N. Westerhof, P. Sipkema, G. C. Van Den Bos, and G. Elzinga, "Forward and backward waves in the arterial system," *Cardiovasc. Res.*, vol. 6, pp. 648–656, 1972.
[4] D. S. Berger, J. K. Li, W. K. Laskey, and A. Noordergraaf, "Repeated reflection of waves in the systemic arterial system," *Amer. J. Physiol. Heart. Circ. Physiol.*, vol. 264, pp. 269–281, 1993.
[5] S. Soderstrom, G. Nyberg, M. F. O'Rourke, J. Sellgren, and J. Ponten, "Can a clinically useful aortic pressure wave be derived from a radial pressure wave?," *Br. J. Aneasth.*, vol. 88, pp. 481–488, 2002.
[6] C. H. Chen, E. Nevo, B. Fetics, P. H. Pak, F. C. Yin, W. L. Maughan, and D. A. Kass, "Estimation of central aortic pressure waveform by mathematical transformation of radial tonometry pressure. Validation of generalized transfer function," *Circulation*, vol. 95, pp. 1827–1836, 1997.
[7] M. E. Safar, J. Blacher, B. Pannier, A. P. Guerin, S. J. Marchais, P. Guyonvarc'h, and G. M. London, "Central pulse pressure and mortality in end-stage renal disease," *Hypertension*, vol. 38, pp. 735–738, 2002.
[8] T. K. Wadell, A. M. Dart, T. L. Medley, J. D. Cameron, and B. A. Kingwell, "Carotid pressure is a better predictor of coronary artery disease severity than brachial pressure," *Hypertension*, vol. 38, pp. 927–931, 2001.
[9] M. J. Bourgeois, B. K. Gilbert, D. E. Donald, and E. H. Wood, "Characteristics of aortic diastolic pressure decay with application to the continuous monitoring of changes in peripheral vascular resistance," *Circ. Res.*, vol. 35, pp. 56–66, 1974.
[10] M. J. Bourgeois, B. K. Gilbert, G. Bernuth, and E. H. Wood, "Continuous determination of beat-to-beat stroke volume from aortic pressure pulses in the dog," *Circ. Res.*, vol. 39, pp. 15–24, 1976.
[11] B. Fetics, E. Nevo, C. H. Chen, and D. A. Kass, "Parametric model derivation of transfer function for noninvasive estimation of aortic pressure by radial tonometry," *IEEE Trans. Biomed. Eng.*, vol. 46, no. 6, pp. 698–706, Jun. 1999.
[12] B. P. M. Imholz, W. Wieling, G. A. Montfrans, and K. H. Wesseling, "Fifteen years experience with finger arterial pressure monitoring: Assessment of technology," *Cardiovasc. Res.*, vol. 38, pp. 605–616, 1998.
[13] T. Kenner, "ABP and its measurement," *Basic Res. Cardiol.*, vol. 83, pp. 107–121, 1988.
[14] P. L. Marino, *The ICU Book*. Baltimore, MD: Williams & Wilkins, 1998.
[15] M. Karamanoglu, M. F. O'Rourke, A. P. Avolio, and R. P. Kelly, "An analysis of the relationship between central aortic and peripheral upper limb pressure waves in man," *Eur. Heart. J.*, vol. 14, pp. 160–167, 1993.
[16] M. Karamanoglu and M. P. Feneley, "On-line synthesis of the human ascending aortic pressure pulse from the finger pulse," *Hypertension*, vol. 30, pp. 1416–1424, 1997.
[17] M. Sugimachi, T. Shishido, K. Miyatake, and K. Sunagawa, "A new model-based method of reconstructing central aortic pressure from peripheral arterial pressure," *Jpn. J. Phsyiol.*, vol. 51, pp. 217–222, 2001.
[18] P. Segers, S. Carlier, A. Pasquet, S. I. Rabben, L. R. Hellevik, E. Remme, T. D. Backer, J. D. Sutter, J. D. Thomas, and P. Verdonck, "Individualizing the aorto-radial pressure transfer function: Feasibility of a model-based approach," *Amer. J. Physiol.*, vol. 279, pp. 542–549, 2000.
[19] M. Karamanoglu and M. P. Feneley, "Derivation of the ascending aortic-carotid pressure transfer function with an arterial model," *Amer. J. Physiol.*, vol. 271, pp. 2399–2404, 1996.
[20] P. Hallock and J. C. Benson, "Studies on the elastic properties of human isolated aorta," *Amer. J. Physiol.*, vol. 16, pp. 595–602, 1937.
[21] A. C. Guyton and J. E. Hall, *Textbook of Medical Physiology*. Philadelphia, PA: Saunders, 1996.
[22] G. Swamy, Q. Ling, L. Tongtong, and R. Mukkamala, "Blind identification of the aortic pressure waveform from multiple peripheral artery pressure waveforms," *Amer. J. Physiol. Heart. Circ. Physiol.*, to be published.
[23] G. Xu, H. Liu, L. Tong, and T. Kailath, "A least-squares approach to blind channel identification," *IEEE Trans. Signal Process.*, vol. 43, pp. 2982–2993, 1995.
[24] D. B. McCombie, A. T. Reisner, and H. H. Asada, "Laguerre-model blind system identification: Cardiovascular dynamics estimated from multiple peripheral circulatory signals," *IEEE Trans. Biomed. Eng.*, vol. 52, no. 11, pp. 1889–1901, Nov. 2005.
[25] L. Zhenwei and R. Mukkamala, "Continuous cardiac output monitoring in humans by invasive and noninvasive peripheral blood pressure waveform analysis," *J. Appl. Physiol.*, vol. 101, pp. 598–608, 2006.
[26] P. C. Hansen, *Rank Deficient and Discrete Ill-Posed Problems: Numerical Aspects of Linear Inversion*. Philadelphia, PA: SIAM, 1987.
[27] R. D. Berger, J. P. Saul, and R. J. Cohen, "Transfer function analysis of autonomic regulation I. Canine atrial rate response," *Amer. J. Physiol. Heart Circ. Physiol.*, vol. 256, pp. 142–152, 1989.
[28] R. Mukkamala, A. T. Reisner, H. M. Hojman, R. G. Mark, and R. J. Cohen, "Continuous cardiac output monitoring by peripheral blood pressure waveform analysis," *IEEE Trans. Biomed. Eng.*, vol. 53, no. 3, pp. 459–467, Mar. 2006.
[29] L. A. H. Critchley and J. A. J. H. Critchley, "A meta-analysis of studies using bias and precision statistics to compare cardiac output measurement techniques," *J. Clin. Monit. Comput.*, vol. 15, pp. 85–91, 1999.
[30] L. Ljung, *System Identification: Theory for the User*. Englewood Cliffs, NJ: Prentice-Hall, 1986.
[31] N. Stergiopulos, B. E. Westerhof, and N. Westerhof, "Physical basis of pressure transfer from periphery to aorta: A model-based study," *Amer. J. Physiol. Heart Circ. Physiol.*, vol. 274, pp. 1386–1392, 1998.

Gokul Swamy (S'06) received the B. Tech. and M. Tech. degrees in mechanical engineering from the Indian Institute of Technology (IIT), Chennai, India, in 2004. He is currently working toward the Ph.D. degree at the Physiologic Signal Processing and Modeling Laboratory, Department of Electrical and Computer Engineering, Michigan State University, East Lansing.

From 2004 to 2006, he was a Research Engineer in the Industrial Imaging and Modeling Laboratory, General Electric (GE), Global Research Centre, India.

Ramakrishna Mukkamala (M'02) received the B.S.E. degree in biomedical/electrical engineering from Duke University, Durham, NC, in 1993, and the S.M. and Ph.D. degrees in electrical engineering and computer science from the Massachusetts Institute of Technology (MIT), Cambridge, in 1995 and 2000, respectively.

From 2000 to 2002, he was a Postdoctoral Fellow/Research Engineer in the Harvard-MIT Division of Health Sciences and Technology. Since then, he has been on the faculty of the Department of Electrical and Computer Engineering, Michigan State University, East Lansing, where he is currently an Associate Professor. His current research interests include biomedical signal processing and identification, modeling of physiologic systems, and cardiovascular physiology.

Dr. Mukkamala is the recipient of an American Heart Association (AHA) Scientist Development Grant in 2005 and a National Science Foundation (NSF) CAREER Award in 2007.

An adaptive transfer function for deriving the aortic pressure waveform from a peripheral artery pressure waveform

Gokul Swamy,[1] Da Xu,[1] N. Bari Olivier,[2] and Ramakrishna Mukkamala[1]

[1]*Department of Electrical and Computer Engineering and* [2]*Department of Small Animal Clinical Sciences, Michigan State University, East Lansing, Michigan*

Swamy G, Xu D, Olivier NB, Mukkamala R. An adaptive transfer function for deriving the aortic pressure waveform from a peripheral artery pressure waveform. *Am J Physiol Heart Circ Physiol* 297: H1956–H1963, 2009. First published September 25, 2009; doi:10.1152/ajpheart.00155.2009.—We developed a new technique to mathematically transform a peripheral artery pressure (PAP) waveform distorted by wave reflections into the physiologically more relevant aortic pressure (AP) waveform. First, a transfer function relating PAP to AP is defined in terms of the unknown parameters of a parallel tube model of pressure and flow in the arterial tree. The parameters are then estimated from the measured PAP waveform along with a one-time measurement of the wave propagation delay time between the aorta and peripheral artery measurement site (which may be accomplished noninvasively) by exploiting preknowledge of aortic flow. Finally, the transfer function with its estimated parameters is applied to the measured waveform so as to derive the AP waveform. Thus, in contrast to the conventional generalized transfer function, the transfer function is able to adapt to the intersubject and temporal variability of the arterial tree. To demonstrate the feasibility of this adaptive transfer function technique, we performed experiments in 6 healthy dogs in which PAP and reference AP waveforms were simultaneously recorded during 12 different hemodynamic interventions. The AP waveforms derived by the technique showed agreement with the measured AP waveforms (overall total waveform, systolic pressure, and pulse pressure root mean square errors of 3.7, 4.3, and 3.4 mmHg, respectively) statistically superior to the unprocessed PAP waveforms (corresponding errors of 8.6, 17.1, and 20.3 mmHg) and the AP waveforms derived by two previously proposed transfer functions developed with a subset of the same canine data (corresponding errors of, on average, 5.0, 6.3, and 6.7 mmHg).

arterial tree; blood pressure; generalized transfer function; model; wave reflection

SINCE ITS INTRODUCTION by O'Rourke and coworkers in 1993 (3), the generalized transfer function has received attention for providing a convenient and safe means for monitoring central aortic pressure (AP) by mathematical transformation of a peripheral artery pressure (PAP) waveform. The basic premise of the transformation is that a single, universal transfer function exists that can faithfully relate the PAP waveform to the AP waveform of all individuals for all time. However, the transfer function linking PAP to AP would ideally be able to adapt to the intersubject and temporal variability of the arterial tree due to, for example, age-related arterial compliance differences, disease-induced peripheral resistance variations, baro- and thermoregulatory modulation of peripheral resistance in response to physiological perturbations, and therapeutic administration of vasoactive agents. To this end, Sugimachi

et al. (12) and Westerhof et al. (18) previously proposed a technique to partially adapt the transfer function by defining it through an arterial tube model with a personalized value for a model parameter reflecting the wave propagation delay time and population averages for the remaining parameters. We recently introduced (13, 14) perhaps the first entirely adaptive technique for mathematically deriving the AP waveform by exploiting the commonality in multiple PAP waveforms through the powerful multichannel blind system identification approach. However, the requirement of more than one PAP waveform is a practical disadvantage of this technique.

In this study, we conceived a fully adaptive technique for deriving the AP waveform from only one PAP waveform. The new technique similarly defines the transfer function relating PAP to AP through a parallel tube model of pressure and flow in the arterial tree but then estimates all of its parameters by capitalizing on preknowledge of aortic flow. The parameters are periodically reestimated for each subject so as to yield an adaptive transfer function (ATF). We performed canine experiments in order to test the ATF technique as well as compare it with previous transfer function techniques over a broad array of controlled and significant hemodynamic perturbations. A preliminary version of this study has been reported in abbreviated form (15).

METHODS

Adaptive transfer function technique. Figure 1 illustrates the major steps of the ATF technique. As shown in Fig. 1*A*, the arterial tree is modeled as a parallel arrangement of *m* uniform tubes in series with terminal loads. The *i*th tube represents the path between the aorta and the *i*th peripheral artery. Each tube is frictionless and therefore has constant characteristic impedance [$Z_{ci} = \sqrt{(l_i/c_i)}$, where l_i and c_i are the tube's total inertance and compliance] and allows waves to propagate with constant delay time from one end of the tube to the other [$T_{di} = \sqrt{(l_i c_i)}$]. Thus, consistent with Poiseuille's law, mean pressure is identical throughout the tubes. The *i*th terminal load signifies the arterial bed distal to the *i*th peripheral artery. Like the studies of Sugimachi et al. (12) and Westerhof et al. (18), each terminal load has a frequency-dependent impedance [$Z_i(\omega)$, where ω is frequency] characterized by two parameters that are dependent on the peripheral resistance and compliance (A_i and B_i, where $0 < A_i < B_i$) as well as the characteristic impedance of the corresponding tube (i.e., Z_{ci}). Thus the wave reflection coefficient at each terminal load is also frequency dependent {$\Gamma_i(\omega) = [Z_i(\omega) - Z_{ci}]/[Z_i(\omega) + Z_{ci}]$}.

Generally speaking, as shown for the *m*th tube and terminal load in Fig. 1*A*, forward pressure and flow waves [$p_f(t)$ and $q_f(t)$] propagate from left to right along each tube without distortion and are proportional to each other through the tube characteristic impedance. These waves are reflected in the opposite direction at the terminal load with relative magnitude and phase based on the frequency according to the wave reflection coefficient. The resulting backward pressure and flow waves [$p_b(t)$ and $q_b(t)$] likewise travel along the tube without distor-

Address for reprint requests and other correspondence: R. Mukkamala, Dept. of Electrical and Computer Engineering, Michigan State Univ., 2120 Engineering Bldg., East Lansing, MI 48824-1226 (e-mail: rama@egr.msu.edu).
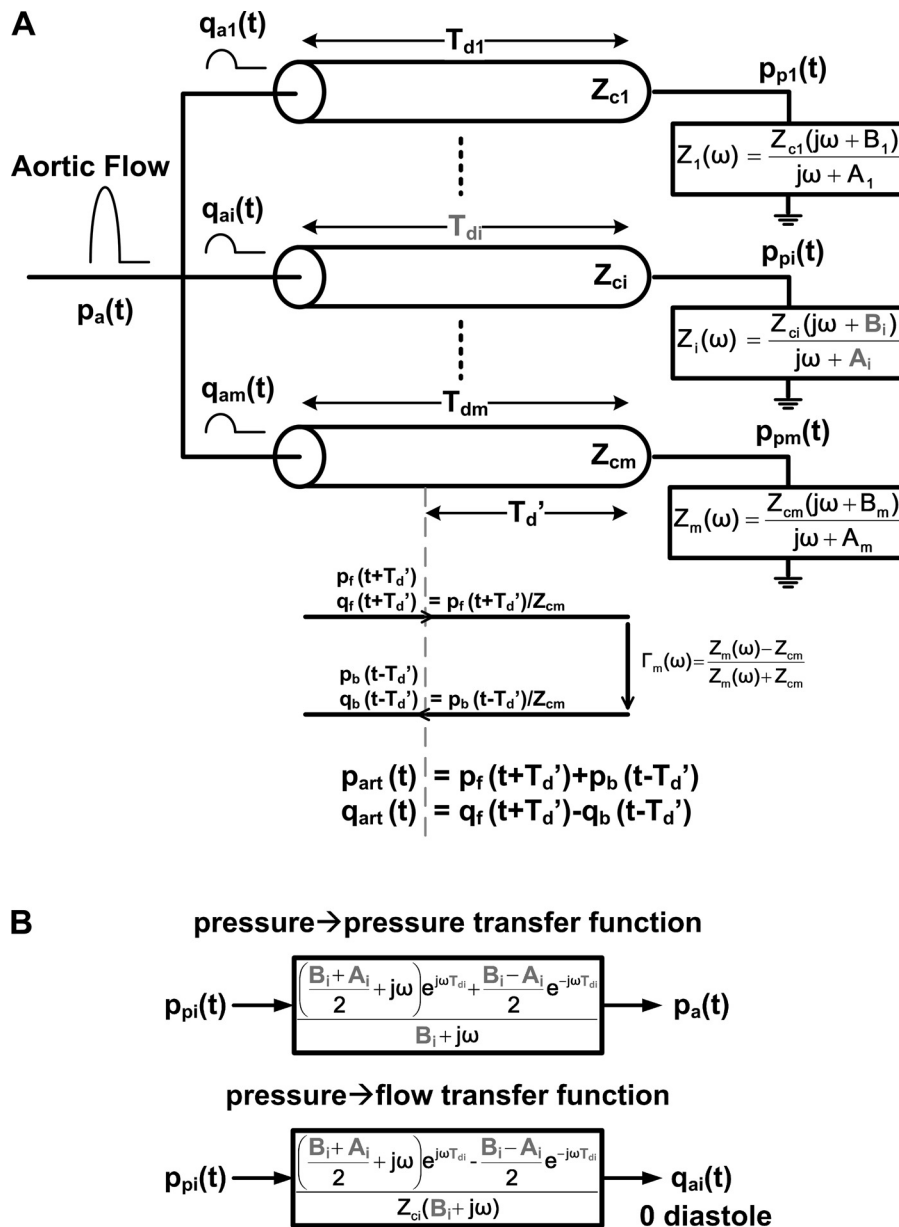
A

Fig. 1. Major steps of the adaptive transfer function (ATF) technique for deriving the aortic pressure (AP) waveform from a peripheral artery pressure (PAP) waveform. *A*: parallel tube model of pressure and flow in the arterial tree on which the technique is based. Each tube ($1 \leq i \leq m$) represents the path from the aorta to a peripheral artery, is characterized by constant characteristic impedance (Z_{ci}), and supports wave propagation from one end of the tube to the other with constant delay time (T_{di}). Each corresponding terminal load represents the arterial bed distal to the peripheral artery and has a frequency-dependent impedance [$Z_i(\omega)$, where ω is frequency] characterized by 2 parameters (A_i and B_i) that are dependent on the peripheral resistance and compliance and Z_{ci}. As shown for the *m*th tube and terminal load, forward pressure and flow waves [$p_f(t)$ and $q_f(t)$] propagate from *left* to *right* along each tube without distortion and are proportional to each other. These waves are reflected at the terminal load according to the wave reflection coefficient [$\Gamma_m(\omega)$]. The resulting backward pressure and flow waves [$p_b(t)$ and $q_b(t)$] likewise travel along the tube without distortion and are proportional to each other. The arterial pressure waveform [$p_{art}(t)$] {or flow waveform [$q_{art}(t)$]} at any point along a tube is therefore given in terms of $p_f(t)$ and $p_b(t)$ [or $q_f(t)$ and $q_b(t)$] shifted in time based on the wave propagation delay time between the point and the tube end (T_d'). *B*, *top*: transfer function relating a PAP waveform [$p_{pi}(t)$] to the AP waveform [$p_a(t)$] in terms of the unknown parameters of the model (in gray). *Bottom*: transfer function relating $p_{pi}(t)$ to the arterial flow waveform at the corresponding tube entrance [$q_{ai}(t)$] in terms of the same parameters. Since aortic flow is negligible during diastole, the common parameters are estimated by finding the pressure → flow transfer function, which when applied to the measured $p_{pi}(t)$, maps $q_{ai}(t)$ (scaled by Z_{ci}) to zero during this time interval. (To facilitate the parameter estimation, an initial noninvasive measurement of T_{di} is also obtained.) The pressure → pressure transfer function with the estimated parameters is then applied to $p_{pi}(t)$ so as to derive $p_a(t)$ in a fully adaptive manner. j, imaginary unit.

B

pressure→pressure transfer function

$$p_{pi}(t) \rightarrow \boxed{\frac{\left(\frac{B_i+A_i}{2}+j\omega\right)e^{j\omega T_{di}}+\frac{B_i-A_i}{2}e^{-j\omega T_{di}}}{B_i+j\omega}} \rightarrow p_a(t)$$

pressure→flow transfer function

$$p_{pi}(t) \rightarrow \boxed{\frac{\left(\frac{B_i+A_i}{2}+j\omega\right)e^{j\omega T_{di}}-\frac{B_i-A_i}{2}e^{-j\omega T_{di}}}{Z_{ci}(B_i+j\omega)}} \rightarrow q_{ai}(t)$$
0 diastole

tion and are proportional to each other. The actual arterial pressure waveform [$p_{art}(t)$] {or flow waveform [$q_{art}(t)$]} at any point along a tube may therefore be expressed as the sum (or difference) of the forward and backward pressure (or flow) waves appropriately shifted in time based on the wave propagation delay time between the point and the tube end (T_d'). In this way, the model is able to mimic the well-known progressive distortion that experimental arterial pressure and flow waveforms undergo with increasing distance from the aorta. Furthermore, from these expressions, a transfer function relating the arterial pressure or flow waveform at any point along a tube to the arterial pressure or flow waveform at any other point on the tube may be established in terms of the model parameters.

More specifically, according to the arterial tree model, a PAP waveform [$p_{pi}(t)$] is related to the AP waveform [$p_a(t)$] through the transfer function shown in Fig. 1*B*, *top* ("pressure → pressure transfer function"), with unknown model parameters (see detailed derivation in Ref. 11). Thus this transfer function may be applied to a measured PAP waveform so as to derive the AP waveform, if its parameters, namely T_{di}, A_i, and B_i, could be determined.

To this end, T_{di}, the wave propagation delay time between the aorta and peripheral artery measurement site, is first measured noninvasively (see DISCUSSION). Only one T_{di} measurement is made for a subject during a period of up to weeks or perhaps even months, as this parameter may not greatly vary over such a time period. That is, although it is well appreciated that T_{di} and arterial pressure have an inverse relationship, large arterial pressure changes yield only small changes in T_{di} (see, e.g., Ref. 8). It should be further noted that changes in vasomotor tone should not markedly perturb T_{di}, because the total compliance between the ascending aorta and a peripheral artery is mainly due to the aorta and other large arteries in which smooth muscle is relatively sparse (5).

Thereafter, the three parameters are determined from each 15-s segment of the measured PAP waveform and initial T_{di} value by exploiting the fact that aortic flow is negligible during each diastolic interval because of aortic valve closure (provided that aortic regurgitation is absent). Thus, as indicated in Fig. 1*A*, the arterial flow at each tube entrance in the arterial tree model ("arterial entry flow") may likewise be small during these time intervals. In particular, according

to this model, the PAP waveform is related to the arterial entry flow waveform to the corresponding peripheral artery [$q_{ai}(t)$] through the transfer function shown in Fig. 1B, *bottom* ("pressure $\rightarrow$ flow transfer function") with the same unknown model parameters as the pressure $\rightarrow$ pressure transfer function. The common parameters are then estimated by finding the pressure $\rightarrow$ flow transfer function, which when applied to the PAP waveform segment, minimizes the energy (sum of squares) of the arterial entry flow waveform (scaled by Z_{ci}) output over its diastolic intervals. In other words, as indicated in Fig. 1B, *bottom*, the parameters are selected so as to map the PAP waveform to an arterial entry flow of zero during diastole.

Figure 2 illustrates the detailed steps of the technique through a flowchart. First, since the mean or DC value of $p_a(t)$ is already known [i.e., approximated as the corresponding value of $p_{pi}(t)$ due to Poi-

seuille's law], the DC value of $p_{pi}(t)$ is removed in order to focus the mapping on the unknown zero-mean or AC components. AC $q_{ai}(t)$ is then calculated to within a $1/Z_{ci}$ scale factor by applying the pressure $\rightarrow$ flow transfer function to AC $p_{pi}(t)$ for a set of A_i and B_i values over a physiological range with the T_{di} value as measured. Next, the end of each diastolic interval in each candidate AC proportional $q_{ai}(t)$ is determined by identifying the minimum preceding the peak amplitude of a cardiac cycle, and the start of each corresponding diastolic interval is approximated based on Malik's formula (4) relating the cardiac cycle length to the systolic interval length. Then the values of A_i and B_i are selected that provide the minimum variance of AC proportional $q_{ai}(t)$ over its diastolic intervals among those values yielding physiologically reasonable pressure and flow waveforms [i.e., AC proportional $q_{ai}(t)$ exhibits an undershoot during diastole as
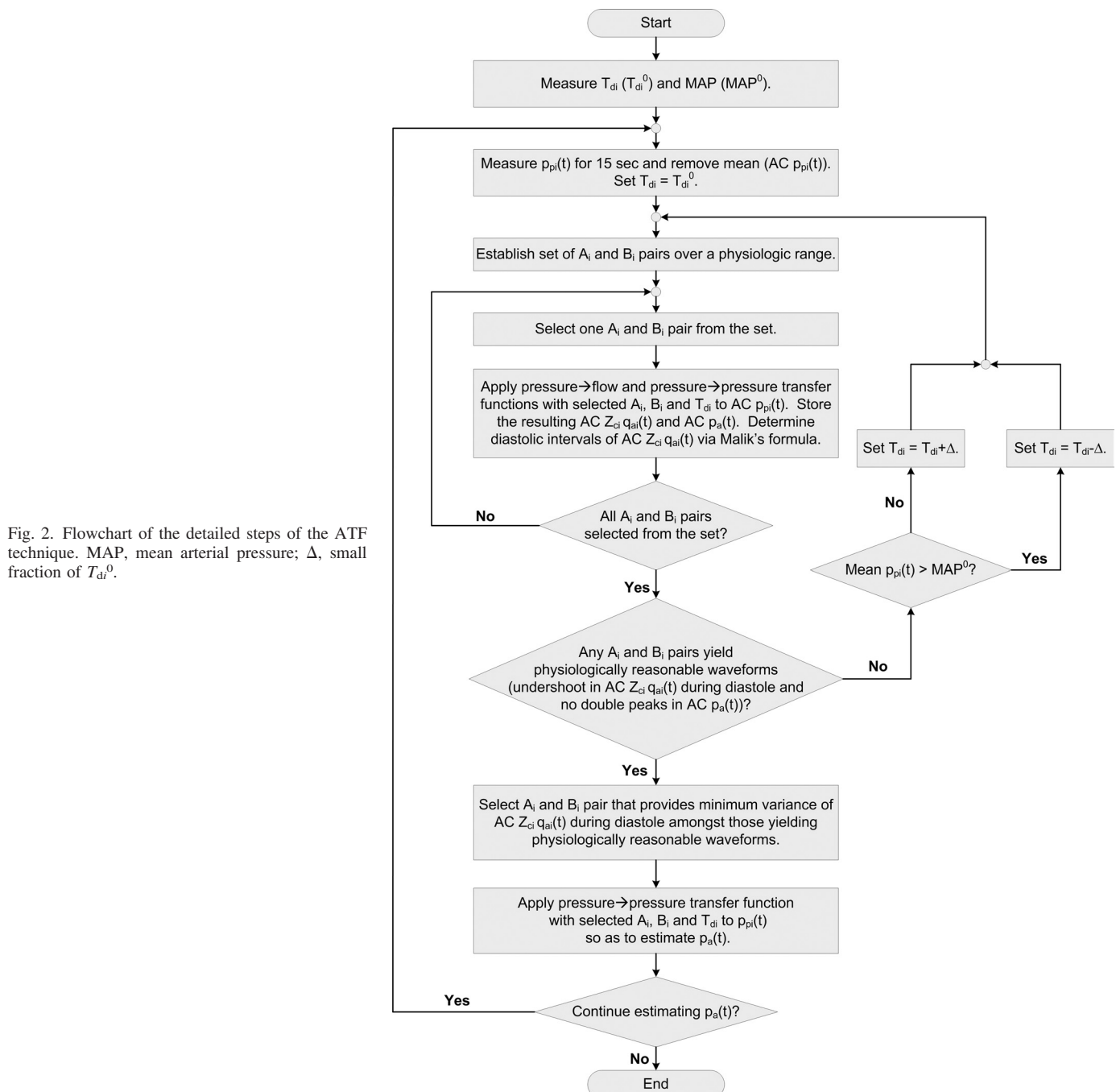

Fig. 2. Flowchart of the detailed steps of the ATF technique. MAP, mean arterial pressure; Δ, small fraction of T_{di}^0.

typically seen in experimental waveforms (6), and $p_a(t)$, computed as described below, does not reveal double peaks]. In the event that none of the A_i and B_i values in the set results in physiologically reasonable waveforms, T_{di} is successively incremented when mean pressure decreases relative to the T_{di} measurement period or decremented when mean pressure increases relative to this period until the criterion is satisfied. Finally, the pressure → pressure transfer function, with the selected values for A_i, B_i, and T_{di}, is applied to $p_{pi}(t)$ (including its DC value) so as to derive $p_a(t)$. [Note that the DC value of proportional $q_{ai}(t)$ may be determined by shifting the diastolic intervals of the AC waveform to zero amplitude.]

Data collection. Data were collected from six healthy adult beagles (10–12 kg) under an experimental protocol approved by the Michigan State University All-University Committee on Animal Use and Care. For each dog, general anesthesia was induced by an intravenous injection of propofol (2.2–6.6 mg/kg) and maintained with an inhaled mixture of oxygen and isoflurane (1.5–2.5%). A micromanometer-tipped catheter (Millar Instruments, Houston, TX) was placed in a femoral artery for the PAP waveform for analysis. A similar catheter was inserted in the opposite femoral artery or a carotid artery and positioned in the ascending aorta for the reference AP waveform. A catheter was also placed in a cephalic vein for drug and isotonic fluid administration, and electrodes were positioned for standard ECG measurements. In the fifth dog, a bipolar electrode catheter (EP Technologies, Boston Scientific, Sunnyvale, CA) was inserted into a jugular vein and advanced to the right atrium for high-rate pacing with an external pulse generator (Medtronic, Minneapolis, MN). In the sixth dog, a quadrapolar ablation catheter (EP Technologies) was inserted into a femoral vein and positioned to ablate the atrioventricular (AV) node and to then apply bipolar electrical stimulation to the His bundle as previously described (10) for low-rate pacing with the external pulse generator. (Additional instrumentation was also installed in the fifth and sixth dogs to address different specific aims.) Placement of all central catheters was accomplished by guidance with a single-plane lateral projection fluoroscopic imaging unit (GE, Milwaukee, WI). The analog transducer outputs were interfaced to a personal computer via an analog-to-digital conversion system (DataQ Instruments, Akron, OH). The arterial pressure waveforms and ECG measurements were recorded at a sampling rate of 1,000 Hz during a baseline period and after infusions of phenylephrine and nitroglycerin in the first dog; dobutamine and esmolol in the second dog; norepinephrine and xylazine in the third dog; saline and progressive hemorrhage in the fourth dog; verapamil and high-rate pacing in the fifth dog; and vasopressin (before AV node ablation) and low-rate pacing in the sixth dog. Several infusion and pacing rates were employed, followed by recovery periods.

Data analysis. The ATF technique was applied to 260 min of recorded PAP waveforms resampled to 250 Hz, with T_{di} measured for each dog as the time interval between the onsets of upstroke of the AP and PAP waveforms during the initial beats of the baseline period. The resulting derived AP waveforms were low-pass filtered with a cutoff frequency of 15 Hz as previously justified (2) and then quantitatively evaluated against the (unfiltered) reference AP waveforms in terms of the sample-to-sample (total waveform, TW), beat-to-beat systolic pressure (SP), and beat-to-beat pulse pressure (PP) root mean square errors (RMSEs) for each experimental condition and overall. The unprocessed PAP waveforms were likewise assessed with respect to the reference AP waveforms after time aligning the two waveforms to eliminate error due merely to the wave propagation delay.

For further comparison, AP waveforms were also derived by an autoregressive exogenous input-based generalized transfer function (GTF$_{ARX}$) technique (2) (which was shown to be the most accurate among 3 generalized transfer function techniques) and the tube model-based partially adaptive transfer function (PATF$_{tube}$) technique (12, 18) (i.e., the transfer function shown in Fig. 1B, *top*, with T_{di} measured for each dog as described above and the same values for the A_i and B_i parameters for all dogs). More specifically, the two previous transfer

functions were established by averaging over a set of transfer functions computed from each 15-s segment of the PAP and AP waveforms of one of the dogs and then applied to the PAP waveforms of the remaining dogs (see DISCUSSION). The resulting derived AP waveforms were then similarly low-pass filtered and evaluated. This procedure was repeated for each dog in order to avoid any bias, and the results were averaged.

Finally, the TW, SP, and PP RMSEs in the AP waveforms derived by the ATF technique were statistically compared with the corresponding errors in the time-aligned PAP waveforms and the AP waveforms derived by the GTF$_{ARX}$ and PATF$_{tube}$ techniques over all the experimental conditions. In particular, paired t-tests were performed after log transformation to make the data more normally distributed. A P value of <0.05 was considered statistically significant.

RESULTS

Table 1 illustrates the AP and heart rate (HR) levels during each of the experimental conditions. Table 2 shows the TW, SP, and PP RMSEs in the PAP waveforms after time alignment and the AP waveforms derived by the new ATF technique as well as the previous GTF$_{ARX}$ and PATF$_{tube}$ techniques for each condition and overall along with P values indicating statistically significant differences. Figure 3 provides visual examples of the measured AP and PAP waveform segments and the corresponding derived AP waveform segments during five different conditions.

AP and HR levels (means ± SD) varied widely over the various experimental conditions. Mean arterial pressure (MAP) ranged from 62 ± 3 to 134 ± 15 mmHg, SP from 78 ± 8 to 162 ± 22 mmHg, PP from 18 ± 1 to 55 ± 11 mmHg, and HR from 73 ± 20 to 197 ± 16 beats/min.

On the whole, the PAP waveforms were markedly different from the reference AP waveforms, especially in terms of SP and PP. The overall TW, SP, and PP RMSEs in the time-aligned waveforms were 8.6, 17.1, and 20.3 mmHg, respectively. The level of discrepancy between the unprocessed PAP and reference AP waveforms likewise varied over the different experimental conditions. The TW, SP, and PP RMSEs were by far the smallest during the nitroglycerin condition (3.2, 2.0, and 2.2 mmHg) and largest during the norepinephrine condition (14.0, 30.9, and 35.2 mmHg).

All three techniques were able to derive the AP waveform with considerably greater accuracy than merely time aligning

Table 1. *AP and HR levels*

Condition	MAP, mmHg	SP, mmHg	PP, mmHg	HR, bpm
Baseline	88±20	104±24	34±9	127±7
Phenylephrine	132±14	158±19	49±9	98±9
Nitroglycerin	62±3	79±3	27±1	96±1
Dobutamine	89±2	116±3	51±2	172±8
Esmolol	71±3	85±3	24±0	113±1
Norepinephrine	134±15	162±22	55±11	117±13
Xylazine	65±8	78±8	25±1	100±10
Saline	98±1	119±1	45±1	137±1
Hemorrhage	66±5	80±5	25±1	105±4
Verapamil	74±10	90±11	33±3	115±10
High-rate pacing	75±3	85±2	18±1	197±16
Vasopressin	94±15	108±16	28±3	103±4
Low-rate pacing	73±7	95±5	42±6	73±20

Quantities are expressed as means ± SD. AP, aortic pressure; MAP, mean arterial pressure; SP, systolic pressure; PP, pulse pressure; HR, heart rate; bpm, beats per minute.

Table 2. *Peripheral artery pressure and derived AP waveform errors*

Condition	Time-Aligned PAP			ATF			GTF$_{ARX}$			PATF$_{tube}$		
	TW	SP	PP	TW	SP	PP	TW	SP	PP	TW	SP	PP
Baseline	11.1	18.8	22.2	6.1	9.4	6.0	5.1	5.9	4.9	5.6	8.8	7.4
Phenylephrine	10.7	19.9	22.9	3.0	2.8	2.4	5.4	6.5	6.0	8.5	4.9	4.3
Nitroglycerin	3.2	2.0	2.2	3.9	7.2	7.0	5.3	9.4	8.1	4.3	7.9	7.7
Dobutamine	7.4	13.9	17.8	4.9	2.8	2.6	8.2	12.3	14.9	6.7	4.1	6.3
Esmolol	5.2	12.0	11.4	2.2	3.8	1.8	2.8	2.2	3.2	2.4	3.7	2.4
Norepinephrine	14.0	30.9	35.2	3.9	5.4	4.7	7.3	6.1	5.9	9.1	11.2	11.2
Xylazine	6.1	13.2	13.9	2.5	4.0	2.9	3.2	2.7	2.1	2.9	4.8	4.3
Saline	11.6	21.0	25.1	4.1	1.2	0.7	4.8	4.7	5.5	4.7	6.7	7.4
Hemorrhage	6.5	15.5	16.1	2.1	2.7	1.0	2.7	3.7	3.1	2.8	6.4	5.3
Verapamil	8.0	15.0	16.7	2.6	2.8	1.8	2.6	2.5	3.1	3.3	4.8	4.7
High-rate Pacing	7.7	13.3	21.5	3.6	1.7	2.7	2.6	2.7	4.8	4.0	6.4	7.6
Vasopressin	7.4	16.3	16.9	3.2	3.3	1.9	3.6	3.0	2.4	2.7	4.2	4.6
Low-rate Pacing	6.7	15.2	17.1	2.7	1.8	2.6	3.0	2.2	2.0	2.4	4.0	4.0
Overall	8.6	17.1	20.3	3.7	4.3	3.4	4.8	6.1	6.7	5.1	6.5	6.6
P value	6.5e-6	1.5e-4	3.7e-5				0.02	NS	0.02	0.04	0.002	4.9e-4

Quantities are root mean square errors (RMSEs; mmHg) with respect to the measured AP waveforms. *P* values indicate statistically significant differences in RMSE over all the conditions with respect to the new adaptive transfer function (ATF) technique. The previous autoregressive exogenous input-based generalized transfer function (GTF$_{ARX}$) and tube model-based partially adaptive transfer function (PATF$_{tube}$) techniques were developed with a subset of the canine data and tested on the remaining data. TW, total waveform (i.e., sample to sample); NS, not significant.

the PAP waveform. The TW, SP, and PP RMSEs in the derived waveforms were markedly reduced relative to those in the unprocessed waveforms for almost all of the individual experimental conditions. The notable exception was the nitroglycerin condition, in which processing of the PAP waveforms by each technique actually increased the RMSEs, because these waveforms were already in close agreement with the AP waveforms. In addition, the GTF$_{ARX}$ technique provided no or only modest reductions in the RMSEs during the dobutamine condition. As a result, the TW, SP, and PP RMSE reductions achieved by the three techniques easily reached statistical significance over all conditions (*P* values not shown for the GTF$_{ARX}$ and PATF$_{tube}$ techniques).

The ATF technique was the most accurate over all the experimental conditions. The overall TW, SP, and PP RMSEs in the AP waveforms derived by this technique were 3.7, 4.3, and 3.4 mmHg, respectively. The corresponding RMSEs of the GTF$_{ARX}$ and PATF$_{tube}$ techniques were similar to each other and, on average, 5.0, 6.3, and 6.7 mmHg. The TW, SP, and PP RMSEs of the ATF technique were statistically smaller over all the conditions than their counterparts for both previous techniques, except for the SP error of the GTF$_{ARX}$ technique.

The ATF technique attained its largest improvements in accuracy over the two previous techniques during the conditions of dobutamine (reduction in TW, SP, and PP RMSEs by 2.6, 5.4, and 8.0 mmHg, respectively, on average), norepinephrine (4.3, 3.3, and 3.9 mmHg), saline (0.7, 4.5, and 5.8 mmHg), and phenylephrine (4.0, 2.9, and 2.8 mmHg). However, this technique was less accurate than the GTF$_{ARX}$ technique during the baseline condition (increase in TW, SP, and PP RMSEs by 1.0, 3.5, and 1.1 mmHg, respectively) and the xylazine condition to a small extent (−0.7, 1.3, and 0.8 mmHg).

DISCUSSION

Pressure waveforms simultaneously measured from the central aorta and a peripheral artery show striking differences in both morphology and level (see, e.g., Fig. 3). Most importantly from a clinical point of view, peripherally measured SP and PP are generally larger than their centrally measured counterparts. This counterintuitive amplification of the pressure waveform with increasing distance from the central aorta arises from wave reflections in the arterial tree. It is therefore the pressure in the central aorta that truly indicates cardiac afterload and myocardial perfusion. Perhaps as a consequence, previous studies have shown that centrally measured arterial pressure can offer clinical information superior to more distally measured pressure (9, 17). Even so, the PAP waveform is much more commonly measured in practice because of the relative ease and safety of its measurement.

In this study, we developed a technique to mathematically transform a PAP waveform so as to obtain the AP waveform conveniently and safely. The technique was inspired by the following investigators: *1*) Stergiopulos et al. (11), who proposed a physical basis for the transfer function relating PAP to AP through an arterial tube model; *2*) Sugimachi et al. (12) and Westerhof et al. (18), who employed the tube model to establish a partially adaptive transfer function for deriving the AP waveform; and *3*) Cohen, who thought to compute the total aortic flow waveform from a PAP waveform by finding a black box, rather than physical model-based, transfer function that maps the PAP waveform to zero during diastole (personal communication in 2000 and now described in Ref. 1 as a result of this study). Our technique similarly defines the transfer function relating PAP to AP through a tube model and then estimates the unknown model parameters from the PAP waveform as well as a one-time noninvasive measurement of the wave propagation delay time between the aorta and peripheral artery measurement site by likewise exploiting the fact that aortic flow is negligible during diastole (see Figs. 1 and 2). In this way, in contrast to the conventional generalized transfer function and perhaps all other previous techniques for mathematically deriving the AP waveform, the new technique is able to fully adapt to the intersubject and temporal variability of the arterial tree with only a single PAP waveform available for analysis.
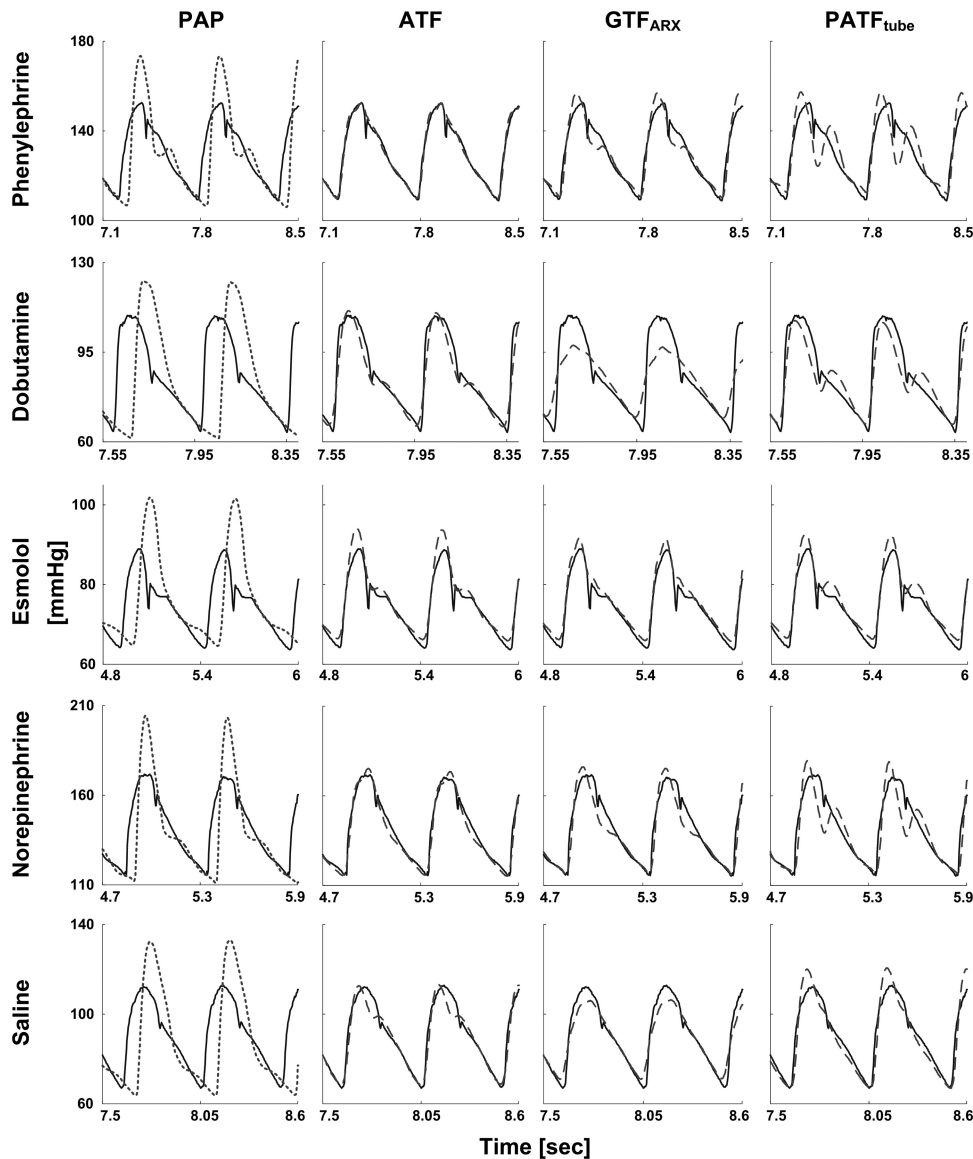
Fig. 3. Example segments of the reference AP (solid line), measured PAP (dotted line), and derived AP (dashed line) waveforms by the new ATF technique and previous autoregressive exogenous input-based generalized transfer function (GTF$_{ARX}$) and tube model-based partially adaptive transfer function (PATF$_{tube}$) techniques during the 5 different conditions.

To demonstrate feasibility of the new ATF technique, we measured a PAP waveform from a femoral artery and the reference AP waveform from the ascending aorta of 6 healthy beagles of similar size during 12 different hemodynamic interventions (see Table 1). Thus, unlike most previous related efforts, we were able to assess the efficacy of the technique over a diverse set of significant perturbations of known effect. On the other hand, our measurements did not allow us to investigate the technique in the context of a varying population of subjects.

Our results (see Table 2 and Fig. 3) showed that the overall TW, SP, and PP RMSEs in the AP waveforms derived by the ATF technique were, respectively, 3.7, 4.3, and 3.4 mmHg. These errors effectively amounted to 75% reduction in wave distortion in the PAP waveforms. The corresponding RMSEs of the GTF$_{ARX}$ and PATF$_{tube}$ techniques were, on average, 34%, 47%, and 96% higher than the new technique. Indeed, the RMSE reductions achieved by the new technique were, in general, statistically significant over all of the experimental conditions. It is important to recognize that, unlike the previous

techniques, the ATF technique was not given crucial information, namely training data comprising a subset of the canine AP waveforms. Even with this handicap, the new technique was able to outperform the previous techniques.

The improved accuracy afforded by the ATF technique over the previous techniques was especially pronounced during the dobutamine, norepinephrine, saline, and phenylephrine conditions. During the first condition, the transfer function relating PAP to AP was altered to a relatively large degree. Evidently, intense vasodilation occurred during this positive cardiac inotropic condition, as centrally measured PP and HR markedly increased from the baseline condition without a change in MAP (see Table 1). During the latter three conditions, the ATF technique was comparatively more effective. On the other hand, this technique was ineffective during the nitroglycerin condition, although better than the previous techniques, and relatively less efficacious during the baseline condition. However, it should be noted that a statistical assessment of the relative accuracy of the techniques during the individual conditions was not feasible, because we employed two different

interventions in each dog. Thus our canine experimental design represents a study limitation.

To obtain the above results, we developed the GTF_{ARX} and $PATF_{tube}$ techniques using one-sixth of the canine data and tested them on the remaining data. Even under the ideal scenario for the previous techniques in which all of the data were utilized for both development and testing, these techniques were still not able to derive the AP waveform with greater accuracy than the ATF technique. However, as indicated in Table 3, the gap between the overall TW, SP, and PP RMSEs of the two previous techniques and the new technique were reduced from 34%, 47%, and 96% to 15%, 33%, and 74%, respectively, and over half of the statistically significant RMSE differences were lost. It should be noted that, in contrast to this ideal scenario, a generalized transfer function does not represent a perfect estimate of the population average transfer function in practice. The reason stems from the high level of invasiveness needed to obtain the requisite AP waveforms, which limits the number of subjects (usually to <100) and the class of subjects (usually to cardiac catheterization patients) available for transfer function derivation. Thus a real-world generalized transfer function suffers from nonnegligible standard error and population bias. We therefore believe that the results of comparing the ATF technique to the previous techniques as developed with one-sixth of the data better indicate, and perhaps even underestimate, what the relative accuracy of the techniques would be when applied to the diverse population of patients seen in clinical practice.

The parallel tube model on which the ATF technique is based (see Fig. 1A) neglects arterial tapering and stiffening, as the dominant wave reflection sites appear to be at the arterial terminations because of their high resistance (6, 19). The model also ignores the inertance of the distal arterial bed, since it is well appreciated that inertial work is small compared with viscous work in the high-pressure systemic arterial tree. Nevertheless, such modeling inaccuracies as well as imperfect parameter estimation represent the sources of error of the technique. To determine the relative contributions of the modeling and parameter estimation errors to the derived AP waveform error, we first found the "actual" parameter values, using the measured PAP and AP waveforms. We specifically established the actual parameter values for each individual segment of analysis by finding the pressure → pressure transfer function (see Fig. 1B, top), which when applied to the PAP waveform segment, best fits the measured AP waveform segment in the least-squares sense. We then applied the transfer function with the actual parameter values to the PAP waveform segment so as to derive the AP waveform segment. The overall TW RMSE in the derived AP waveforms, which represents the lower bound for the ATF technique due only to its modeling error,

Table 3. *Derived AP waveform errors for GTF_{ARX} and PATF_{tube} techniques in which all canine data were utilized for both development and testing*

	GTF$_{ARX}$			PATF$_{tube}$		
	TW	SP	PP	TW	SP	PP
Overall	3.7	5.8	6.6	4.8	5.6	5.2
P value	NS	NS	NS	NS	0.03	0.02

Values are RMSEs (mmHg). See Table 2 for meaning of quantities.

was 2.8 mmHg. Thus most (76%) of the corresponding RMSE of the ATF technique was due to modeling inaccuracies. As a related comment, it should be noted that the GTF_{ARX} and $PATF_{tube}$ techniques derived the AP waveform with similar average overall RMSEs (see, e.g., Table 2), perhaps as a result of the modeling error offsetting the partial individualization of the latter tube model-based technique.

While modeling inaccuracies represent a cost of the new technique, it should be noted that the benefit of basing the technique on a model extends beyond the realization of a fully adaptive transfer function. In particular, unlike conventional black box techniques such as the GTF_{ARX} technique, the parameters of the model on which the ATF technique is based carry physiological meaning (e.g., peripheral resistance and compliance) and may be utilized to calculate additional physiological quantities (e.g., wave reflection coefficient) (12, 18). Thus, by periodically reestimating these parameters, our model-based technique may offer expanded physiological monitoring capabilities over the conventional techniques.

For this demonstration study, we obtained the single measurement of the wave propagation delay time between the aorta and the peripheral artery measurement site (T_{di}) for each dog by using a few beats of the measured AP and PAP waveforms during the baseline period. In practice, T_{di} may be measured noninvasively by, for example, placing a handheld tonometer on the carotid artery and determining the time between the onsets of upstroke of the waveform that it measures and the recorded PAP waveform (12). For long-term monitoring applications, such an operator-required measurement would likely need to be made periodically (e.g., every few weeks). Alternatively, T_{di} may be continuously approximated through, for example, a simultaneously recorded ECG or phonocardiogram.

It is claimed that a generalized transfer function is justified when applied to a PAP waveform from the upper limb but not the lower limb (7). Despite this claim, we measured the PAP waveform from a femoral artery in this study because of experimental convenience, the observation that this waveform appears significantly different from the AP waveform (see Fig. 3), and the fact that this peripheral artery is commonly cannulated in clinical practice. Our study may therefore be among the first, if not the first, studies demonstrating the feasibility of mathematically transforming a PAP waveform from a lower limb to the AP waveform. Because of its ability to adapt to arterial tree changes, our technique should be applicable to pressure waveforms obtained from any peripheral artery including the readily accessible radial artery (but excluding distal arteries in the coronary circulation for which arterial entry flow is significant during diastole). However, while we believe that our technique will also reveal improved accuracy over generalized transfer function techniques when applied to a PAP waveform from the upper limb, we do acknowledge the possibility that the overall difference in accuracy may not be as significant.

In summary, we have developed perhaps the first fully adaptive technique for mathematically deriving the AP waveform from one PAP waveform and have demonstrated its feasibility in animals over a wide range of physiological conditions. In the future, it would be worthwhile to explore refinements to the parallel tube model on which the technique is based (e.g., the inclusion of additional parameters to more

accurately represent the terminal loads) as well as continuous approximation of the wave propagation delay time from simultaneously recorded noninvasive measurements. In addition, further testing of the technique is needed to establish its relative efficacy during different experimental conditions and to assess its applicability to PAP waveforms measured noninvasively, from the upper limb, and from humans. Such testing should involve side-by-side comparisons with the previous transfer function techniques in terms of not only AP waveform derivation accuracy but also cardiovascular risk stratification capabilities (see, e.g., Refs. 9, 17) in order to convincingly demonstrate the added value of the new technique. If such follow-up studies prove successful, then the technique could be employed for more precise arterial pressure monitoring, titration of therapy, and cardiovascular risk stratification in intensive care and surgical units in which PAP catheters are routinely inserted and other clinical environments such as outpatient clinics and home in conjunction with noninvasive PAP devices. Finally, subsequent combination of the technique with an AP waveform analysis technique that we have also recently developed (16) may ultimately permit continuous monitoring of cardiac output and left ventricular ejection fraction in addition to AP from just a single PAP waveform.

REFERENCES

1. **Cohen RJ.** *Flow Estimation*. Cambridge, MA: Massachusetts Institute of Technology, Case No. 13176, 2008.
2. **Fetics B, Nevo C, Chen H, Kass DA.** Parametric model derivation of transfer function for noninvasive estimation of aortic pressure by radial tonometry. *IEEE Trans Biomed Eng* 46: 698–706, 1999.
3. **Karamanoglu M, O'Rourke MF, Avolio AP, Kelly RP.** An analysis of the relationship between central aortic and peripheral upper limb pressure waves in man. *Eur Heart J* 14: 160–167, 1993.
4. **Malik M.** If Dr Bazett had a computer. *Pacing Clin Electrophysiol* 19: 1635–1639, 1996.
5. **McDonald DA.** Regional pulse-wave velocity in the arterial tree. *J Appl Physiol* 24: 73–78, 1968.
6. **McDonald DA.** *Blood Flow in the Arteries*. London: Edward Arnold, 1974.
7. **O'Rourke MF, Avolio AP.** Arterial transfer functions: background, applications and reservations. *J Hypertens* 26: 8–10, 2008.
8. **Pruett JD, Bourland JD, Geddes LA.** Measurement of pulse-wave velocity using a beat-sampling technique. *Ann Biomed Eng* 16: 341–347, 1988.
9. **Safar ME, Blacher J, Pannier B, Guerin AP, Marchais SJ, Guyonvarc'h PM, London GM.** Central pulse pressure and mortality in end-stage renal disease. *Hypertension* 39: 735–738, 2009.
10. **Sanders R, Bailie M, Olivier NB.** Stability of ventricular depolarization in conscious dogs with chronic atrioventricular dissociation and his-bundle pacing. *Pacing Clin Electrophysiol* 27: 1475–1483, 2004.
11. **Stergiopulos N, Westerhof BE, Westerhof N.** Physical basis of pressure transfer from periphery to aorta: a model-based study. *Am J Physiol Heart Circ Physiol* 274: H1386–H1392, 1998.
12. **Sugimachi M, Shishido T, Miyatake K, Sunagawa K.** A new model-based method of reconstructing central aortic pressure from peripheral arterial pressure. *Jpn J Physiol* 51: 217–222, 2001.
13. **Swamy G, Ling Q, Li T, Mukkamala R.** Blind identification of the aortic pressure waveform from multiple peripheral artery pressure waveforms. *Am J Physiol Heart Circ Physiol* 292: H2257–H2264, 2007.
14. **Swamy G, Mukkamala R.** Estimation of the aortic pressure waveform and beat-to-beat cardiac output from multiple peripheral artery pressure waveforms. *IEEE Trans Biomed Eng* 55: 1521–1529, 2008.
15. **Swamy G, Mukkamala R, Olivier NB.** Estimation of the aortic pressure waveform from a peripheral artery pressure waveform via an adaptive transfer function. *30th Annu IEEE EMBS Conf* 1: 1385–1388, 2008.
16. **Swamy G, Kuiper J, Gudur M, Olivier NB, Mukkamala R.** Continuous left ventricular ejection fraction monitoring by aortic pressure waveform analysis. *Ann Biomed Eng* 37: 1055–1068, 2009.
17. **Wadell TK, Dart AM, Medley TL, Cameron JD, Kingwell BA.** Carotid pressure is a better predictor of coronary artery disease severity than brachial pressure. *Hypertension* 38: 927–931, 2001.
18. **Westerhof BE, Guelen I, Stok WJ, Wesseling KH, Spaan JA, Westerhof N, Bos WJ, Stergiopulos N.** Arterial pressure transfer characteristics: effects of travel time. *Am J Physiol Heart Circ Physiol* 292: H800–H807, 2007.
19. **Westerhof N, Sipkema P, Van Den Bos GC, Elzinga G.** Forward and backward waves in the arterial system. *Cardiovasc Res* 6: 648–656, 1972.

Improved pulse transit time estimation by system identification analysis of proximal and distal arterial waveforms

Da Xu,[1] Kathy L. Ryan,[2] Caroline A. Rickards,[3] Guanqun Zhang,[1] Victor A. Convertino,[2] and Ramakrishna Mukkamala[1]

[1]*Michigan State University, East Lansing, Michigan;* [2]*United States Army Institute of Surgical Research, Fort Sam Houston; and* [3]*University of Texas at San Antonio, San Antonio, Texas*

Xu D, Ryan KL, Rickards CA, Zhang G, Convertino VA, Mukkamala R. Improved pulse transit time estimation by system identification analysis of proximal and distal arterial waveforms. *Am J Physiol Heart Circ Physiol* 301: H1389–H1395, 2011. First published July 29, 2011; doi:10.1152/ajpheart.00443.2011.—We investigated the system identification approach for potentially improved estimation of pulse transit time (PTT), a popular arterial stiffness marker. In this approach, proximal and distal arterial waveforms are measured and respectively regarded as the input and output of a system. Next, the system impulse response is identified from all samples of the measured input and output. Finally, the time delay of the impulse response is detected as the PTT estimate. Unlike conventional foot-to-foot detection techniques, this approach is designed to provide an artifact robust estimate of the true PTT in the absence of wave reflection. The approach is also applicable to arbitrary types of arterial waveforms. We specifically applied a parametric system identification technique to noninvasive impedance cardiography (ICG) and peripheral arterial blood pressure waveforms from 15 humans subjected to lower-body negative pressure. We assessed the technique through the correlation coefficient (r) between its 1/PTT estimates and measured diastolic pressure (DP) per subject and the root mean squared error (RMSE) of the DP predicted from these estimates and measured DP. The technique achieved average r and RMSE values of 0.81 ± 0.16 and 4.3 ± 1.3 mmHg. For comparison, the corresponding values were 0.59 ± 0.37 ($P < 0.05$) and 5.9 ± 2.5 ($P < 0.01$) mmHg for the conventional technique applied to the same waveforms and 0.28 ± 0.40 ($P < 0.001$) and 7.2 ± 1.8 ($P < 0.001$) mmHg for the conventional technique with the ECG waveform substituted for the ICG waveform. These results demonstrate, perhaps for the first time, that the system identification approach can indeed improve PTT estimation.

arterial blood pressure; arterial stiffness; foot-to-foot detection; impulse response; pulse wave velocity

ACCORDING TO THE MOENS-KORTEWEG equation, pulse wave velocity (PWV) increases as the arteries stiffen. Indeed, PWV is the most popular index of arterial stiffness because of the ease of its measurement and its proven independent value in predicting cardiovascular events and mortality in hypertensive patients (2, 4, 12, 14). In addition, because arterial stiffness increases with arterial blood pressure (ABP), PWV and ABP often show positive correlation, suggesting that PWV could provide a means to achieve continuous, noninvasive, and cuffless ABP monitoring (18).

Conventionally, PWV is determined from the distance and pulse transit time (PTT) between proximal and distal arterial sites (5). PTT is, in turn, estimated by acquiring arterial waveforms from the two sites and then detecting the foot-to-foot time delay between the waveforms. The premise is that the foot of the proximal waveform represents a time before the return of the reflected wave to its measurement site. However, wave reflection may not always be negligible at the proximal waveform foot. Just as important, it is often difficult to detect the waveform feet reliably because of motion and other artifact (16). Thus, the foot-to-foot detection technique can yield inaccurate PTT estimates. Compounding matters, ABP changes perturb PWV relatively little (18). Thus, typical plots of ABP vs. PWV show significant vertical scatter about the line of best fit (18). This scatter limits the ability of PWV to track ABP.

Several investigators have aimed to improve PTT estimation by more sophisticated analysis of proximal and distal arterial waveforms. Sola et al. (21) applied parametric modeling to the systolic upstrokes of the waveforms to identify their feet more reliably. Pruett et al. (18) computed an average of multiple time delays taken from the early systolic samples of two ABP waveforms to establish PTT estimates that were able to reduce the scatter in ABP vs. PWV plots. While their idea of mitigating PTT error by using more than one pair of samples of the waveforms is interesting, wave reflection becomes a greater factor as the cardiac cycle progresses. This technique is also restricted to ABP and flow waveforms. Latson et al. applied nonparametric system identification to estimate the impulse response (time domain version of the transfer function) relating a proximal ABP waveform (input) to a distal ABP waveform (output) and then estimated PTT as its time delay (11). Their intriguing idea was that, since the impulse response represents the distal ABP response to a very narrow pulse applied to proximal ABP at *time 0*, this PTT estimate should not be corrupted by wave reflection. However, neither Latson et al. nor an ensuing group who reproduced their technique (17) showed that it actually improved PTT estimation. Furthermore, this approach is applicable to arbitrary arterial waveforms (rather than being limited to ABP waveforms) and should afford great robustness to artifact, since PTT is determined from all pairs of waveform samples. However, these latter ideas may have not been noted until now.

We investigated the system identification approach for PTT estimation. We specifically applied a robust parametric system identification technique to an impedance cardiography (ICG) waveform (the proximal input) and a noninvasive peripheral ABP waveform (the distal output) recorded from humans subjected to progressive reductions in central blood volume using a lower-body negative pressure (LBNP) protocol. Because it is difficult to independently measure the true PTT in the absence of wave reflection, we assessed the technique

Address for reprint requests and other correspondence: R. Mukkamala, Dept. of Electrical and Computer Engineering, Michigan State Univ., 2120 Engineering Bldg., East Lansing, MI 48824-1226 (e-mail: rama@egr.msu.edu).

in terms of the ability of its (proportional) PWV estimates to track ABP changes. Our results show that the technique greatly reduced the scatter in ABP vs. PWV plots compared with conventional foot-to-foot detection techniques. A preliminary version of this study has been reported in abbreviated form (23).

MATERIALS AND METHODS

Physiological data. Existing, deidentified physiological data from humans subjected to a LBNP protocol were analyzed. The data collection procedures were approved by the Institutional Review Board of the Brooke Army Medical Center (Fort Sam Houston, TX) and are described in detail in several recent publications (7, 20).

Briefly, fit and typically young subjects that showed no signs of cardiovascular abnormalities (e.g., hypertension, hypotension, autonomic nervous dysfunction) and were not pregnant or taking any medications known to alter autonomic nervous function were studied. The subjects were instrumented for measurement of various physiological data, including noninvasive stroke volume estimates via ICG, a noninvasive peripheral ABP waveform via finger-cuff photoplethysmography, and an ECG waveform. Subjects were positioned supine in a LBNP chamber. The data were then recorded at a sampling rate of 500 Hz during *1*) a 5-min baseline period; *2*) 5-min chamber decompression at −15, −30, −45, and −60 mmHg each; *3*) additional increments of −10 mmHg for 5 min until the onset of hemodynamic decompensation [as indicated by presyncopal symptoms, sudden fall in ABP or heart rate (HR), systolic pressure (SP) <80 mmHg, or at the subject's request]; and *4*) a 10-min recovery period.

For this study, 15-s steady segments of data during the baseline period, each distinct LBNP period, and the recovery period were extracted. Because PWV estimates would be assessed in terms of their ability to track ABP changes, appreciable changes in ABP within a subject were needed for the assessment to be challenging and useful. Thus, data from subjects with more modest diastolic pressure (DP) changes (maximum average DP over the periods minus the minimum average DP over the periods <20 mmHg) were excluded. Data from 15 of 66 available subjects (nine males and six females; age 31 ± 8 yr; height 173 ± 12 cm; weight 76 ± 15 kg) remained for analysis.

PTT estimation. PTT was estimated by applying conventional foot-to-foot detection techniques to the simultaneous pairs of the 15-s segments of the differentiated ICG waveform (a proximal arterial waveform that is specifically related to thoracic flow) or the ECG waveform (a commonly proposed surrogate for the proximal arterial waveform) and the peripheral ABP waveform (a distal arterial waveform). PTT was then estimated by applying a parametric system identification technique to the same pairs of ICG and peripheral ABP waveform segments.

Conventional foot-to-foot detection techniques. Figure 1 shows the conventional foot-to-foot detection techniques. First, the waveform feet were detected as the R waves for the ECG waveform, the standard B points for the ICG waveform (i.e., the time of zero derivative before the peak) (22), and the minima for the peripheral ABP waveform (i.e., DP). These foot detection techniques yielded the best results among a set of conventional techniques (6) and are thus referred to as optimized henceforth. Next, the time delays between each R wave and subsequent DP (T_{d1}) and between each B point and ensuing DP (T_{d2}) were determined. Finally, the time delays were averaged over the 15-s waveform segments to reduce noise in the PTT estimates.

Parametric system identification technique. Figure 2 shows the parametric system identification technique. The differentiated ICG waveform was considered to be the input [$x(t)$] to a system while the peripheral ABP waveform [$y(t)$] was regarded as the resulting output. The system was identified by finding its impulse response [$h(t)$], which when convolved with $x(t)$, optimally fitted $y(t)$. The time delay of $h(t)$ (T_{d3}) was then detected as the estimate of PTT. This estimate may be viewed as the time delay for a very narrow pulse of thoracic
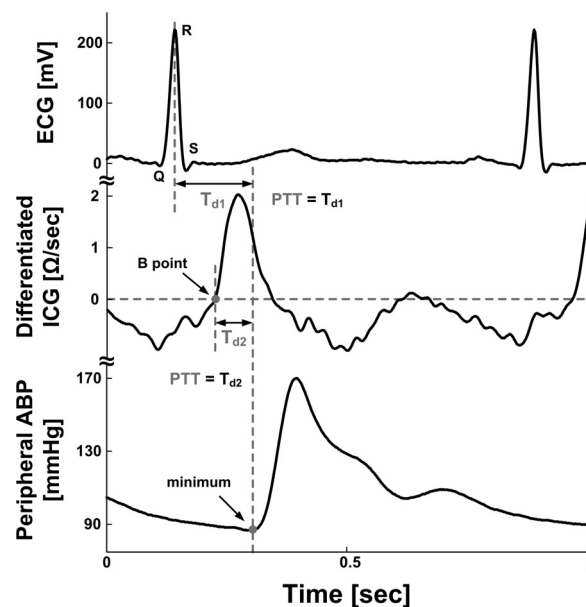

Fig. 1. Optimized conventional foot-to-foot detection techniques for estimating pulse transit time (PTT) from either an ECG or impedance cardiography (ICG) waveform (a proximal waveform) and a simultaneous noninvasive peripheral arterial blood pressure (ABP) waveform (a distal waveform) [the time delays between each R wave and subsequent DP (T_{d1}) and between each B point and ensuing DP (T_{d2})].

flow to reach the peripheral ABP measurement site or the time delay between the entire ICG and peripheral ABP waveforms after equalizing their shapes. Mathematical details are provided immediately below.

The impulse response $h(t)$ was estimated as per the following autoregressive exogenous input structure:

$$y(t) = \sum_{k=1}^{n} a_k y(t-k) + \sum_{k=0}^{m} b_k x(t-k) + e(t),$$

where a_k and b_k are sets of unknown parameters that define $h(t)$, n and m denote the number of parameters in the sets, and $e(t)$ is the unmeasured residual error (13). The term n had little effect on the results and was arbitrarily fixed to five, whereas the term m should scale with PTT and was simply set to T_{d2} times the sampling rate. The parameters were then estimated from the 15-s segments of $x(t)$ and zero-mean $y(t)$ by linear least-squares minimization of $e(t)$ (13). The time delay T_{d3} was thereafter determined as the time of the maximal second derivative of $h(t)$ between its first zero-crossover with positive derivative and its peak. This time, which denotes when the slope of $h(t)$ is changing most during its rise to the peak, provided a good marker of the foot location of $h(t)$ (6). [Determining T_{d3} as the first zero-crossover with positive derivative, which indicates when $h(t)$ first becomes positive as it rises to the peak, yielded similar results.]

PTT assessment and comparison. The PTT estimates of each technique were assessed based on their ability to track the average DP of the analyzed peripheral ABP waveform segments in each subject. Figure 3 shows the PTT assessment procedure. First, since PWV generally shows better linear correlation to DP than PTT, the reciprocals of the PTT estimates were first taken to arrive at proportional PWV estimates per subject. (Note that the proportionality constant, which represents the distance between the proximal and distal arterial sites, was not needed here.) Next, two quantitative metrics were computed. One metric was the standard correlation coefficient (r) between the proportional PWV estimates and measured DP. The other metric was the root mean squared error (RMSE) between the DP predicted by mapping the proportional PWV estimates through the
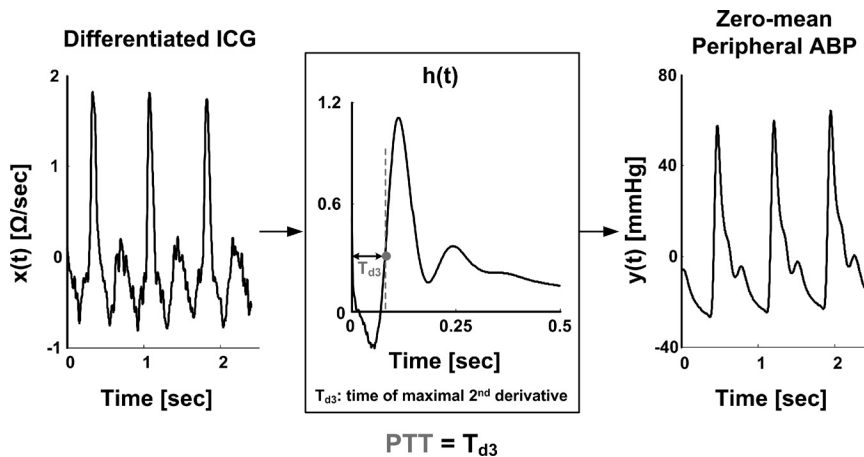
Fig. 2. Parametric system identification technique for estimating PTT from simultaneous ICG and noninvasive peripheral ABP waveforms. First, the former waveform is regarded as an input [$x(t)$] to a system while the latter waveform is considered to be the resulting output [$y(t)$]. Next, the system is identified by finding a parametric impulse response [$h(t)$] (see equation in MATERIALS AND METHODS) that, when convolved with $x(t)$, optimally fits $y(t)$. Finally, the time delay (T_{d3}) of $h(t)$ is detected as the time of its maximal second derivative so as to yield as an estimate of PTT.

line of best fit established from the correlation analysis and the measured DP.

The PTT estimates of the techniques were then statistically compared. Straightforward one-way repeated-measures ANOVA was specifically employed to compare the subject average r values and log-transformed RMSE values of the three techniques. Because both of these tests revealed $P < 0.05$, multiple pairwise comparisons between all techniques were then performed using the Student-Newman-Keuls post hoc test.

Fig. 3. Procedure for evaluating the PTT estimates of the techniques in terms of their ability to track diastolic pressure (DP) within a subject. Note that 1/PTT here is simply proportional to pulse wave velocity (PWV). RMSE is the root mean squared error.

RESULTS

Figure 4 shows sample plots of measured DP vs. the proportional PWV estimated by each technique from *subjects 15* and *12*. In *subject 15*, the parametric system identification technique noticeably reduced the scatter about the line of best fit compared with the conventional foot-to-foot detection techniques, especially with the ECG waveform substituted for the ICG waveform. In *subject 12*, the conventional techniques produced proportional PWV estimates that showed nonphysiological, negative correlation with DP, whereas the system identification technique yielded estimates that revealed the expected positive correlation.

Figure 5 shows plots of the DP predicted by each technique vs. measured DP from all 15 subjects and the corresponding overall RMSE values (i.e., the root mean square of the errors pooled together from all of the subjects). The system identification technique showed better predictions than both of the conventional techniques.

Table 1 shows the DP range and r and RMSE values of each technique per subject. The average r and RMSE values of the system identification technique were 0.81 ± 0.16 and 4.3 ± 1.3 mmHg. For comparison, the corresponding values were 0.59 ± 0.37 ($P < 0.05$) and 5.9 ± 2.5 ($P < 0.01$) mmHg for the conventional technique applied to the same waveforms and 0.28 ± 0.40 ($P < 0.001$) and 7.2 ± 1.8 ($P < 0.001$) mmHg for the conventional technique with the ECG waveform substituted for the ICG waveform. [Although not indicated in Table 1, the r and RMSE values of the two conventional techniques were also statistically different ($P < 0.05$).] Furthermore, of the 15 r values corresponding to each subject, only 3 were <0.80 for the system identification technique compared with 8 and 15 for the conventional techniques.

DISCUSSION

In summary, PWV is a useful marker of arterial stiffness and may permit continuous, noninvasive, and cuffless ABP monitoring. Conventionally, PWV is determined as the ratio of the distance and PTT between proximal and distal arterial sites. PTT is, in turn, estimated by detecting the foot-to-foot time delay between waveforms measured at the two arterial sites of interest. However, this technique can provide inaccurate PTT estimates because of wave reflection interference and wave-
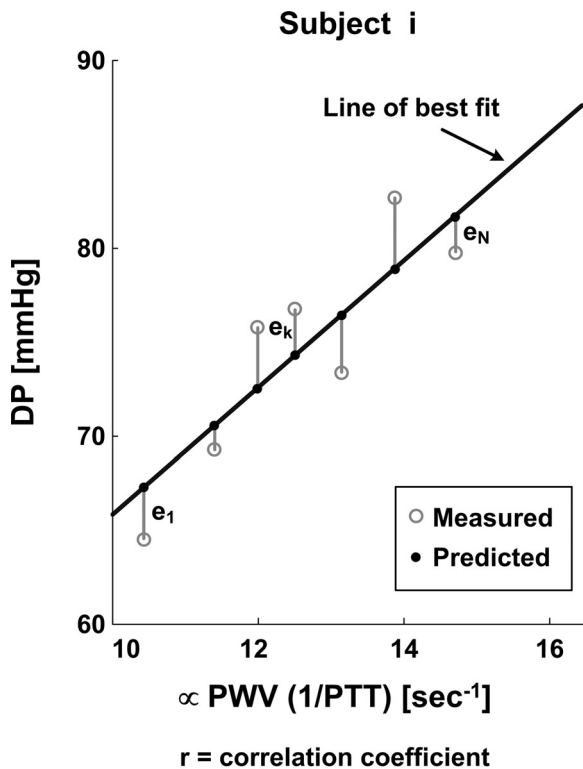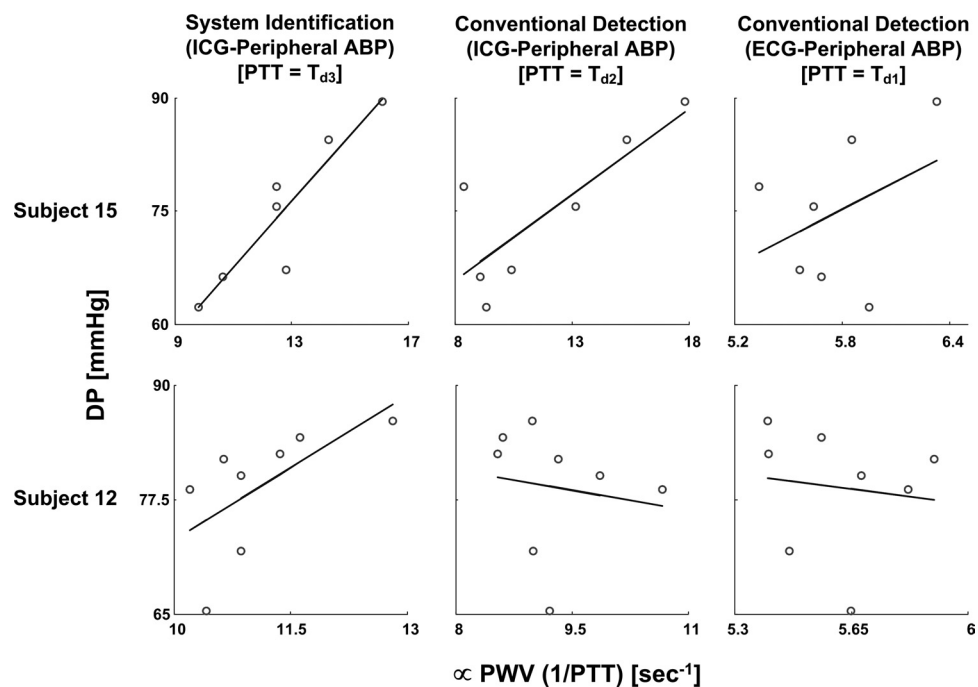
Fig. 4. Plots of measured DP vs. the proportional PWV estimated by each technique from *subjects 15* and *12*.

form artifact. The system identification approach for estimating PTT potentially provides a means to overcome both of these limitations while being applicable to arbitrary types of arterial waveforms. We applied a parametric system identification technique to noninvasive ICG and peripheral (finger) ABP waveforms measured from healthy humans during progressive LBNP. The resulting PTT estimates correlated with ABP much better than those of optimized conventional techniques. To our knowledge, these results are the first to demonstrate that the system identification approach can indeed improve PTT estimation.

System identification approach for PTT estimation. The system identification approach for PTT estimation is employed as follows. First, proximal and distal arterial waveforms are measured and respectively regarded as the input and output of a system. Next, the system impulse response is identified from the measured input and output. Finally, the time delay of the

impulse response is detected as an estimate of PTT. This approach is similar in concept to previous techniques for estimating PTT that have experimentally eliminated the reflected wave by applying a transient perturbation to a proximal arterial site and then measuring the time delay for the response to occur at a distal arterial site (1, 10). However, the obvious advantage of the system identification approach is that no experimental perturbation is needed.

The system identification approach should also afford significant advantages over conventional foot-to-foot detection techniques and other previous techniques for estimating PTT without a perturbation. First, this approach effectively determines PTT from all pairs of samples of the waveforms, rather than just one pair or a few pairs, by mathematically eliminating the reflected wave or, more generally, equalizing the waveform shapes. In this way, the approach should be robust to waveform artifact while revealing the true PTT in the absence of wave
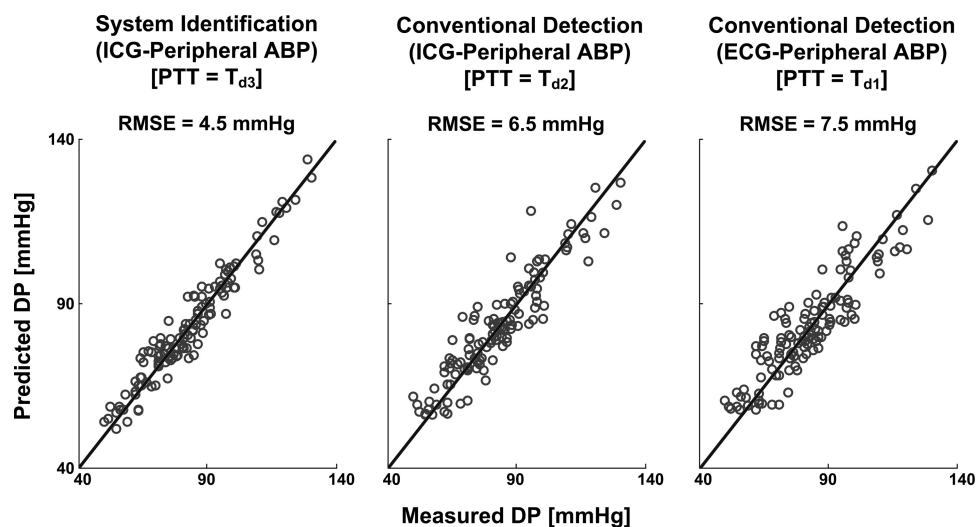

Fig. 5. Plots of the DP predicted from the proportional PWV estimates of each technique vs. measured DP from all 15 subjects. The RMSE values represent the root mean square of the errors pooled together from all of the subjects instead of the average of the RMSE values over the subjects (as shown in Table 1).

Table 1. *Results of each pulse transit time estimation technique per subject*

Subject No.	DP Range, mmHg	System Identification (ICG-Peripheral ABP) (PTT = T_{d3})		Conventional Detection (ICG-Peripheral ABP) (PTT = T_{d2})		Conventional Detection (ECG-Peripheral ABP) (PTT = T_{d1})	
		r	RMSE, mmHg	r	RMSE, mmHg	r	RMSE, mmHg
1	75–101	0.55	6.8	0.39	7.5	0.33	7.7
2	97–121	0.96	2.7	0.91	3.8	0.53	7.8
3	71–99	0.85	4.2	0.86	4.2	0.63	6.3
4	95–116	0.85	4.0	0.88	3.6	0.46	6.8
5	88–130	0.95	4.8	0.66	11.8	0.76	10.1
6	64–86	0.92	2.4	0.86	3.1	0.47	5.3
7	69–100	0.84	5.9	0.18	10.8	0.20	10.7
8	54–75	0.83	3.6	0.81	3.8	0.36	6.1
9	64–85	0.38	6.5	0.61	5.6	−0.89	3.2
10	65–91	0.85	4.5	0.85	4.5	0.29	8.2
11	72–95	0.91	3.3	0.71	5.4	0.35	7.2
12	65–86	0.63	5.0	−0.15	6.4	−0.13	6.4
13	50–71	0.82	3.9	−0.23	6.6	−0.12	6.8
14	62–83	0.91	3.4	0.69	5.9	0.49	7.1
15	62–89	0.92	3.7	0.81	5.5	0.39	8.6
Average	70–95	0.81 ± 0.16	4.3 ± 1.3	0.59 ± 0.37‡	5.9 ± 2.5†	0.28 ± 0.40*	7.2 ± 1.8*

Average quantities are presented as means ± SD. DP, diastolic pressure; ICG, impedance cardiography; ABP, arterial blood pressure; r, correlation coefficient between 1/PTT estimates and DP; RMSE, root mean squared error between DP predicted from 1/PTT estimates and measured DP. Level of statistical significance vs. system identification: *$P < 0.001$, †$P < 0.01$, and ‡$P < 0.05$. See the legend for Fig. 1 for remaining abbreviations.

reflection. The approach is therefore intended to improve the accuracy of PTT estimation rather than to make the PTT measurement process more convenient as others have proposed via an ECG or otherwise (19). Second, the system identification approach is applicable to arbitrary types of arterial waveforms, including those indicative of ABP, flow, and volume, instead of being restricted to certain types of waveforms (18). For example, the waveforms could be acquired with tonometry, ultrasound, ballistocardiography (proximal only), electrical impedance, pulse oximetry, and even noncontact laser Doppler vibrometry (8). The disadvantage of the approach is that it may not be able to estimate PTT on a beat-to-beat basis, since longer waveform segments are typically needed to reliably identify the impulse response.

Evaluation approach and limitations. Ideally, we would have evaluated the parametric system identification technique against reference measurements of PTT. However, these measurements are not simple to make. We therefore evaluated the technique in terms of the ability of its proportional PWV estimates to track changes in ABP induced by progressive LBNP. Note that the approach of evaluating PWV estimates in terms of their ability to track ABP changes is not new and originates from many studies that have shown a tight, acute relationship between PWV and ABP (9, 18).

However, we acknowledge that ABP was likely not the only significant determinant of the true PWV in this study. Indeed, vasomotor tone changes (e.g., vasoconstriction occurred during LBNP as a compensatory response), which may have altered PWV without appreciably influencing ABP, constitute the major study limitation. If PWV were estimated through the aorta, which is relatively sparse in smooth muscle (15), rather than to a finger, such changes may have been less of a factor. On the other hand, HR and cardiac output were probably not significant determinants of PWV in this study for the following reasons. First, PWV in large arteries is essentially constant across frequencies because of negligible viscous effects (16). Thus, since we investigated PWV through largely nonviscous arteries, PWV here should have been mostly independent of

HR. Second, PWV characterizes the properties of the arteries only. Therefore, cardiac output could have only impacted PWV via alterations in ABP.

Although the relationship between ABP and PWV generally follows an exponential (18), it could be well approximated here as linear because of the relatively narrow ABP range elicited by the LBNP. Thus, we quantitatively evaluated the ability of the technique to track ABP changes in terms of the linear correlation between its PWV estimates and ABP.

Tracking DP. In 15 subjects, DP was perturbed appreciably (>20 mmHg) by the LBNP. In these subjects, the parametric system identification technique achieved an average r value between its proportional PWV estimates and measured DP of 0.81 ± 0.16 and an average RMSE value between the DP predicted from these estimates and measured DP of 4.3 ± 1.3 mmHg. These averages were ~30% better than those of an optimized version of the conventional foot-to-foot detection technique applied to the same waveforms. Furthermore, in two subjects, the system identification technique was able to profoundly "correct" the PWV estimates of the conventional technique to show appropriate positive, rather than negative, correlation with DP.

We also assessed the conventional foot-to-foot detection technique with the ECG waveform substituted for the ICG waveform. This commonly proposed technique actually estimates the sum of PTT and the preejection period (PEP). Because PEP generally changed in the opposite direction of PTT with progressive LBNP (results not shown), the technique performed poorly in tracking DP. Note that the RMSE values of this technique should be interpreted with caution. For example, in *subject 9*, the technique showed a strong, nonphysiological negative correlation between its PWV estimates and DP and consequently a small RMSE value.

Tracking other ABP parameters. The proportional PWV estimates of the parametric system identification technique may correlate best with mean ABP, as they arise from all waveform samples. However, because LBNP perturbed DP much more than mean ABP, we focused on DP tracking.

Note that the PWV estimates of the conventional techniques are designed to track DP by virtue of being derived from the waveform feet. Nevertheless, the PWV estimates of the system identification technique were able to follow DP better than those of the conventional techniques. The likely reason is that DP correlated well with mean ABP here, which is generally the case. On the other hand, SP can show less correlation to DP and mean ABP. Indeed, for those subjects whose SP changed by >20 mmHg ($n = 12$), none of techniques yielded proportional PWV estimates that were able to track SP (average r and RMSE values ranged from 0.11 ± 0.50 to 0.29 ± 0.45 and from 8.6 ± 3.6 to 9.0 ± 4.3 mmHg; $P =$ not significant). These results are not an indictment against the system identification technique or the conventional technique applied to the same waveforms, since their PWV estimates correlated significantly better with DP. However, because the PWV estimates of the conventional technique applied to the ECG waveforms showed poor tracking of all ABP parameters, we conclude that it is not suitable during progressive central hypovolemia.

Reproducibility. In addition to accuracy, reproducibility across time in the same subjects would be another necessary attribute for the parametric system identification technique. In *subjects 1* and *4*, repeated measurements were available on a second day. We therefore conducted preliminary reproducibility testing of the technique. The overall RMSE of the PTT estimates on the second day relative to the first day was just 4.9%. Thus, the technique was highly reproducible. Furthermore, the first and second day r values between the proportional PWV estimates and measured DP were 0.55 and 0.51 in one of the subjects and 0.85 and 0.80 in the other subject. Thus, the evaluation results of the technique were also reproducible. For the conventional techniques, the corresponding reproducibility results were generally not as strong. For example, the overall RMSE values of their PTT estimates between the two days were ~13% each.

Future directions and potential clinical applications. Further investigation of the system identification approach for PTT estimation is warranted. First and foremost, testing of the approach in patients recommended for PWV monitoring (e.g., elderly, hypertensives) is a must. Thorough reproducibility testing also remains to be performed. In addition, refinements to the specific technique described herein via other system identification and time-delay estimation techniques (3) are also needed to reduce or even eliminate instances of poor performance (i.e., *subject 9*).

With successful future efforts, the system identification approach for PTT estimation may be employed for improved arterial stiffness monitoring in hypertension patients. For example, consistent with common practice (14), this approach could be applied to noninvasive carotid and femoral ABP waveforms obtained with tonometry in these patients for more accurate PWV estimation and thus potentially superior prognostic information (although nontrivial PWV error may still be present because of transit distance measurement inaccuracy). The approach could also be applied to arterial waveforms acquired with simple sensors (e.g., carotid artery and toe pulse oximeters) for potentially accurate, continuous, noninvasive, and cuffless ABP monitoring. However, other problems, including convenient construc-

tion of patient-specific calibration curves relating DP and mean ABP to PWV as well as SP estimation, must be solved before it could be used for such convenient ABP monitoring.

DISCLOSURES

None.

REFERENCES

1. **Anliker M, Histand MB, Ogden E.** Dispersion and attenuation of small artificial pressure waves in the canine aorta. *Circ Res* 23: 539–551, 1968.
2. **Asmar R.** *Arterial Stiffness and Pulse Wave Velocity. Clinical Applications*. St. Louis, MO: Elsevier, 1999.
3. **Bjorklund S.** *A survey and comparison of time-delay estimation methods in linear systems* (online). http://www.control.isy.liu.se/publications/doc?id=1599 [12 March, 2011].
4. **Blacher J, Asmar R, Djane S, London GM, Safar ME.** Aortic pulse wave velocity as a marker of cardiovascular risk in hypertensive patients. *Hypertension* 33: 1111–1117, 1999.
5. **Boutouyrie P, Briet M, Collin C, Vermeersch S, Pannier B.** Assessment of pulse wave velocity. *Artery Res* 3: 3–8, 2009.
6. **Chiu YC, Arand PW, Shroff SG, Feldman T, Carroll JD.** Determination of pulse wave velocities with computerized algorithms. *Am Heart J* 121: 1460–1470, 1991.
7. **Convertino VA, Ryan KL, Rickards CA, Salinas J, McManus JG, Cooke WH, Holcomb JB.** Physiological and medical monitoring for en route care of combat casualties. *J Trauma* 64: S342–S353, 2008.
8. **De Melis M, Morbiducci U, Scalise L, Tomasini EP, Delbeke D, Baets R, Van Bortel LM, Segers P.** A noncontact approach for the evaluation of large artery stiffness: a preliminary study. *Am J Hypertens* 21: 1280–1283, 2008.
9. **Geddes LA, Voelz MH, Babbs CF, Bourland JD, Tacker WA.** Pulse transit time as an indicator of arterial blood pressure. *Psychophysiology* 18: 71–74, 1981.
10. **Landowne M.** A method using induced waves to study pressure propagation in human arteries. *Circ Res* 5: 594–601, 1957.
11. **Latson TW, Hunter WC, Katoh N, Sagawa K.** Effect of nitroglycerin on aortic impedance, diameter, and pulse-wave velocity. *Circ Res* 62: 884–890, 1988.
12. **Laurent S, Boutouyrie P, Asmar R, Gautier I, Laloux B, Guize L, Ducimetiere P, Benetos A.** Aortic stiffness is an independent predictor of all-cause and cardiovascular mortality in hypertensive patients. *Hypertension* 37: 1236–1241, 2001.
13. **Ljung L.** *System Identification: Theory for the User*. Englewood Cliffs, NJ: Prentice Hall, 1987.
14. **Mancia G, De Backer G, Dominiczak A, Cifkova R, Fagard R, Germano G, Grassi G, Heagerty AM, Kjeldsen SE, Laurent S, Narkiewicz K, Ruilope L, Rynkiewicz A, Schmieder RE, Boudier HA, Zanchetti A.** Guidelines for the management of arterial hypertension: the Task Force for the management of arterial hypertension of the European Society of Hypertension (ESH) and of the European Society of Cardiology (ESC). *J Hypertens* 25: 1105–1187, 2007.
15. **McDonald DA.** Regional pulse-wave velocity in the arterial tree. *J Appl Physiol* 24: 73–78, 1968.
16. **Milnor WR.** *Hemodynamics*. Baltimore, MD: Williams & Wilkins, 1989.
17. **Mitchell GF, Pfeffer MA, Finn PV, Pfeffer JM.** Comparison of techniques for measuring pulse-wave velocity in the rat. *J Appl Physiol* 82: 203–210, 1997.
18. **Pruett JD, Bourland JD, Geddes LA.** Measurement of pulse-wave velocity using a beat-sampling technique. *Ann Biomed Eng* 16: 341–347, 1988.
19. **Qasem A, Avolio A.** Determination of aortic pulse wave velocity from waveform decomposition of the central aortic pressure pulse. *Hypertension* 51: 188–195, 2008.

20. **Reisner AT, Xu D, Ryan KL, Convertino VA, Rickards CA, Mukkamala R.** Monitoring non-invasive cardiac output and stroke volume during experimental human hypovolaemia and resuscitation. *Br J Anaesth* 106: 23–30, 2011.
21. **Sola J, Vetter R, Renevey P, Chetelat O, Sartori C, Rimoldi SF.** Parametric estimation of pulse arrival time: a robust approach to pulse wave velocity. *Physiol Meas* 30: 603–615, 2009.

22. **Woltjer HH, Bogaard HJ, de Vries PMJM.** The technique of impedance cardiography. *Eur Heart J* 18: 1396–1403, 1997.
23. **Xu D, Ryan KL, Rickards CA, Zhang G, Convertino VA, Mukkamala R.** Robust pulse wave velocity estimation by application of system identification to proximal and distal arterial waveforms. In: *Proc 32nd Annu Int Conf IEEE EMBS* 1: 3559–3562, 2010.